Forschungszentrum Karlsruhe
in der Helmholtz-Gemeinschaft

Wissenschaftliche Berichte

FZKA 7435

Modelling of Intra- and Inter-Species Charged Particle Collisions for Flow Simulation in Pulsed Plasma Thrusters

D. D'Andrea

Institut für Hochleistungsimpuls- und Mikrowellentechnik
Programm FUSION
Association EURATOM/Forschungszentrum Karlsruhe

Oktober 2009

Forschungszentrum Karlsruhe
in der Helmholtz-Gemeinschaft
Wissenschaftliche Berichte

FZKA 7435

Modelling of Intra- and Inter-Species Charged Particle Collisions for Flow Simulation in Pulsed Plasma Thrusters

Danilo D'Andrea

Institut für Hochleistungsimpuls- und Mikrowellentechnik
Programm Fusion
Association EURATOM-FZK

vom Institut für Aerodynamik und Gasdynamik
der Universität Stuttgart genehmigte Dissertation

Forschungszentrum Karlsruhe GmbH, Karlsruhe

2009

Forschungszentrum Karlsruhe GmbH
Postfach 3640, 76021 Karlsruhe

Mitglied der Hermann von Helmholtz-Gemeinschaft
Deutscher Forschungszentren (HGF)

ISSN 0947-8620

urn:nbn:de:0005-074352

Modelling of Intra- and Inter Species Charged Particle Collisions for Flow Simulation in Pulsed Plasma Thrusters

A thesis accepted by the Faculty of Aerospace Engineering and Geodesy of the Universität Stuttgart in partial fulfilment of the requirements for the degree of Doctor of Engineering Sciences (Dr.-Ing.)

by

Danilo D'Andrea

from Lecce, Salento.

Committee chair: Prof. Dr. C.-D. Munz
Committee member: Prof. Dr. Dr. h.c. M. Thumm
Date of defence: July 22, 2008

Institute of Aerodynamics and Gas Dynamics
Universität Stuttgart
2008

ACKNOWLEDGMENTS

I gratefully acknowledge the Landesstiftung Baden-Württemberg for funding the present work from October 2004 to November 2006 and I also wish to thank the Forschungszentrum Karlsruhe – in der Helmholtzgemeinschaft for the financial support and during the year 2007.

My best thanks to Jörg Heiermann and his wife Natasha for making this possible; not only they let me fulfil my dream but also allow me to find my way.

I could never be grateful enough to my supervisor Dr. Rudolf Schneider, for his patient presence, his dedication and his immense moral and material support during these three years.

I am thankful to my family for being always helpful in the difficult moments and to Manuela for resisting in spite of everything.

Karlsruhe, den 18.03.2008

Danilo D'Andrea

To Silvestro, my cat

Kurzfassung

Modellierung der Streuung geladener gleich- und verschiedenartiger Teilchen zur Strömungssimulation in gepulsten Plasmatriebwerken

Für ein besseres physikalisches Verständnis von elektrischen Antriebssystemen für die Raumfahrt, wie beispielsweise gepulste Plasma-Thruster, ist die numerische Modellierung und Simulation von hochverdünnten Plasmaströmungen unumgänglich. Die mathematische Formulierung solcher Phänomene basiert auf der kinetischen Beschreibung, wie sie durch die vollständige, zeitabhängige Boltzmanngleichung gegeben ist. Eine attraktive Strategie um das komplexe, nichtlineare Boltzmann-Problem numerisch anzugehen, besteht in der Kombination von bekannten Particle-in-Cell (PIC) und Monte Carlo Methoden, die durch einen PIC-basierten Fokker-Planck Löser erweitert werden müssen. Die Konstruktion und Entwicklung des PIC-basierten Fokker-Planck Lösers ist der Gegenstand der vorliegenden Arbeit. Das gesamte numerische Modell trägt der Physik der Wechselwirkung von geladenen Teilchen mit elektromagnetischen Feldern, der inelastischen Streuung von Elektronen mit Neutralteilchen als auch der Kollision zwischen gleichartigen (intraspezies) und verschiedenartigen (interspezies) geladenen Teilchen Rechnung.

Zur Beschreibung der elastischen intra- und interspezies Coulomb Wechselwirkung geladener Teilchen ist es zweckmäßig vom Boltzmannschen Stoßintegral aus zu starten, wobei für den differentiellen Wirkungsquerschnitt die klassische Rutherfordformel benutzt wird. Eine Taylorentwicklung der gestreuten Verteilungsfunktionen nach der Geschwindigkeit bis zur zweiten Ordnung und die Annahme eines Grenzwertes des maximalen Stoßparameters erlauben es schließlich, das Boltzmannintegral zu integrieren, wodurch man zur Fokker-Planck Gleichung gelangt. Die zentralen physikalischen Größen, die in der Fokker-Planck Gleichung auftauchen sind der Vektor der Reibungskraft und der Diffusionstensor. Die Schlüsselelemente zur Berechnung dieser tensoriellen Koeffizienten sind die sogenannten Rosenbluthpotenziale. Diese sind ihrerseits komplizierte Integrale, die sich über den gesamten Geschwindigkeitsbereich erstrecken und deren Integranden aus dem Produkt der Verteilungsfunktion der Streuer-Teilchen und der Relativgeschwindigkeit der gestreuten und streuenden Partikel bestehen. Üblicherweise werden zur Berechnung dieser Potenziale oft sehr restriktive Annahmen gemacht: So wird gewöhnlich vorausgesetzt, dass die Geschwindigkeitsverteilung der Feldteilchen, wie die Streuer auch genannt werden, isotrop ist. Die Beobachtung, dass die Rosenbluthpotenziale Faltungsintegrale sind, legt das Vorgehen nahe, Techniken anzuwenden, die auf der Fouriertransformation basieren, um diese Potenziale und deren Ableitung zu bestimmen. Solch eine Vorgehensweise bringt den Vorteil mit sich, dass keinerlei Annahmen hinsichtlich der Gestalt der Verteilungsfunktion getroffen werden müssen. Es sei weiterhin erwähnt, dass diese Art der Bestimmung der Rosenbluthpotentiale den Grundstock für die selbstkonsistente Modellierung der Stoßrelaxation legt.

Um die dreidimensionale Fokker-Planck Gleichung, welche die Entwicklung der gestreuten

Verteilungsfunktion beschreibt, in den numerischen Rahmen der Teilchenmethoden einzubinden, wird die Äquivalenz dieser Gleichung zu den stochastischen Differentialgleichungen benutzt. Die stochastische Variable $\mathbf{C}(t)$, die solch einer Gleichung genügt, wird später mit der Geschwindigkeit der geladenen Teilchen identifiziert. Auch im Kontext der stochastischen Differentialgleichungen spielen die oben erwähnte Reibungskraft und eine Matrix, die von dem Diffusionstensor abgeleitet ist, eine zentrale Rolle. Mit Hilfe der Itô-Taylor Entwicklung und dem auf Itô zurückgehenden Rechenverfahren gelingt es, die stochastische Differentialgleichung zu diskretisieren und geeignete numerische Schemata abzuleiten. In der vorliegenden Arbeit wurden sogenannte explizite, schwache Schemata bis zur Verfahrensordnung zwei herangezogen, um die Geschwindigkeit der geladenen Simulationsteilchen zu bestimmen.
Diese schwachen Itô-Taylor Verfahren stellen im Zusammenhang mit der verwendeten Fouriertransformationsmethode und den Teilchen-Gitter Kopplungstechniken ein bemerkenswertes Simulationswerkzeug dar, mit dessen Hilfe sich der Stoßrelaxationsprozess ohne spezielle Annahmen oder Modellen untersuchen läßt. Als Folge dieser selbstkonsistenten Berechnungmethode lassen sich beispielsweise unterschiedliche Zeitskalen des Relaxationsprozesses realistischer ermitteln als mit dem sogenannten Testteilchen-Ansatz.

Die vorgestellte Modellierung der Streuung gleichartiger geladener Teilchen läßt sich direkt auf die interspezies Wechselwirkung zwischen Elektronen und Ionen übertragen. Darüber hinaus erlaubt die Struktur der entwickelten, auf der PIC-Technik basierenden Methoden die numerische Simulation der gekoppelten Prozesse von intra- und interspezies Wechselwirkung.

Abstract

A better physical understanding of electrical space propulsion systems like Pulsed Plasma Thrusters requires the numerical modelling and simulation of highly rarefied plasma flows. Mathematically, such phenomena demand a kinetic description which is established by the complete, time-dependent Boltzmann equation. An attractive numerical approach to tackle this complex non-linear problem consists of a combination of the well-known Particle-in-Cell (PIC) and Monte Carlo methods extended by a PIC-based Fokker-Planck solver, on which we focus our attention in the following. This numerical model accommodates the physics of interaction of charged particles with electromagnetic fields, inelastic electron-neutral scattering as well as intra- and inter-species charged particle Coulomb collisions.

To describe elastic intra- and inter-species charged particle Coulomb collisions it is convenient to start from the Boltzmann collision integral with the classical Rutherford differential cross section. A Taylor series expansion up to second order in velocity of the post-collision distribution functions and the adoption of a cut-off value for the impact parameter permits the final integration of the Boltzmann integral to obtain the Fokker-Planck equation. The central quantities appearing in the Fokker-Planck equation are the friction force vector and the diffusion tensor. The keys to compute the friction and diffusion coefficients are the Rosenbluth potentials which are in turn complicate integrals of the field particle distribution function and the relative velocity between test and field particles. Usually, strong assumptions like isotropic velocity distribution of the scatterer, are made to evaluate the Rosenbluth potentials. Observing that the Rosenbluth potentials are convolution intergrals addresses the use of fast Fourier transform techniques to calculate these quantities and their derivatives rapidly with the advantage of being free of any additional assumption. Furthermore, such a determination the Rosenbluth potentials is the basis to model collisional relaxation in a complete self-consistent manner.

In order to fit the three-dimensional Fokker-Planck equation of the scattered distribution function into a particle-based method framework, the equivalence with the stochastic differential equation (SDE) is exploit. The stochastic variable $\mathbf{C}(t)$ which obeys the SDE is later identified with the charged particle velocity. Also in this context the friction force vector and a matrix derived from the diffusion tensor play the central role. By means of Itô-Taylor expansion and Itô calculus the stochastic differential equation is discretised and numerical schemes are derived. In this work, explicit weak schemes up to approximation order two have been applied to update the particles velocity.

These weak Itô-Taylor schemes together with the Fourier transform method and particle-mesh interface techniques form a remarkable simulation tool to study collisional relaxation processes from first principles. For instance by means of this tool, a more realistic evaluation of the time scales can be provided since the classical test-particle approach is not necessary anymore thanks to self-consistency.

The introduced intra-species charged particle modelling can be easily adapted for inter-species

electron-ion particle collisions. Finally, the structure of the developed PIC-based method to solve the Fokker-Planck equation also allows to combine intra- and inter-species collisions to perform coupled simulations.

Contents

1. Scientific Context and Motivations

The purpose of this work is the development of a suitable numerical tool which takes into account Coulomb collisions in the simulation of plasma devices, and in particular of plasma accelerators for space-propulsion applications.

After a period of oblivion, these propulsion systems are the object of a renewed scientific interest, thanks also to the progresses in computer technology which allowed the numerical simulations to enhance their very promising features. In fact, plasma thrusters can outperform conventional chemical (liquid and solid propellant) propulsion systems because of their higher specific impulse values I_{sp}, i.e., the change in momentum per unit of propellant [1]. In the history of these devices, the 1990s have been classified as the "era of application" because their benefits have been realised on numerous commercial satellites. The risk of employing plasma thrusters on spacecraft has diminished in recent years due to an increase in the number of successfull missions. Plasma propulsion can provide mass and cost savings, increasing orbital lifetimes, and increased mission capability and flexibility.

Since more than two decades, the IRS (Institute of Space Systems, University of Stuttgart), has started a "small satellite" program, in whose frame a lunar satellite is under development. Mission BW-1 will be accomplished by a **P**ulsed **P**lasma **T**hruster PPT, named SIMPLEX (**S**tuttgart **I**nstationary **M**agneto**P**lasmadynamic Thruster for **L**unar **Ex**ploration). In this frame, a PPT is a natural choice for its properties of compactness, reliability and ease of construction. Moreover the pulsed energy release allows for low average power without loss of performances, a tight constrain on board of small satellites [2].

SIMPLEX is essentially a condensator (see Fig. 1.1) which charges the electrode to a po-

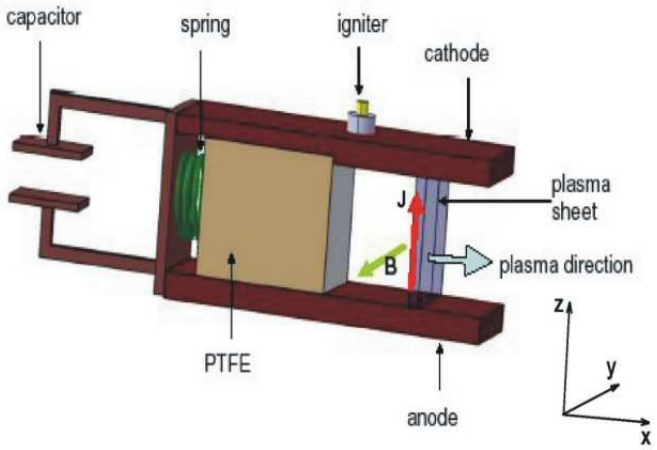

Figure 1.1. Schematic representation of a PPT. Technical specifications [3]: Voltage: 1500,1800,2000 V; Capacitance: 40 μF; Electrodes width: 20,40,60 mm; Distance between the electrodes: 21,36,42 mm

tential difference that ablates a layer of the block of Teflon (PTFE), also by the help of a common sparkle. The originated plasma consists typically of electrons and heavy particles

(neutrals, positives and negatives) in quasi neutrality condition. The charged particles will accelerate because of the electric fields and will self-induce a magnetic field. The Lorentz force that is born by the interaction of the electric and magnetic fields will push the particles outside of the truster. The change in momentum gained by the particles will results in an equal and opposite reaction on the spaceship. Despite its simplicity, several physical mechanisms taking place during its operation need deeper investigation and even some of its working principles are not totally understood. Numerical simulation becomes mandatory in flanking experimental work for the optimisation of the thruster. Apart some confined regions close to the propellant surface, non- equilibrium conditions and discontinuities are expected essentially everywhere. The solution of the complete Boltzmann equation by means of particle methods is the task that IRS together with IAG (Institute for Aerodynamics and Gas Dynamics, University of Stuttgart), HLRS (High Performance Computing Center Stuttgart) and IHM (Institute for Pulsed Power and Microwave Technology, Research Center Karlsruhe) want to accomplish. Elastic and inelastic collisions can modify the quasi-neutral environment and heavy charged particles can distribute around the spacecraft causing sputtering and contamination. Therefore the original Particle-In-Cell (PIC) scheme developed by IHM [4, 5] is being extended by adding models for intra- and inter-species charged particle collisions and intermolecular reactions (see Figure 1.2) giving light to a new hybrid PIC/DSMC (Direct Simulation Monte Carlo) code named PicLas [6, 7]. The block diagram in Figure 1.2 illus-

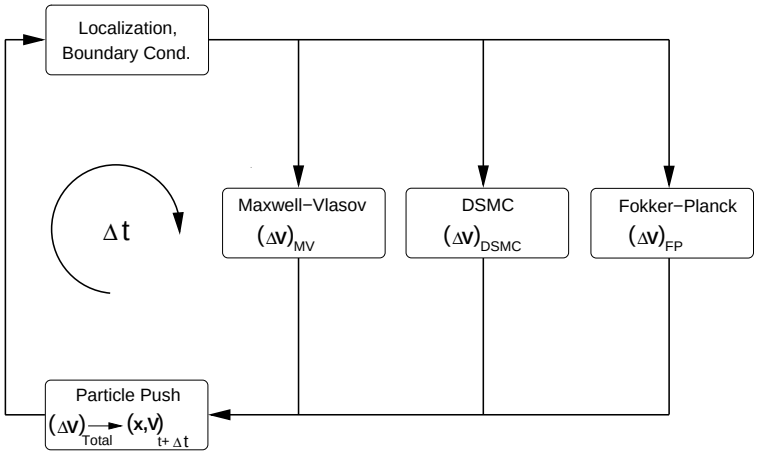

FIGURE 1.2. Schematic view of the coupling concept

trates schematically the working principles of the new code. First of all it is worthwhile to remark how the general program structure allows for a flexible combination of the different modules which can be run in parallel mode, each to contribute to the final $\Delta\vec{V}$.
The Maxwell-Vlasov solver models the interactions between charged particles and electromagnetic fields. Momentum and energy exchanges, without consideration of Lorentz force, as well as chemical reactions are treated in DSMC block, by means of a DSMC method based on the previous "LasVegas" code [8]. Finally, the effects of electrons and ions collisions on their velocity field are evaluated in the completely new Fokker-Planck solver, which adopts

PIC techniques in velocity space. The integration of these three modules is expected to allow for an accurate prediction of the behaviour of electric space propulsion systems operating far from continuum hypotheses. Additionally, the necessity of a three dimensional and time accurate description and complex geometries requires optimisation and parallelisation of the code in order to efficiently use high performance computers. The interplay of the different building blocks will be investigated and analysed in detail. Due to the multi-scale nature of the problem, the requirements for time step size, mesh size w.r.t. mean free path length, the maximum or minimum number of particles per cell might be competing, and systemic rules for stable, accurate settings are under development.

The objective of this work is to describe Coulomb interaction between charged particles like electron-electron collisions which play an important role in many application areas of plasma physics and accelerator physics. Due to the long-range nature of this force, there is a fundamental difference in treating these collisions compared to short-range reactions in the Boltzmann approach of dilute gases and plasmas, where different kind of hard sphere models are important tools of description [9]. The purpose of the present work is to introduce the Fokker-Planck approach for charged particle interaction in PIC simulation, where the impact parameter is usually large and, consequently, the deflection per collision is small. The diffusion approximation of the Boltzmann collision integral is customary to describe electron-electron interactions in a plasma, which mainly determine the shape of the electron energy distribution function (EEDF). In the case where the energy input into the plasma goes primarily into the thermal part of the EEDF, the high-energy tail is mainly populated by energy up-scattering caused by these collisions. It is clear from energetic considerations, that the high-energy tail also controls reactions like atomic excitation and ionisation – the energy sinks for electrons – and to some extent the plasma chemistry. Furthermore, the electron-electron collisions always drive the EEDF towards a Maxwellian distribution. Due to the important role of the EEDF for the plasma properties it is essential to model electron-electron collisions as realistic as possible.

2. Classical Particle-In-Cell Method. A short review

2.1. **Introduction.** The *P*article-*I*n-*C*ell approach (PIC) is particularly adept at modelling low pressure systems in which the matter density is $\varrho \lessapprox 10^{18}\,\mathrm{m}^3$; in this sense, it complents fluid methods which deal well with coherent behaviour of bulk population, but are not so useful to determine non-linear behaviour of small sub-groups, like the heating of a small fraction of the electron density in the sheet.

It is seems appropriate here to sketch out the main features of this approach and describe some theoretical aspects on which the core of this work is based. Generally speaking the PIC method refers to a technique used to solve a certain class of partial differential equation in which individual particles (or "representants") in a Lagrangian frame are tracked in continuum phase space, whereas moments of the distribution function are evaluated on Eulerian mesh points. The following procedure exploits what said above:

(1) Integration of equation of motion of particles
(2) Interpolation of the source terms to the field mesh
(3) Computation of the fields on mesh points
(4) Interpolation of the fields from the mesh to the particles locations

With this in mind, it is clear that one of the major problem suffered by PIC applications is the statistical noise, due to the relatively small number of particles they can deal with (typically $\leq 10^6$). Finally, it is worthwhile to remark another pecularity of this technique: the so-called macro- (or super-)particles. Actually, an exact description of a physical phenomenon describable through the approach on hand would involve a calculation of the interactions between all the physical particles and eventually the external fields, a prohibitive task for any computer. Modern computers are still not enough powerful to simulate all of the physical particles in even a low density plasma, for example. In fact, the particles P_i represented on the computational domain are actually phase fluids elements, or samples of different species of particle, each "containing"

$$N_{i,\alpha} = \int_{P_i} \int f_\alpha(\mathbf{x}, \mathbf{w}, t)\, d^3x\, d^3w \tag{1}$$

constituents for the specie α ; here, f_{alpha} denotes the distribution function, while $\mathbf{x}$ and $\mathbf{w}$ are the phase-space coordinates.

It is straightforward to apply the previous general considerations to non-equilibrium plasmas, for example, in which the particle distribution are not solely a function of the local fields. They have been used to reproduce in extremely accurate manner, experimental measurements of non-Maxwellian electrons and ions distribution. Moreover, PIC codes are widely used for modelling a variety of plasma types and conditions including radio-frequency systems. Charged plasma species are modelled as individual macro-particles which move in the computational domain in response to self-consistently calculated electromagnetic-fields and possibly applied external fields. Two important facts must be remarked:

(1) A macro particle P_i moves in the same way as single plasma particle, because the ratio $Q_i/M_i = q_\alpha/m_\alpha$ is independent of the number of constituents $N_{i,\alpha}$
(2) Point particle representation is still possible as long as quantum mechanical effects are negligible.

These and other extended concepts were applied in the 1990s (see, e.g. [10, 11]) for the simulation of pulsed power ion diodes and were developed and improved in the PicLas project since three years to fit in the frame of the project for the simulation of a space thruster. Finally, note that standard PIC codes are not able to catch charged particles collisions because of the averaging and subsequent assignment procedure on the volumes vertices; i.e., the Coulomb fields of the particles inside a cell cancel one another out. For this reasons they are not recommended in situations were collisions dominate, as in rarefied gas flows.
Ironically, it is possible to treat Coulomb collisions making use of the PIC philosophy as it will be shown in the next chapters. In order to get a better understanding of the following topics, it is therefore necessary to give here a short review of the PIC approach, for instance done also in [12] where the PIC technique was applied to the simulation of a non-neutral, collisionless plasma. Therefor which the Maxwell-Vlasov equations are sufficient for an accurate physical-mathematical description. Munz, C.-D. and Roller, S. and Schneider, R.

2.2. **The Maxwell-Vlasov Equation.** Computational simulations of devices whose behaviour is substantially influenced by charged particle flow are important in applied science and technology. A detailed understanding of the phenomena caused by such a non-neutral plasma requires the solution of the Maxwell-Vlasov equation given by

$$\frac{\partial f_\alpha}{\partial t} + \mathbf{c}_\alpha \cdot \nabla_x f_\alpha + \frac{\mathbf{K}_\alpha}{m_\alpha} \cdot \nabla_c f_\alpha = 0 \,, \tag{2}$$

and describes the evolution of the distribution function $f_\alpha = f_\alpha(\mathbf{x}, \mathbf{c}, t)$ in phase space for specie "α". According to the law of dynamics for charged particles with charge q, the force $\mathbf{K}_\alpha$ in equation (2) is given by the Lorentz force

$$\mathbf{K}_\alpha \quad = \quad q_\alpha \left[\mathbf{E}(\mathbf{x}, t) + \mathbf{c} \times \mathbf{B}(\mathbf{x}, t)\right] \,, \tag{3}$$

on charge q_α with mass m_α and depends on the velocity $\mathbf{c}$, the electric field $\mathbf{E}$ and the magnetic induction $\mathbf{B}$. Note that in the case of highly rarefied plasma flow the collision term of the Boltzmann equation can be neglected and (2) is also known as collisionless Boltzmann equation. In the terminology of hyperbolic partial differential equations, the general solution of (2) is given by its characteristics

$$\frac{d\mathbf{p}_\alpha(t)}{dt} = \mathbf{K}_\alpha(\mathbf{c}_\alpha, \mathbf{x}_\alpha, t) \quad \text{and} \quad \frac{d\mathbf{x}_\alpha(t)}{dt} = \mathbf{c}_\alpha(t) \tag{4}$$

and are called Lorentz equations in the following. Here, the relativistic momentum is given by $\mathbf{p}_\alpha = m_\alpha \gamma \mathbf{c}_\alpha$ with the Lorentz factor $\gamma^2 = 1 + (\mathbf{p}_\alpha)^2/(m_\alpha c)^2$, where c_0 denotes the speed of light. The difficulties in solving the Lorentz equations arise from the fact that $\mathbf{E}$ and $\mathbf{B}$ are not given explicitly. In fact, they have to be calculated at each time step in a self-consistent

manner [13, 14] from the full set of Maxwell equations. This system consists of the two hyperbolic evolution equations

$$\frac{\partial \mathbf{E}}{\partial t} - c^2 \nabla \times \mathbf{B} = -\frac{\mathbf{j}}{\epsilon_0} \tag{5}$$

$$\frac{\partial \mathbf{B}}{\partial t} + \nabla \times \mathbf{E} = 0 \tag{6}$$

(Ampère's and Faraday's law) and the elliptic parts

$$\nabla \cdot \mathbf{E} = \frac{\rho}{\epsilon_0}, \quad \nabla \cdot \mathbf{B} = 0 \tag{7}$$

(Gauss' law and the statement about the absence of magnetic monopoles), where the electric permittivity ϵ_0 and magnetic permeability μ_0 are related to the speed of light in vacuum c_0 according to $\epsilon_0 \mu_0 {c_0}^2 = 1$. For given charge and current densities ρ and $\mathbf{j}$, the Maxwell equations describe the temporal and spatial evolution of the electric field and the magnetic induction. With an integration over the entire momentum space, the self-consistent parts of the charge ρ and current density $\mathbf{j}$ are obtained from (see e.g. [4])

$$\rho = \sum_\alpha q_\alpha \int f_\alpha(\mathbf{x}, \mathbf{p}, t) d^3p \quad \text{and} \quad \mathbf{j} = \sum_\alpha q_\alpha \int \mathbf{c}_\alpha(\mathbf{p}) f_\alpha(\mathbf{x}, \mathbf{p}, t) d^3p. \tag{8}$$

Up to this point, the description is exact in the sense that no numerical approximations are made. For the numerical realization of the Maxwell-Vlasov system, (also called Maxwell-Lorentz system) the Particle-In-Cell method is applied [14, 13]. In this context f_α is expressed by a weak approximation [4], yielding the following expressions for charge and current density

$$\rho^* = \sum_i q_\alpha \sum_{k=1}^{N_\alpha} \delta \left[\mathbf{x} - \mathbf{x}_\alpha^{(k)}(t) \right] \tag{9}$$

$$\mathbf{j}^* = \sum_i q_\alpha \sum_{k=1}^{N_\alpha} \mathbf{c}_\alpha^{(k)} \delta \left[\mathbf{x} - \mathbf{x}_\alpha^{(k)}(t) \right], \tag{10}$$

where the superscript (k) denotes the k^{th} particle of specie α, N_α is the total number of particles within this group and δ represents the usual Dirac function. For each grid node, all particles in the surrounding cells are considered. In order to determine the contribution of all charged particles, shape-functions are used to calculate ρ and $\mathbf{j}$ at the grid nodes. With these charge and current densities the new electromagnetic fields are computed at the nodes and afterwards interpolated to the local particle postions [12]. This procedure, which is schematically depicted in Figure 2.1, has to be repeated at each time step.

A direct consequence of the charge conservation equation $\frac{\partial \rho}{\partial t} + \nabla \cdot \mathbf{j} = 0$ and of the divergence of the curl for any differentiable vector field being zero is that the divergence constraints (7) are satisfied at all times, if the initial values satisfy these relations. In this case, it would be sufficient to solve the hyperbolic evolution equations (5) and (6) only. Unfortunately, numerical errors may occur in the simulation: The divergence of a curl may be zero up to some error terms only and interpolation errors in the particle treatment may arise. This leads to small errors being introduced at each time step. If only the hyperbolic evolution equations are numerically solved, then these errors may increase and strongly falsify the solution. For

a self-consistent movement of charged particles, the Gauss law and the statement about the absence of magnetic monopoles (7) have to be coupled with Ampère's and Faraday's law. In the Generalised Langrange Multiplier approach [15, 16, 17], two additional variables $\Phi(\mathbf{x},t)$ and $\Psi(\mathbf{x},t)$ are introduced into the Maxwell equations to couple the evolution equations for the electromagnetic fields (5) and (6) with their elliptical constraints (7). The coupling terms may be chosen in a way that allows a purely hyperbolic system to be formed. If the errors are zero it coincides with the original Maxwell equations. The purely hyperbolic Maxwell equations system reads as

$$\frac{\partial \mathbf{E}}{\partial t} - c^2 \nabla \times \mathbf{B} + \chi c^2 \nabla \Phi = -\frac{\mathbf{j}}{\epsilon_0}, \tag{11}$$

$$\nabla \cdot \mathbf{E} + \frac{1}{\chi}\frac{\partial \Phi}{\partial t} = \frac{\rho}{\epsilon_0}, \tag{12}$$

$$\frac{\partial \mathbf{B}}{\partial t} + \nabla \times \mathbf{E} + \gamma \nabla \Psi = 0, \tag{13}$$

$$\nabla \cdot \mathbf{B} + \frac{1}{\gamma c^2}\frac{\partial \Psi}{\partial t} = 0, \tag{14}$$

where the dimensionless positive parameters χ and γ represent the transport coefficients for the local errors Φ and Ψ. Obviously, these new variables $\Phi(\mathbf{x},t)$ and $\Psi(\mathbf{x},t)$ define two additional degrees of freedom and couple the divergence conditions (7) to the evolution equations (5), (6). This correction technique ensures that the divergence errors arising from the *div curl* as well as from the charge conservation violation within an electromagnetic PIC computation cannot increase and falsify the numerical simulation results. Keep in mind that explicit numerical methods for the Maxwell equations in time domain can be properly combined with a hyperbolic divergence correction in a straightforward manner, yielding a very efficient and highly flexible Maxwell solver module for PIC applications on unstructured grids and for parallel computing [18].

2.3. **Numerical Scheme.** As previously mentioned, an attractive numerical method to solve the non-linear Maxwell-Lorentz problem is the PIC method based on ingenious particle-mesh techniques (see Fig. 2.1). The basic ideas can be summarised as follows: the plasma inside a device is represented by a sample of charged particles. In each time step the electromagnetic fields obtained by the numerical solution of the Maxwell equations (eqns. (5) and (6)) are interpolated to the actual locations of these charged particles. According to the Lorentz force (3) the charges are re-distributed and the new phase space coordinates are determined by solving numerically the usual laws of dynamics. To close the chain of self-consistent interplay the particles have to be located with respected to the computational grid in order to determine the contribution of each charged particle to the changed charge and current density being the sources for the Maxwell equations in the subsequent time-step.
Traditional techniques for solving the Maxwell equation rely on the finite-difference methods which maybe traced back to Yee [19] and were applied to PIC computations by [10, 11, 20]. In the context of PIC code design at IHM and IAG, high resolution explicit finite-volume schemes are developed and applied as Maxwell solvers [4, 21, 15]. Other numerical methods

for the Maxwell equations like finite-elements techniques were introduced e.g. in [22]. Very recently, arbitrary high order accurate ADER [23] and discontinuous Galerkin methods [18, 24] methods are proposed and developed for the numerical solution of Maxwell equations in PIC simulations.

The discretisation of the relativistic equation (4) as well as its non-relativistic counterpart has been extensively investigated in literature [13, 25, 14]. The most "popular" approach for the numerical solution of the momentum equation is the leapfrog scheme introduced by Boris [25]. Recently, new techniques for charged particle movement are discussed which allow high-order discretisation of the relativistic equation [26, 27] and seem to be an important contribution for high-order self-consistent PIC simulations.

Clearly, the Maxwell solver is a grid-based module for structured or unstructured mesh arrangements while particle movement is performed in the mesh-free domain. In the following, we briefly discuss the two interfaces between grid-based and mesh-free computations which are the charge and current density *assignment* and the *interpolation* of the actual position, where we assume an unstructured computational mesh.

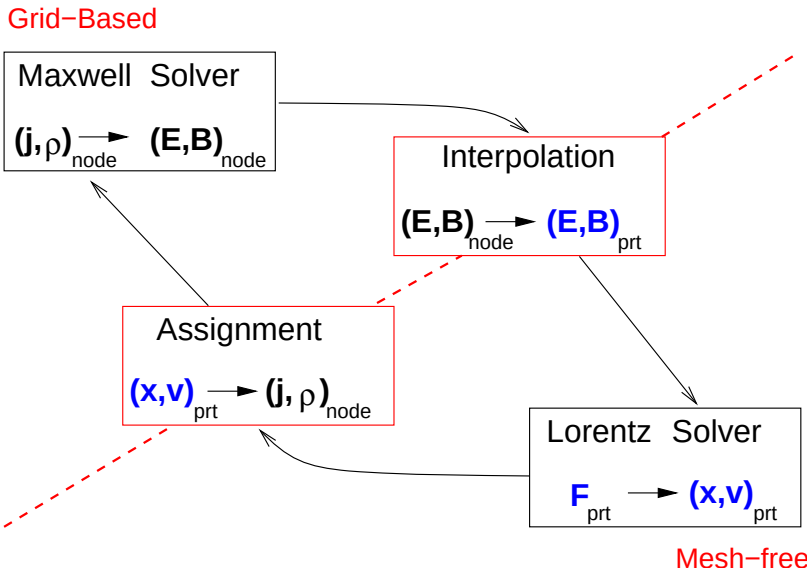

FIGURE 2.1. The different building blocks for a typical PIC Simulation code

Essentially some form of interpolation among the grid points "surrounding" the particles is required to link the "mesh-free" and the "grid-based" zone of the loop [12]. As always there is a trade-off between computational efficiency and accuracy. The simplest and fastest weighting procedure is called zeroth order or nearest-grid point (NGP) weighting. In this system particles are simply assigned to the nearest grid point and the resolution to which a particle can be tracked as far as the grid is concerned is limited to the distance between grid points. From grid's point of view when a particle moves in through one wall the density jumps up sharply and as the particle leaves through another wall the density drops sharply.

The particle then appear to have a rectangular shape with width $\triangle$x. Because the density changes so abruptely at grid points, zeroth order weighting might results in noisy electric and magnetic fields.

A first order procedure which fits particularly good for unstructured grid is the "node-domain assignment". Suppose that the contribution of a macro particle k at the phase space position $(\mathbf{x}_k(t), \mathbf{c}_k(t))$ to the current and the charge density is to be calculated at the node i and $S_i^k = S_i(x_k(t))$ is the related shape function. The node connects a certain number of elements forming the local node domain Ω_i (see Fig. 2.2). This task is accomplished calculating the shape function $S_i = S_i(\mathbf{x}(t))$ [12]. The contribution of the kth charged macro particle at the

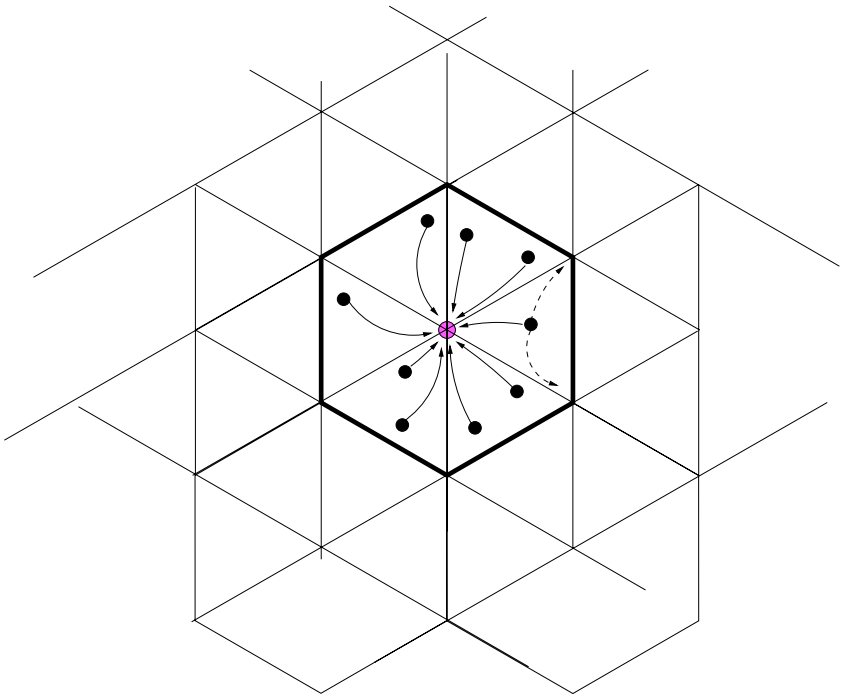

FIGURE 2.2. The local node domain assignment

node i is obtained from

$$\rho_k(t) = \frac{Q_k}{V_i} S_i^{(k)} \tag{15}$$

$$\mathbf{j}(t) = \frac{Q_k \mathbf{c}_k}{V_i} S_i^k \tag{16}$$

where V_i is the volume associated with the node i. From the perspective of the grid each particle is now a cloud with peak density at the position of the particle. Higher order weighting ([14]) make use of quadratic and cubic spline to further round-off the roughness in particle shape and reduce density and field noise, at the cost of more computation.

The above numerical framework has been used in PicLas to model charged particle movement

in electromagnetic fields [28, 27]; these concepts are at the basis of the development of the PIC module for modelling Coulomb collisions in low pressure plasma. The only difference lies in the nature of the equation to be integrated.

3. Coulomb Collisions and Fokker-Planck Model

3.1. **Introduction.** Being essentially an ensemble of positive, negative and neutral particles which co-exist together, plasmas can appear in a large variety of conditions and states. By some estimates 99 % of the observable universe is in the plasma state, with the exception of the Earth since it is not a favourable environment for its too low temperature and its too high matter density. Nonetheless, plasma can exist at low (laboratory) temperatures, provided a mechanism for ionisation and a sufficiently low pressure to avoid recombination.
Depending on the situation on hand, different approaches and consequently approximations can be used to simulate plasma behaviour. If only time scales much larger than the relaxation times are of interest, an equilibrium, namely Maxwellian distribution function for the electrons can be assumed and the moments of the distribution function can be integrated to get conservation laws. This so-called fluid theory is successfully applied also under conditions of high pressure and high density where the motion of single particles is not a concern. On the contrary, in the cases of non-equilibrium, low pressure and/or low densities a kinetic -particle motion - approach is adequate. The latter description is based and encompasses appropriate averages of the motion of all the individual charged particles in plasma.
The role of collisions deserves a separate discussion, because they can completely change the physical-mathematical model, according to their relative importance. They are totally negligible if the Coulomb potential is much smaller than the thermal kinetic energy, because Coulomb cross section decreases with increasing temperature. Fusion plasmas, in fact, are considered collisionless. This implies that the collisional effects are less important than the collective effects, i.e. the cumulative under λ_D-scale events are negligible in comparison with over λ_D-scale, with λ_D the Debye length. In formulas

$$\frac{2\pi\nu_c}{\omega_{pc}} \propto \frac{nln\Lambda}{\sqrt{n}} \propto \frac{1}{N_D} lnN_D \tag{17}$$

and

$$n\lambda_D \propto \frac{T^{3/2}}{n^{1/2}} \tag{18}$$

where ν_c is the collision frequency, $T = T_i = T_e$ is the temperature of an isothermal plasma, ω_{pc} is the typical plasma frequency, n is the plasma density, $ln\Lambda$ is the Coulomb logarithm and finally N_D is the number of particles in a Debye sphere. Some interesting considerations follow: a collisionless system (ν_c decreases with the density) has a very large number of particles in a Debye sphere and a collisional one has few but still enough not be classified as rarified and binary collisions would totally dominate the dynamics [29].

3.2. **Governing Equation.** From the description of the PPT the necessity of solving the fundamental plasma kinetic equation emerges [30, 31]

$$\frac{\partial f_\alpha}{\partial t} + \mathbf{c} \cdot \nabla_x f_\alpha + \frac{\mathbf{K}}{m_\alpha} \cdot \nabla_c f_\alpha = C(f) \,, \tag{19}$$

to describe the evolution of the distribution function $f_\alpha = f_\alpha(\mathbf{x}, \mathbf{c}, t)$ of a generic plasma specie "α" in phase space. Here, $\mathbf{K} = \mathbf{K}(\mathbf{x}, \mathbf{c}, t)$ represents the electromagnetic force acting on the particles of the ensemble "α" with charge q_α and mass m_α. The term on the right-hand side (rhs) of equation (19) is the so-called operator which reflects the rate of change with respect to time of f_α due to collisions. As first approximation it is possible to consider only elastic, two-body collisions including charged and neutral particles which results into the Boltzmann operator

$$\begin{aligned} \mathcal{C}(f) &= \mathcal{C}_B(f) = \qquad (20) \\ \left(\frac{\delta f_\alpha}{\delta t}\right)_{col} &= \sum_\beta n_\beta(\mathbf{x}, t) \int d^3w \, d\Omega \, g \, Q_{\alpha\beta} \left[\Phi_{\alpha\beta}(\mathbf{c}', \mathbf{w}') - \Phi_{\alpha\beta}(\mathbf{c}, \mathbf{w})\right], \end{aligned}$$

where $\Phi_{\alpha\beta}(\mathbf{c}, \mathbf{w}) = f_\alpha(\mathbf{c}) \, f_\beta(\mathbf{w})$ is the product of the particle distribution functions of the particle species involved in the process. Here, the index β runs over all "scattering" populations (field particles), n_β is the local number density of the field particle specie "β", $g = |\mathbf{g}| = |\mathbf{c} - \mathbf{w}|$ is the absolute value of the relative velocity, $Q_{\alpha\beta} = Q_{\alpha\beta}(g, \chi, \varphi)$ is the differential scattering cross section (see App. B) (in the center-of-mass system) between the particles of the species "α" and "β" and the element of solid angle $d\Omega$ is given by $d\Omega = \sin\chi \, d\chi \, d\varphi$ (χ: scattering angle, φ: azimuthal angle). Moreover, the prime refers to the value of a quantity after a collision and unprimed denotes the values before the collision. In this case equation (19) is called Boltzmann equation.

A rigorous mathematical description of that can be obtained by the so-called **BBGKY** theory [32]. It essentially casts the Liouville equation into a chain of equations where the first equation connects the evolution of one particle density propability with the two particle density probability function, and similarly the i-*th* equation connects the i-*th* particle and the (i+1)-*st* particle density probability function. Approximations of the **BBGKY** chain, like truncation usually at the level of the first or first two equation lead to the Vlasov or to the Boltzmann equation. Moreover, under the assumption that the probability density is a function of only the relative distance, the hydrodynamic equations are obtained.

In many practical situations, ambient conditions like the supposedly SIMPLEX operation conditions [33] require an accurate description of both elastic and inelastic particle interactions, that is in a certain sense to include some chemistry. From now on, attention will be devoted exclusively to those phenomena involving only elastic charged particle interactions.

3.3. **From the Boltzmann to the Fokker-Planck Collision Operator.** So far, the defined area of interest is the analysis of the effects of collisions on a charged particle velocity distribution in a quasi-neutral plasma. Since the plasma properties are such that a classical depiction is sufficient, the starting point for the mathematical formulation of the problem is equation (19) that, once again, consider only binary interactions. Some simplifying hypotheses follow. Scattering angles are supposed to be small, a reasonable conjecture in the case of $N_D >> 1$; the Coulomb potential for the scattered particle is cut off at distances larger than

the Debye length, i.e.

$$\begin{aligned} \Phi(r) &= \frac{Ze^2}{4\pi\varepsilon_0 r}\,, r < \lambda_D\,, \\ \Phi(r) &= 0\,, r > \lambda_D\,; \end{aligned} \tag{21}$$

no collision takes place for $b > \lambda_D$, b being the impact parameter or the distance of closest approach; during a collision the surrounding particles are viewed as rearranging themselves so that the two particles interact in accordance with (21). Under these statements it is possible to develop $f_\alpha(\mathbf{c})$ and $f_\beta(\mathbf{w})$ in (19) in Taylor's series performing integration over the angles (see App. A) and finally get [30, 34]

$$\mathcal{C}_B \approx \mathcal{C}_{\alpha\beta} = \tag{22}$$

$$\left(\frac{\delta f}{\delta t}\right)_\alpha = \sum_\beta \Gamma_P^{(\alpha\beta)}\, n_\beta \left\{ -\frac{\partial}{\partial c_p}\left[\frac{\partial \mathcal{H}^{(\beta)}}{\partial c_p}\, f_\alpha\right] + \frac{1}{2}\frac{\partial^2}{\partial c_p \partial c_q}\left[\frac{\partial^2 \mathcal{G}^{(\beta)}}{\partial c_p \partial c_q}\, f_\alpha\right]\right\}.$$

.

This collision term, also known as Fokker- Planck collision operator and equation (22) is usually referred as Fokker-Planck FP equation. It represents the lowest order approximation of the Boltzmann collision integral and importantly involves the cumulative effects of multiple small angle, elastic (energy preserving), charged particle collisions within a Debye sphere. Note that the FP model retains the significant properties of the Boltzmann integral [35], namely, the mass, momentum and energy conservation as well as the H-theorem, which states the fact that an arbitrary initial particle distribution is always driven to a Maxwellian. $\mathcal{H}$ and $\mathcal{G}$ are known as Rosenbluth potentials and are defined as

$$\mathcal{H}^{(\beta)}(\mathbf{x}, \mathbf{c}, t) \equiv \frac{m_\alpha}{m_{\alpha\beta}} \int_{-\infty}^{\infty} \frac{f_\beta(\mathbf{x}, \mathbf{w}, t)}{|\mathbf{g}|}\, d^3 w\,, \tag{23}$$

$$\mathcal{G}^{(\beta)}(\mathbf{x}, \mathbf{c}, t) \equiv \int_{-\infty}^{\infty} |\mathbf{g}|\, f_\beta(\mathbf{x}, \mathbf{w}, t)\, d^3 w\,, \tag{24}$$

where $1/m_{\alpha\beta} = 1/m_\alpha + 1/m_\beta$ is the reduced mass of the species "α" and "β". Their name comes from the property that these two quantities and the distribution function fulfil:

$$\nabla_c^2\, \mathcal{H}^{(\beta)}(\mathbf{x}, \mathbf{c}, t) \propto f_\beta(\mathbf{x}, \mathbf{c}, t) \tag{25}$$

and

$$\nabla_c^2\, \mathcal{G}^{(\beta)}(\mathbf{x}, \mathbf{c}, t) \propto \mathcal{H}^{(\beta)}(\mathbf{x}, \mathbf{c}, t)\,, \tag{26}$$

which means that they satisfy a Poisson equation with sources f_β and $\mathcal{H}^{(\beta)}$, respectively. Probably the most meaningfull aspect is actually the relation that links their derivatives to the dynamical friction $F_p^{(\alpha)} = F_p^{(\alpha)}(\mathbf{x}, \mathbf{c}, t)$ (unit: $[m/s^2]$) and diffusion coefficient (evaluated

first by Chandraseaker in [36]) $D_{pq}^{(\alpha)} = D_{pq}^{(\alpha)}(\mathbf{x}, \mathbf{c}, t)$ (unit: $[m^2/s^3]$)

$$F_p^{(\alpha)} = \sum_\beta \Gamma_P^{(\alpha\beta)}\, n_\beta(\mathbf{x}, t)\, \frac{\partial \mathcal{H}^{(\beta)}}{\partial c_p} \tag{27}$$

and

$$D_{pq}^{(\alpha)} = \sum_\beta \Gamma_P^{(\alpha\beta)}\, n_\beta(\mathbf{x}, t)\, \frac{\partial^2 \mathcal{G}^{(\beta)}}{\partial c_p \partial c_q}\,, \tag{28}$$

respectively, where the index "β" runs over all "scattering" populations (also called field particles). Here, $n_\beta(\mathbf{x}, t)$ represents the local density of the scatterer,

$$\Gamma_P^{(\alpha\beta)} = \frac{q_\alpha^2 q_\beta^2}{4\pi\epsilon_0^2 m_\alpha^2} \ln(\Lambda) \tag{29}$$

is the plasma parameter [31] in SI-units ($[\mathrm{m}^6/\mathrm{s}^4]$). Note, that the factor $\overline{\nu}_{\alpha\beta} = n_\beta\, \Gamma_P^{(\alpha\beta)} \,/\, v_{\mathrm{th}}^3$ may be considered as an energy-weighted average of the speed-dependent momentum transfer collision frequency (cf. [34]) between the particles of the species "α" and "β", where the thermal velocity is defined by $v_{\mathrm{th}}^2 = k_B\, T_\beta \,/\, m_\beta$. Note that equation (22) is the evolution equation for a two species system only due to collisions, that is in absence of spatial gradients of f – like in a reservoir – and in those situation where the smoothed electromagnetic force is negligible with respect to collisions as for example in cold plasmas.

Analytical solutions of the FP equation are available only for very special cases of the friction force and diffusion tensor. For instance, the short-time solution of the FP equation is obtained if one assumes that the friction and diffusion coefficients weakly depend on the velocity (see App. C). A further analytical solution is known for the Lenard-Bernstein model (also called Ornstein-Uhlenbeck process) which is established by $\mathbf{F} = \mathbb{A}(\mathbf{x}, t) \cdot \mathbf{c}$ ($\mathbb{A}$ is a matrix) and $\mathbb{D} = \mathbb{D}(\mathbf{x}, t)$ (see, e.g. [37, 38, 39, 29] and App. D). In general, the FP model represents a complicated nonlinear problem which has to be solved numerically in an appropriate – namely, self-consistent – manner.

To introduce the numerical method adopted for solving the FP problem it is instructive to explore the results obtained by reducing the original problem because it contains the essential characteristics of the main problem despite its relative simplicity. The intra-species collision case – test particles and scatterers are identical – is the starting point for the following discussion.

3.4. **The Isotropic Field Particle Distribution Hypothesis.** The approximations and assumption illustrated in this section both provide a first insight into the collisional phenomena and base a benchmark problem for the validation of the numerical model. It is well known that the assumption of an isotropic but non-Maxwellian velocity distribution of the field particles implies an enormous reduction of the three dimensional problem [34, 40, 41]. It is important to point out that the problem remains three-dimensional but the angular dependency of the distribution function is dropped. We consider intra-species scattering of charged particles (for instance, electrons) and suppress the species indices "α" and "β". The assumption of isotropic velocity distribution function f ($= f_\beta$) of the scatterer means that f depends only on the absolute value $w = |\mathbf{w}|$ of the field particle velocity: $f = f(w)$. In order

to compute the integrals (24) and (27), we introduce spherical coordinates in velocity space and replace $|\mathbf{c}-\mathbf{w}|$ by

$$|\mathbf{c}-\mathbf{w}| = \sqrt{c^2+w^2-2cw\cos\Theta}\,.$$

The integration over the azimuthal angle Φ and the polar angle Θ yields the results (cf., [30, 34, 40])

$$\mathcal{H}(\mathbf{x},c,t) = 8\pi\left\{\frac{1}{c}\int\limits_0^c w^2\, f\, dw + \int\limits_c^\infty w\, f\, dw\right\} \tag{30}$$

and

$$\begin{aligned}\mathcal{G}(\mathbf{x},c,t) &= 4\pi\left\{\frac{1}{3c}\int\limits_0^c w^4\, f\, dw + c\int\limits_0^c w^2\, f\, dw\right.\\ &+ \left.\int\limits_c^\infty w^3\, f\, dw + \frac{c^2}{3}\int\limits_c^\infty w\, f\, dw\right\},\end{aligned} \tag{31}$$

where $f = f(\mathbf{x},w,t)$. To calculate the derivatives of the isotropic potentials in velocity space with respect to the velocity c_p, we use the fact that $\frac{\partial c}{\partial c_p} = \frac{c_p}{c}$ and get the equations

$$\frac{\partial\mathcal{H}(\mathbf{x},c,t)}{\partial c_p} = \frac{\partial\mathcal{H}(c)}{\partial c}\,\hat{c_p} \tag{32}$$

and

$$\frac{\partial^2\mathcal{G}(\mathbf{x},c,t)}{\partial c_p\partial c_q} = \frac{\partial^2\mathcal{G}(c)}{\partial c^2}\,\hat{c_p}\hat{c_q} + \frac{1}{c}\frac{\partial\mathcal{G}(c)}{\partial c}\left[\delta_{pq}-\hat{c_p}\hat{c_q}\right], \tag{33}$$

where δ_{pq} denotes the Kronecker symbol and $\hat{c_p}$ is the p^{th} component of the unit vector $\hat{c} = \mathbf{c}/c$. Then the friction and diffusion coefficients are given by

$$F(c) = n\,\Gamma_P\frac{\partial\mathcal{H}(c)}{\partial c} = -n\Gamma_P\frac{8\pi}{c^2}\int\limits_0^c w^2\, f\, dw\,, \tag{34}$$

$$D_\parallel(c) = n\,\Gamma_P\frac{\partial^2\mathcal{G}(c)}{\partial c^2} = n\Gamma_P\frac{8\pi}{3}\left\{\frac{1}{c^3}\int\limits_0^c w^4\, f\, dw + \int\limits_c^\infty w\, f\, dw\right\}, \tag{35}$$

$$\begin{aligned}D_\perp(c) = \frac{n\,\Gamma_P}{c}\frac{\partial\mathcal{G}(c)}{\partial c} &= n\Gamma_P\frac{4\pi}{3}\left\{\frac{1}{c^3}\int\limits_0^c (3c^2-w^2)\, w^2\, f\, dw\right.\\ &+ \left.2\int\limits_c^\infty w\, f\, dw\right\}.\end{aligned} \tag{36}$$

Clearly, if we identify $\hat{c}$ with the unit vector $\mathbf{e}_x$, then the matrix established by (33) have only non-vanishing diagonal elements. It is obvious, that the coefficients (34)-(36) are decreasing functions of c with high-velocity behaviour proportional $1/c^2$, $1/c^3$ and $1/c$, respectively. Consequently, friction and diffusion based effects like approach to equilibrium are much weaker at high energies of the particles. Furthermore note, that field particles with speed w greater than the speed c of the test particles do not contribute to the friction coefficient (34). This effect is a pecularity of Coulomb scattering off an isotropic

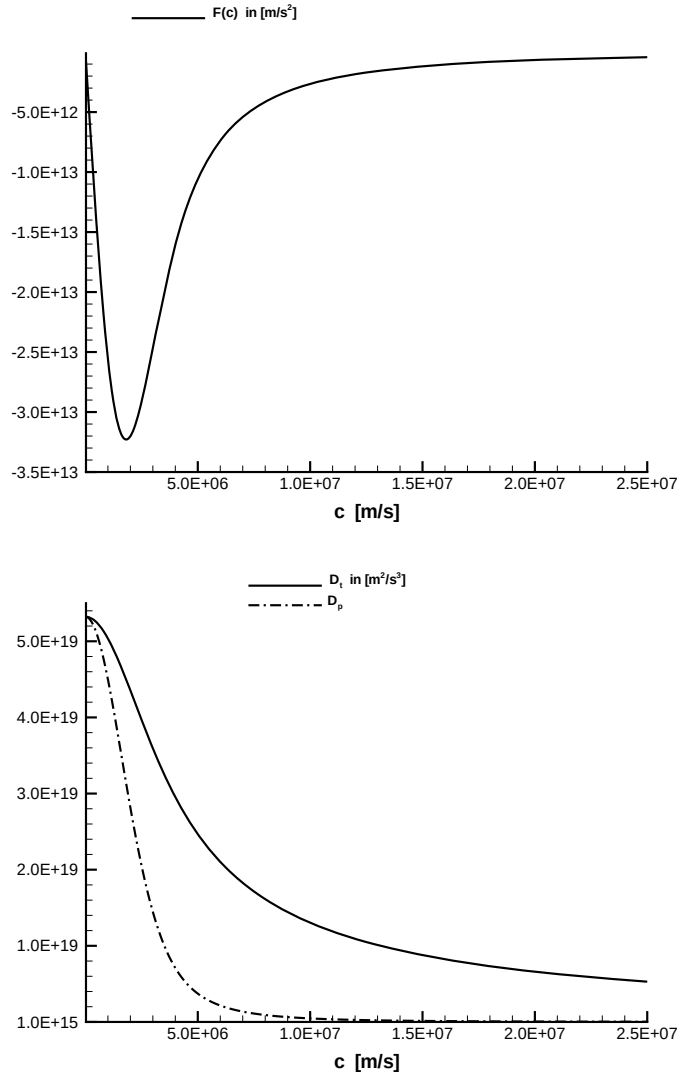

FIGURE 3.1. Dynamical friction (upper plot) and diffusion (lower plot) coefficients $D_\perp$ (full) and $D_\parallel$ (dashed-dotted line) as a function of velocity c.

distribution of scatterers. To get a quantitative picture, the friction and diffusion coefficients (34)-(36) are seen in Figure 3.1 as a function of the velocity c. For this, a Gaussian distribution function of the form $f(w) = \frac{2}{\sqrt{2\pi}\, v_{\rm th}^3} \exp\!\left(-\frac{w^2}{2v_{\rm th}^2}\right)$ with $v_{\rm th}^2 = k_B\, T/m_e$ is assumed for the field electron distribution, which possesses a constant number density $n_e = 10^{18}$ m^{-3} and a temperature $T_e^\star = 10$ eV. It is apparent from these plots, that the accurate velocity-dependence is very important for modelling these coefficients, especially in the low-velocity region. Furthermore, in Figure 3.2 we depict the dependence of the coefficients $|F(c)|$, $D_\perp(c)/c$ and $\sqrt{D_\parallel(c)}$ (see below) from the velocity c. Note, that these coefficients possess units of an "acceleration" and that $D_\perp(c)/c$ is the dominant contribution at very

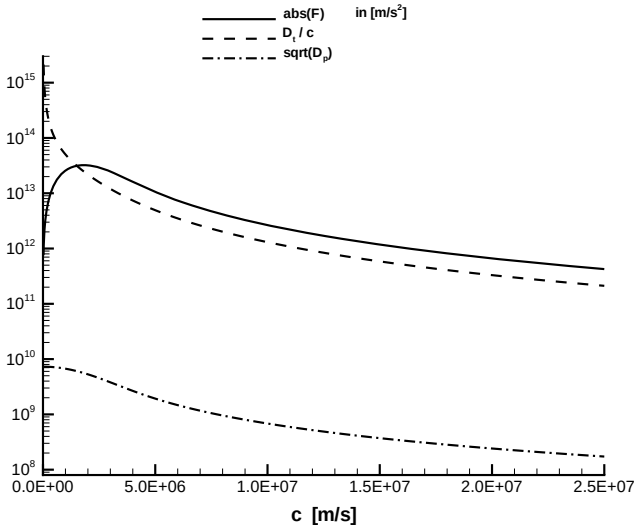

FIGURE 3.2. $|F(c)|$ (full line), $D_\perp(c)/c$ (dashed line) and $\sqrt{D_\parallel}$ (dash-dotted line) as a function of the velocity c. In all cases the unit is $[m/s^2]$.

small velocities, which is responsible that the particles diffuse up towards the thermal velocity $v_{\rm th}$ where they feel strong friction that tends to centre the velocity around the mean value.

3.5. FP **Equation in Spherical Coordinates.** More than a nice mathematical training, formulating the FP equation in spherical coordinate can be convenient in circumstances where the geometry requires it or where the only variables that counts is the modulus of the velocity, as it will be considered in chap. 6

As starting point the FP equation in covariant form is considered [42]

$$\partial_t f = -\Big[f\,F^\mu\Big]_{,\,\mu} + \frac{1}{2}\Big[f\,D^{\nu\mu}\Big]_{,\,\nu\,,\,\mu}\,, \tag{37}$$

which is valid for any set of curvilinear coordinates x^1, x^2 and x^3 in the non-relativistic case. Here, the commas indicate covariant derivatives with respect to x^μ, repeated Greek indices imply summation (Einstein's summation convention) and $f = f(x^1, x^2, x^3)$ is the particle distribution function. The covariant derivatives can be written as [43, 42]

$$\sqrt{g}\,\Big[f\,F^\mu\Big]_{,\,\mu} = \frac{\partial}{\partial x^\mu}\Big[\sqrt{g}\,f\,F^\mu\Big] \tag{38}$$

and

$$\sqrt{g}\,\Big[f\,D^{\nu\mu}\Big]_{,\,\nu\,,\,\mu} = \frac{\partial^2}{\partial x^\mu \partial x^\nu}\Big[\sqrt{g}\,f\,D^{\nu\mu}\Big] + \frac{\partial}{\partial x^\mu}\Big[\sqrt{g}\,f\,\Gamma^\mu_{\alpha\beta}\,D^{\alpha\beta}\Big]\,, \tag{39}$$

respectively, where $g = |g_{\mu\nu}|$ is the determinant of the metric tensor $g_{\mu\nu}$ and $\Gamma^\mu_{\alpha\beta}$ denotes the Christoffel symbol of second kind defined by (see, e.g. [44])

$$\Gamma^\gamma_{\alpha\beta} = \frac{1}{2}\,g^{\gamma\delta}\left(\frac{\partial g_{\alpha\delta}}{\partial x^\beta} + \frac{\partial g_{\beta\delta}}{\partial x^\alpha} - \frac{\partial g_{\alpha\beta}}{\partial x^\delta}\right), \tag{40}$$

which, in general, is not a tensor. Inserting (38) and (39) into equation (37), we get after some rearrangements

$$\partial_t \tilde{f} = -\frac{\partial}{\partial x^\mu}\Big[\tilde{f}\left(F^\mu - \frac{1}{2}\Gamma^\mu_{\alpha\beta}\, D^{\alpha\beta}\right)\Big] + \frac{1}{2}\frac{\partial^2}{\partial x^\mu \partial x^\nu}\Big[\tilde{f}\, D^{\nu\mu}\Big]\,, \tag{41}$$

where $\tilde{f} = \sqrt{g}\, f$. Obviously, in the latter equation the drift term (first term on the rhs) is modified by the geometry term $\frac{1}{2}\Gamma^\mu_{\alpha\beta}\, D^{\alpha\beta}$, which vanishes in the case of Cartesian coordinates. In the following we consider spherical polar coordinates in velocity space, where $x^1 = c$, $x^2 = \theta$ and $x^3 = \varphi$. The metric tensor $g_{\mu\nu}$ ($g = c^4 \sin^2\theta$), the physical components of the vector F^μ as well as the tensor $D^{\mu\nu}$ and the Christoffel symbols $\Gamma^\mu_{\alpha\beta}$ may be adopted from the literature [44], resulting in a quite lengthy expression for the rhs of (41). The first simplification of this expression is obtained by choosing the velocity difference vector $\mathbf{g}$ to be parallel to the unit basis vector $\mathbf{e}_c$. This leads to the fact that the vector $\mathbf{F}$ possesses only the component F_c and the tensor $\mathbb{D}$ is diagonal. Furthermore, assuming azimuthal symmetry, we obtain the equation

$$\begin{aligned}\partial_t \tilde{f} = \; &- \; \frac{\partial}{\partial c}\left\{\tilde{f}\left[F_c + \frac{1}{2c}\big(D_{\theta\theta} + D_{\varphi\varphi}\big)\right]\right\} + \frac{1}{2}\frac{\partial^2}{\partial c^2}\Big[\tilde{f}\, D_{cc}\Big] \\ &- \; \frac{1}{2c^2}\frac{\partial}{\partial \theta}\Big[\tilde{f}\, \cot\theta\, D_{\varphi\varphi}\Big] + \frac{1}{2c^2}\frac{\partial^2}{\partial \theta^2}\Big[\tilde{f}\, D_{\theta\theta}\Big]\,,\end{aligned} \tag{42}$$

where $\tilde{f}$ as well as the coefficients F_c, D_{cc}, $D_{\theta\theta}$ and $D_{\varphi\varphi}$ depend on c and θ. A further reduction of the latter equation is obtained if we assume that the friction and diffusion coefficients depend only on the modulus c of the velocity $\mathbf{c}$, then $F_c = F$, $D_{cc} = D_\parallel$ and $D_{\theta\theta} = D_{\varphi\varphi} = D_\perp$ are given by the relations (34)-(36). The resulting form of the FP equation then reads as (see also [41])

$$\partial_t h = -\frac{\partial}{\partial c}\left[h\left(F + \frac{D_\perp}{c}\right)\right] + \frac{1}{2}\frac{\partial^2}{\partial c^2}\Big[h\, D_\parallel\Big] + \frac{D_\perp}{2c^2}\frac{\partial}{\partial a}\left[(1-a^2)\,\frac{\partial h}{\partial a}\right]\,, \tag{43}$$

where $h = c^2\, f(c,\theta)$ and a is given by $a = \cos\theta$. Finally, in the case of an isotropic distribution function, where h is independent of the polar angle θ we get the result

$$\partial_t h = -\frac{\partial}{\partial c}\left[h\left(F + \frac{D_\perp}{c}\right)\right] + \frac{1}{2}\frac{\partial^2}{\partial c^2}\Big[h\, D_\parallel\Big]\,, \tag{44}$$

which will be considered below in the context of code assessment.

In practice, if the field particles are isotropic distributed the problem reduces from three to one variable a fact that makes it more easily tractable and several ways of evaluate the integrals can be adopted. This can be even avoided if the two colliding particles have some properties, as explained in the next section.

3.6. **Inter-Species Collision: The Electron-Ion Case.** Because the ions (index X) are so massive relative to the electrons (index e), the velocity of the electrons is much larger than the one of the ions ($|\mathbf{c}| \gg |\mathbf{w}|$) and, furthermore, the smallness of their mass ratio ($\frac{m_e}{m_X} \ll 1$) is taken into account. Of course, it is possible to formulate the previous statements in several ways, according to the situation on hand. The most intuitive (and maybe crudest) procedure is to approximate $m_X \to \infty$ and and $w_X \to 0$ which means that the electrons are scattered off

by infinitely massive ions, where the energy coupling is null. In this situation the Rosenbluth potentials (23) and (24) can be simply expressed by

$$\mathcal{H}^{(\mathrm{X})}(\mathbf{x},\mathbf{c},t) = \frac{1}{c} \tag{45}$$

$$\mathcal{G}^{(\mathrm{X})}(\mathbf{x},\mathbf{c},t) = c\,, \tag{46}$$

where it is assumed that $f_{\mathrm{X}}(\mathbf{x},\mathbf{w},t)$ is normalised in velocity space. It is straightforward to obtain the components of the friction force and the diffusion tensor for the electrons, which, respectively, read as

$$F_p^{(\mathrm{e})}(\mathbf{x},\mathbf{c},t) = \Gamma_P^{(\mathrm{eX})}\, n_{\mathrm{X}}(\mathbf{x},t)\, \frac{\hat{c}_p}{c^2} \tag{47}$$

and

$$D_{pq}^{(\mathrm{e})}(\mathbf{x},\mathbf{c},t) = \Gamma_P^{(\mathrm{eX})}\, n_{\mathrm{X}}(\mathbf{x},t)\, \frac{1}{c}\left[\delta_{pq} - \hat{c}_p\hat{c}_q\right]\,, \tag{48}$$

where $\hat{c}_p$ is the abbreviation for c_p/c and the ion charge $q_{\mathrm{X}} = Z\,e$. The parameter Λ for this process is proportional to

$$\Lambda \sim \lambda_D = \sqrt{\frac{\epsilon_0\, k_{\mathrm{B}}\, T_{\mathrm{e}}\, T_{\mathrm{X}}}{e^2\,(n_{\mathrm{e}}\, T_{\mathrm{X}} + n_{\mathrm{X}}\, Z^2\, T_{\mathrm{e}})}}\,, \tag{49}$$

and k_{B} is the Boltzmann constant. This collision operator allows no momentum to be transferred from the electrons to the ions and there is no energy exchange.

A more detailed formulation of the problem starts off with considerations about the relative motion of the two species: if the ions mass is much bigger than the electrons' it is reasonable to think that the former did not change their velocity significantly. Indeed ions have a velocity $\mathbf{w}_X \neq 0$ but still $|\mathbf{w}_X| \ll |\mathbf{c}|$ which allows an expansion in Taylor serie of $|\mathbf{g}|$ and $|\mathbf{g}^{-1}|$ in (23) and (24) respectively; a truncation at the second term gives the following expressions for the friction and diffusion coefficient:

$$\frac{\partial \mathcal{H}^{(X)}}{\partial c_p} \approx \frac{c_p}{c^3} + \left(\frac{V_p^{(X)}}{c^3} - 3\,\mathbf{c}\cdot\mathbf{V}^{(X)}\frac{c_p}{c^5}\right) + \frac{9}{4}\frac{c_p}{c^5}\;\overline{v}_h^2 \tag{50}$$

$$\begin{aligned}\frac{\partial^2 \mathcal{G}^{(X)}}{\partial c_p \partial c_q} &\approx \frac{1}{c^3}[c^2\delta_{pq} - c_p c_q] \\ &+ \frac{1}{c^3}[c_p V_q^{(X)} + c_q V_p^{(X)} + \mathbf{c}\cdot\mathbf{V}^{(X)}\delta_{pq}] - 3\,\mathbf{c}\cdot\mathbf{V}^{(X)}\frac{c_p c_q}{c^5} \\ &- \frac{3}{4}\frac{\overline{v}^2}{c^3}\cdot[\delta_{pq} - 3\frac{c_p c_q}{c^2}]\end{aligned} \tag{51}$$

where $\mathbf{V}^{(X)} = \int\limits_{\mathbb{R}^3} d^3w\,\mathbf{w}\,f_h(\mathbf{w}))$ and $\overline{v}^2 = 2v_{th}^2 = 2k_B\frac{T_X}{m_X}$. It is immediate to recognise in the first terms on the rhs the approximation used at the beginning of this section and corresponding to the zero order of the Taylor expansion. The further, higher order terms take into account ions velocity through the moments of their distribution function, that is the force experienced by the electron in a collision with an ion depends on its own velocity and

on the moments of the ion distribution function. Because of the remarkable difference in the velocity it is sufficient in fact to consider only the averaged contributions of the background species and not that of a single particle, and the Taylor expansion allows to separate the two effects. Note that, in the situation where the test particles and scatterers are identical the friction and diffusion are a result of a complex interplay among the particles of the complete ensemble which, in addition, depends on the velocity $\mathbf{c}$.
This and the previous example introduced the primary importance of the evaluation of the force coefficients and supplied some simplified expressions, provided that some hypothesis are respected. Once $\mathcal{H}^{(X)}$ and $\mathcal{G}^{(X)}$, and consequently their derivatives are known they can be inserted in equation (22) and this can in turn be solved, usually numerically. Therefore it is extremely important to have an efficient and effective method available for the computation of these two quantities in the general case.

3.7. **Computation of the Rosenbluth Potentials.** The cornerstones of the general FP problem are the Rosenbluth potentials, so it is important to calculate them rapidly and accurately. For this reasons some properties that allow to recast the Rosenbluth potentials into an appropriate form which will reveal fruitful for numerical computations. A closer inspection of relations (23) and (24) displays that the Rosenbluth potentials are convolutions of the field particle distribution function and the absolute value of the relative speed. This suggest to apply Fourier transformation techniques to compute the integrals, where no assumptions concerning the distribution function have to be imposed. In the following, we consider intra-species scattering which means, that the test and field particles belong to the same type (for instance, electron-electron collision) and drop for convenience the species indices "α" and "β". Performing a change of variables according to $\mathbf{g} = \mathbf{c} - \mathbf{w}$ with $d^3w = -d^3g$ and applying some standard manipulations [45], we obtain the results

$$\hat{\mathcal{H}}(\mathbf{k}) = 8\,\pi \frac{\hat{f}(\mathbf{k})}{k^2} \tag{52}$$

and

$$\hat{\mathcal{G}}(\mathbf{k}) = -8\,\pi \frac{\hat{f}(\mathbf{k})}{k^4}\ , \tag{53}$$

for the transformed quantities with $k = |\mathbf{k}|$, where the identity $\nabla_c^2 g = 2/g$ (see App. E) has been used to obtain the second relation. Clearly, the expressions (23) and (24) reveal once again the convolution character of the Rosenbluth potentials: In $\mathbf{k}$-space this leads to the product of the Fourier transform $\hat{f}(\mathbf{k}) = (2\pi)^{-3/2} \int_{-\infty}^{\infty} d^3c\, \mathrm{e}^{-i\,\mathbf{k}\cdot\mathbf{c}}\, f(\mathbf{c})$ and $1/k^2$, which is the analytically obtained Fourier transformation of the "Coulomb potential" $1/g$ (see App. F). Since only the derivatives of the Rosenbluth potentials enter in the determination of the friction and diffusion coefficients, we apply the differentiation property of the Fourier transformation and get directly

$$\frac{\partial \mathcal{H}}{\partial c_p} = 8\,\pi\, i\ \mathcal{F}^{-1}\left\{ \frac{k_p}{k^2} \hat{f}(\mathbf{k}) \right\} \tag{54}$$

and

$$\frac{\partial^2 \mathcal{G}}{\partial c_p \partial c_q} = 8\,\pi\,\mathcal{F}^{-1}\left\{\frac{k_p\,k_q}{k^4}\hat{f}(\mathbf{k})\right\} \tag{55}$$

for the derivatives of the potentials, where $\mathcal{F}^{-1}$ denotes the inverse Fourier transformation of the arguments in the braces. Moreover, this proceeding considerable reduces "computational noise" often associated with differentiation on the velocity grid. In essence, the main advantage of the Fourier approach is that we obtain a first principle, fully self-consistent determination of the deterministic friction (27) and stochastic diffusion (28) since no specific model assumptions on the field particle distribution are necessary to compute the Rosenbluth potentials.

An analysis of the resolution obtained with Fourier transformation technique is hard to perform due to the three dimensional nature of each component of the friction vector and the diffusion matrix. Choosing a Gaussian initial distribution function, the exact expression for the friction and diffusion forces can be derived and a visual comparison between the numerical value and the analytical expression can be achieved if each component is plotted separately and one of the variables is set as independent. As for instance, in Fig. 3.3, Fig. 3.4 and Fig. 3.5 the level lines of the z-component of the friction force are plotted in the $c_x - c_y$ plane, for $c_z = 0$ and for 32, 64 and 128 grid points respectively. The 128 points calculation gives obviously the most accurate results but the 64 points is an optimal compromise between quality and CPU time. Moreover, from a three dimensional representation is also possible to extract some slices in given planes and the one dimensional curves can be used for an even easier and more direct comparisons. An example is shown in Figs. from 3.7 to 3.9 for $\partial^2\mathcal{G}/\partial c_x^2$ where "portions" were cut out in the planes $c_x = 0$. As expected the 128 points resolution represents the exact profile at the best. Finally, the L_2 norm of the error, evaluated as

$$\epsilon_2 = \frac{\parallel u_{num} \;-\; u_{exact} \parallel_{L_2}}{\parallel u_{exact} \parallel_{L_2}} \tag{56}$$

has been chosen as better measurement of the goodness of the numerical solution on the whole computational domain and has been reported for each case-study in the caption of all pictures; u indicates the general quantity whose error is to be evaluated.

One of the major obstacle to the solution of the Fokker-Planck equation has been now overcome and it is now the time to find the most appropriate method of solving it, which will be the topic of the next chapter.

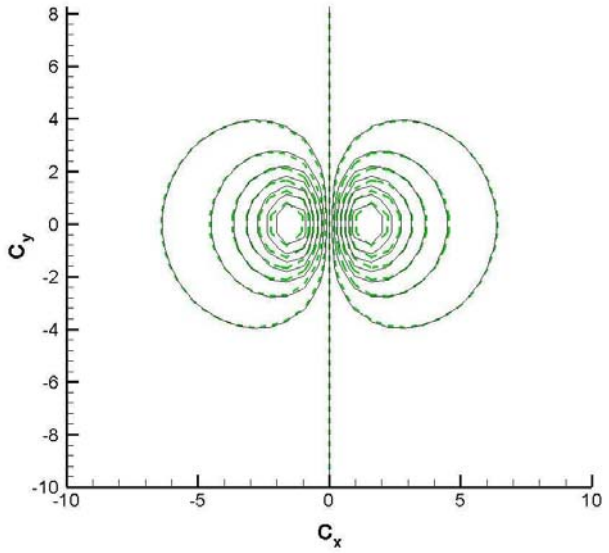

FIGURE 3.3. 32 grid points evaluation of the F_z component. A relevant mismatch from the exact solution (continuous line) is present close to the origin. $\epsilon_2 = 0.45\%$

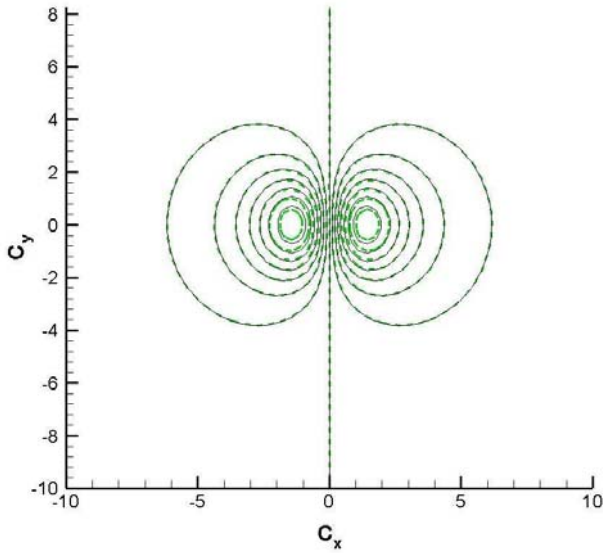

FIGURE 3.4. 64 Points grid points evaluation of the F_z component. The numerical solution is now acceptable. $\epsilon_2 = 0.23$ %

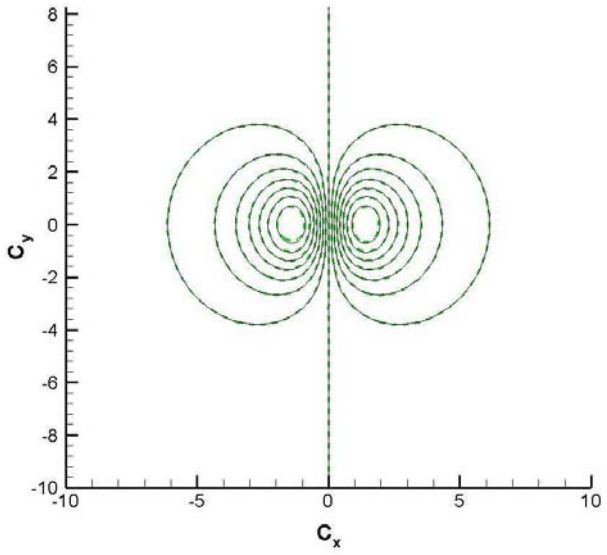

FIGURE 3.5. 128 Points grid points evaluation of the F_z component. Only very small differences from the exact solution. $\epsilon_2 = 0.12$ %

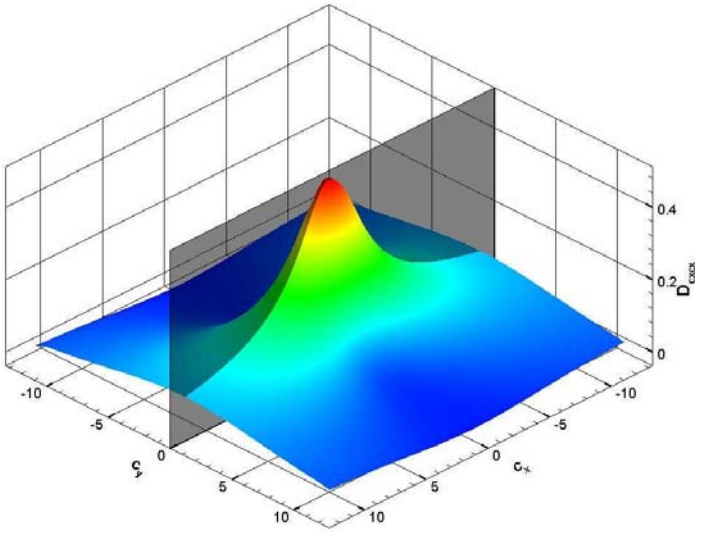

FIGURE 3.6. 3D visualisation of $D_{c_x c_x}(c_x, c_y, 0)$

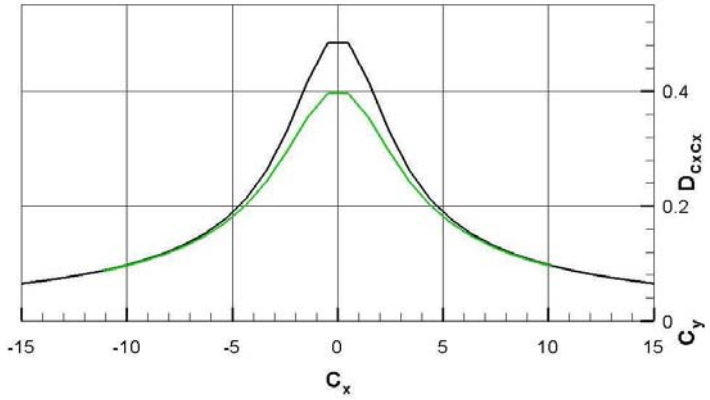

FIGURE 3.7. Exact (bold) and numerical (light) curves extracted from 32 points resolution. The discrepancy is not tolerable for numerical calculations since $\epsilon_2 = 0.44\%$

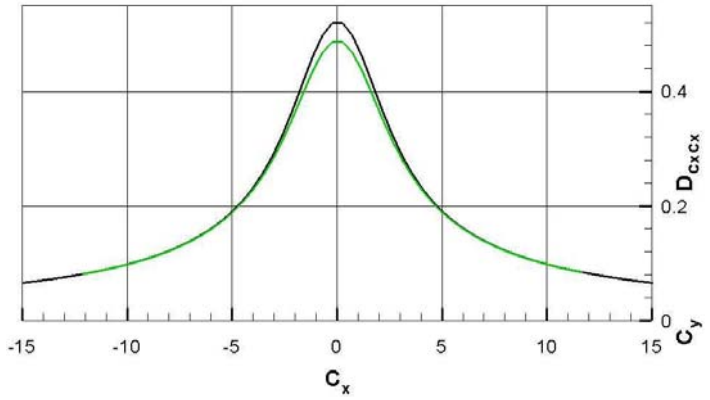

FIGURE 3.8. The 64 points curve is in good agreement and the distance from the exact solution is considered negligible, as indicated also by $\epsilon_2 = 0.24\ \%$

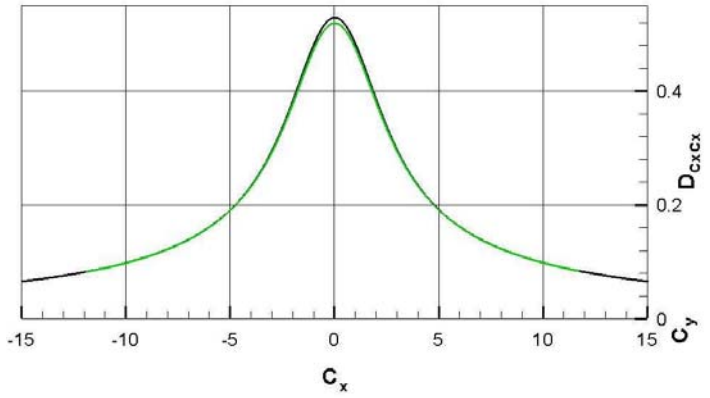

FIGURE 3.9. The 128 Fourier transformation guarantees an extremely good resolution, even though somewhat expensive from the computational point of view ($\epsilon_2 = 0.15$ %)

4. Stochastic Processes and the Fokker-Planck Equation

4.1. **Introduction.** The friction and diffusion forces acting on each scattered particle must be evaluated before solving the Fokker-Planck equation for the time-dependant distribution function. In the last chapter, situations have been explored in which the computation of these two quantities was made easier by means of simplifying hypotheses and finally one general technique was introduced, namely Fourier transform. In most of the cases, $f_\alpha(\mathbf{x}, \mathbf{c}, t)$ must be evaluated per numerical way.
Particle methods solve for the phase-space position of the particles and then eventually reconstruct the distribution function; they can be deterministic or stochastic according to the way of approximating the diffusion process. The time differentiation can be tackled via a Crank-Nicholson method or via an Alternating-direction-implicit method [46, 38].
For the reasons exposed in Sec. 1, a particle method fits very well to the purposes of this work; in particular the stochastic modelling of the diffusion component is suitable to be incorporated in the PIC strategy, giving rise to a fully kinetic, self-consistent approach for the solution of the Fokker-Planck equation.

4.2. **Stochastic Processes.** The information about the kind of plasma in the space thruster, the experience acquainted in PIC technique as well as the PIC-based tool present at IHM and the will of creating a coherent numerical framework for the simulation of this and similar devices, led the choices so far, to approach the diffusion process in a stochastic manner. A short introduction to stochastical processes is therefore needed to show how Coulomb collisions can be easily modelled at expense of some cumbersome algebra. A deep analysis of stochastic calculus is clearly beyond the scope of this work, but it is important to be able to handle this instrument since it opens new roads to the insight of many phenomena.
Generally, a stochastic process is a series of events whose evolution depends on an unpredictably changeable quantity. This means that uncertainty is an intrinsic part of the development of the physical or also for example social or economical systems. In this sense stochastic is present in everyday life, physical phenomena influenced by stochastical processes like chemical reactions or non-Newton fluid flows are, in fact, quite frequent in nature (see, for instance [38, 39]). Nevertheless, the first scientific investigation of a stochastic phenomenon is quite recent and is attributed to the botanist Robert Brown who observed irregular motion of pollen grains suspended in water. Since he could prove that there was no organic explanation in that irregular movement, the solution of the riddle came only in 1905 independently from Einstein and Smoluchowski [47, 48]). Some time afterwards, Langevin developed a different method and according to him *"infinitely more simple"*. In order to study the problem of Brownian motion, Langevin considered the equation

$$\dot{v}(t) = -\gamma\, v(t) + \mathcal{K}(t)\ , \tag{57}$$

for a particle moving in a suspension with a friction coefficient γ, where $\mathcal{K}(t)$ is a highly irregular force acting on the particle with mass m. From this equation he deduced Einstein's result for the variance of the displacement of the particle $\mathsf{Var}\big\{x(t)\big\} = \frac{2\,k_{\mathrm{B}}\,T}{m\,\gamma}\,t$, where he argued

that the average (expectation value) of $< x(t)\,\mathcal{K}(t) >$ vanishes because of the irregularity of $\mathcal{K}(t)$ (see, [38] and the references given therein). This may be regarded that $\mathcal{K}(t)$ represents a time-dependent "random force", which is a model for the highly fluctuating influence of a very rapid sub-system whose action cancels out in the limit when a large number of particle trajectories are considered. Actually a grounding mathematical formulation had to wait 40 years yet when Itô formulated a new concept of calculus, but Langevin equation still remains the first example of stochastic differential equation (SDE), in the sense that it contains a random term whose solution is a random function. The "old" idea that if all initial data can be collected then the future can be predicted must be abandoned and face the fact that most of human everyday's experience (chaos and not quantum mechanics) are unpredictable, in the sense that a very small change in the initial condition can change completely the solution of the problem. It is the task of this new branch of science to evaluate ensemble quantities which can give informations about the degree of uncertainty. To find out how what the Langevin equation has to do with the problem of charged particles collision it is necessary to sketch some basic probability concepts and which will bring to the fundamental equation for the development of the numeric scheme.

4.2.1. *Markov Process*. From now on, the logic path is the one followed in ([38]) where the reader is referred for a major details. Only the guidelines will be given while the formal mathematical steps can be found, for instance, in Ref. [39] and [46].
The probability that the same event occurs at different times, or equivalently if two events occur at the same time is called *joint probability* and the probability that an event occur provided that another occurred is called *conditional probability*. Given a vector $\mathbf{s}$ and $\mathbf{X}$ a vector of random variables the characteristic, or moment generating function is defined by

$$\varphi(\mathbf{s}) = \langle exp(i\ \mathbf{s}\cdot\mathbf{X})\rangle = \int d\mathbf{x}\, p(\mathbf{x}) exp(i\ \mathbf{s}\cdot\mathbf{x}) \tag{58}$$

whose properties will be used and cleared from time to time in the course of this chapter. If a time dependent random variable $\mathbf{X}(t)$ exists it is possible to measure values $\mathbf{x}_1, \mathbf{x}_2, \mathbf{x}_3...$ at times $t_1, t_2, t_3...$ it is assumed that a set of joint probability density exists $p(\mathbf{x}_1, t_1; \mathbf{x}_2, t_2; \mathbf{x}_3, t_3...)$. A weakly correlated stochastical process is called a Markov process if the conditional probability density is given by the condition

$$P_n(x_n, t_n | x_{n-1}, t_{n-1};\ \ldots;\ x_1, t_1) = P_2(x_n, t_n | x_{n-1}, t_{n-1})$$

for $t_1 < t_2 < \cdots < t_n$. This means, that the transition probability to $(x_n,\ t_n)$ depends not on the complete history $(x_{n-1},\ t_{n-1};\ldots;x_1,\ t_1)$ but only on the last state $(x_{n-1},\ t_{n-1})$. Then, $P_2(x_n,\ t_n|\, x_{n-1}\, t_{n-1})\, dx_n$ is the probability that, for instance, a particle travels the distance $x_n - x_{n-1}$ during the time $t_n - t_{n-1}$. A well-know example of a Markov process is the decay of unstable nuclei. A central property of a Markov process is that it is completely defined if the probability density $P_1(x_1,\ t_1)$ and the common probability $P_2(x_2,\ t_2|\, x_1,\ t_1)$ – which is also called conditional or transition probability – is given, that is, the prediction of the future value of $\mathbf{X}(t)$ given the knowledge of the past. From the definition of joint and conditional

probability, and making use of the Markov assumption it follows

$$p(\mathbf{x}_1, t_1|\mathbf{x}_3, t_3) = \int d\mathbf{x}_2\, p(\mathbf{x}_1, t_1|\mathbf{x}_2, t_2)p(\mathbf{x}_2, t_2|\mathbf{x}_3, t_3) \tag{59}$$

the Chapman-Kolmogrov equation which is a nonlinear functional equation relating all conditional probability to each other. Under the hypothesis of:

$$\lim_{\Delta t\to 0} p(\mathbf{x}, t+\Delta t|\mathbf{z}, \mathbf{t})/\Delta t = W(\mathbf{x}|\mathbf{z}, t) \tag{60}$$

$$\lim_{\Delta t\to 0} \tfrac{1}{\Delta t} \int\limits_{|x-z|<\varepsilon} d\mathbf{x}(x_i - z_i)p(\mathbf{x}, t+\Delta t|\mathbf{z}, \mathbf{t}) = A_i(\mathbf{z}, t) + \mathcal{O}(\varepsilon) \tag{61}$$

$$\begin{aligned}\lim_{\Delta t\to 0} \tfrac{1}{\Delta t} \int\limits_{|x-z|<\varepsilon} & d\mathbf{x}(x_i - z_i)\,(x_j - z_j)p(\mathbf{x}, t+\Delta t|\mathbf{z}, \mathbf{t}) \\ & = B_{ij}(\mathbf{z}, t) + \mathcal{O}(\varepsilon)\end{aligned} \tag{62}$$

(the first uniformly in $\mathbf{x}, \mathbf{z}$ and t for $|\mathbf{x} - \mathbf{z}| \geqslant \varepsilon$, the last two being uniform $\mathbf{z}$, ε and t) this equation can be put in differential, more usefull form

$$\begin{aligned}\partial_t p(\mathbf{z}, t|\mathbf{y}, t') = \; & - \sum_i \frac{\partial}{\partial z_i}\Big[A_i(\mathbf{z}, t)p(\mathbf{z}, t|\mathbf{y}, t')\Big] \\ & + \sum_{i,j} \frac{1}{2}\frac{\partial^2}{\partial z_i \partial z_j}\Big[\mathbb{B}_{ij}(\mathbf{z}, t)p(\mathbf{z}, t|\mathbf{y}, t')\Big] \\ & + \int d\mathbf{x}\Big[W(\mathbf{z}|\mathbf{x}, t)p(\mathbf{x}, t|\mathbf{y}, t') \\ & - W(\mathbf{x}|\mathbf{z}, t)p(\mathbf{z}, t|\mathbf{y}, t')\Big].\end{aligned} \tag{63}$$

Under certain conditions, specifying $\mathbf{A}$ and $\mathbb{B}$ as positive semi-definite, and $\mathbf{W}$ as non-negative, a non negative solution of both this and the Chapman-Kolmogrov equation exists. The initial conditions are

$$p(\mathbf{z}, t|\mathbf{y}, t) = \delta(\mathbf{y} - \mathbf{z}); \tag{64}$$

the boundary conditions are generally more difficult to itemise.

4.2.2. *The Fokker-Planck equation.* The first important result is attained: if $\mathbf{W}$ is set to zero equation (63) coincides with the Fokker-Planck equation:

$$\begin{aligned}\partial_t p(\mathbf{z}, t|\mathbf{y}, t') = \; & - \sum_i \frac{\partial}{\partial z_i}\Big[A_i(\mathbf{z}, t)p(\mathbf{z}, t|\mathbf{y}, t')\Big] \\ & + \sum_{i,j} \frac{1}{2}\frac{\partial^2}{\partial z_i \partial z_j}\Big[\mathbb{B}_{ij}(\mathbf{z}, t)p(\mathbf{z}, t|\mathbf{y}, t')\Big]\,,\end{aligned} \tag{65}$$

which define the temporal evolution for the transition probability $p(\mathbf{z}, t|\mathbf{y}, t')$ for a Markov process. The condition $\mathbf{W} = 0$ means that there are no jumps in the solution. It is important to note that if a random variable has a continuous range of possible values, it is a totally different question whether it varies continuously with t, that is if the sample path of $\mathbf{X}(t)$ is continuous. A Markov process can be mathematically continuous but this is not always a good approximation of the reality, for instance systems with a short memory on time scale if the observation is performed. The case of hard sphere-collision model in gas offers a good example: the velocity changes are very likely discontinuous but the change of position are reasonably continuous. The stochastic process corresponds in physics to a diffusion process. If only small Δt are considered, eq. (65) can be approximated by (see App. C):

$$\partial_t p(\mathbf{z}, t|\mathbf{y}, t') = -\sum_i A_i \frac{\partial p(\mathbf{z}, t|\mathbf{y}, t')}{\partial z_i} + \sum_{i,j} \frac{1}{2} B_{ij} \frac{\partial^2 p(\mathbf{z}, t|\mathbf{y}, t')}{\partial z_i \partial z_j}, \tag{66}$$

and even solved for p getting:

$$p(\mathbf{z}, t + \Delta t|\mathbf{y}, t) = (2\pi)^{-N/2} \left\{ det\Big[\mathbb{B}(\mathbf{y}, t)\Big] \right\}^{1/2} [\Delta t]^{1/2} \times \tag{67}$$

$$\exp\left\{ -\frac{1}{2} \frac{[\mathbf{z} - \mathbf{y} - \mathbf{A}(\mathbf{y}, t)\Delta t]^T][\mathbb{B}(\mathbf{y}, t)]^{-1}[\mathbf{z} - \mathbf{y} - \mathbf{A}(\mathbf{y}, t)\Delta t]}{\Delta t} \right\},$$

that is a Gaussian distribution with variance matrix $\mathbb{B}$ and mean $\mathbf{y} + \mathbf{A}(\mathbf{y}, t)\Delta t$. It is not difficult now to imagine a system moving with a systematic drift at a rate $\mathbf{A}$ on which is superposed a Gaussian disturbance with covariance matrix $\mathbb{B}\Delta t$ that is:

$$\mathbf{y}(t + \Delta t) = \mathbf{y}(t) + \mathbf{A}(\mathbf{y}(t), t)\ \Delta t + \eta(t)\ \Delta t^{1/2}, \tag{68}$$

where $\langle \eta(t) \rangle = 0$ and $\langle \eta(t)\eta(t)^T \rangle = \mathbb{B}(\mathbf{y}, t)$. Summarising, if a joint probability function describes a Markov process, it may satisfies the differential Chapman-Kolmogrov equation, which turns to be the Fokker-Planck equation under opportune hypothesis. During small time intervals the solution for the probability density function can be found and arguments can be derived even for the time evolution of the system itself. What is for the moment only a speculation will be the key to build a new numerical method to work out the Coulomb collision problem. To do this, another mathematical instrument is needed, namely the Itô calculus whereby the formal equivalence between eq. (65) and (68) will be demonstrated.

4.3. **General Ideas and Basic Relations.** The previous reasoning led to the intuitive conclusion that instead of solving eq. (66) for the variable p, it is possible to solve eq. (68), which looks more attractive because it acts directly on a particle property, namely the

velocity. What now an hint is will be proofed right after. The straightforward extension of the Langevin equation in one dimension reads as:

$$dC(t) = F(C,t)\,dt + B(C,t)\,dW(t)\ , \tag{69}$$

where the coefficients are in general functions of the stochastical variable $C = C(t)$ and time t and $dW(t)$ is the Wiener increment. Note, that in the case where B is a constant the random forcing is called additive noise, otherwise, if B (linearly) depends on the generic stochastic quantity $V(t)$ the forcing is called multiplicative noise. The SDE (69) has to be interpreted mathematically as a stochastic integral equation of the form

$$C(t) = C(t_0) + \int_{t_0}^{t} F\Big(C(s),s\Big)\,dt + \int_{t_0}^{t} B\Big(C(s),s\Big)\,dW(s)\ . \tag{70}$$

Here, the second term on the rhs is an ordinary integral (of Riemann or Lebesgue type), while the third term is a stochastical integral, which has to be interpreted consistently. The Wiener increment $dW(t)$ appearing in equation (69) and (70) may be defined as an integral over the rapidly fluctuating random term $\eta(t)$ (see, for instance [38, 39])

$$dW(t) = \int_{t}^{t+dt} \eta(s)\,ds\ , \tag{71}$$

with the requirements that for $t \neq t'$, $\eta(t)$ and $\eta(t')$ are statistically independent, the mean value $< \eta(t) >= 0$ and and the variance $< \eta(t)\,\eta(t') >= \delta(t-t')$. For our purposes, we introduce the Wiener increment by considering the sequence $\Big\{\eta_i\Big\}_{i\in\mathbb{N}}$ of independently and identically distributed random numbers with the expectation values $\mathcal{E}\{\eta_i\} = 0$ and $\mathcal{E}\{\eta_i^2\} = 1$

$$W^N(t_n) = \frac{1}{\sqrt{N}}\sum_{i=1}^{n}\eta_i\ ; \quad t_n = \frac{n}{N}\ \ , 0 \le n \le N \tag{72}$$

with $\Delta t_i = t_{i+1} - t_i = 1/N$. Then, the Wiener increment reads as

$$\Delta W_i = W_{i+1} - W_i = \frac{1}{\sqrt{N}}\,\eta_{i+1} = \sqrt{\Delta t_i}\,\eta_{i+1}\ , \tag{73}$$

and possess the properties $\mathcal{E}\big\{\Delta W_i\big\} =< \Delta W_i >= 0$ and $\mathcal{E}\big\{\Delta W_i\,\Delta W_j\big\} =< \Delta W_i\,\Delta W_j >= \Delta t_i\,\delta_{ij}$, where the latter relation indicates that the variance is linear in Δt_i. Now, setting in the integral equation (70) $C(t_0) = F = 0$ and replacing B by the random function $G = G\Big(W(t),t\Big)$, we obtain the formal definition of the Itô integral:

$$\mathcal{I}[G] = \int_{t_0}^{t} G\Big(W(s),s\Big)\,dW(s)\ , \tag{74}$$

which now depends also on $W(t)$. For the discretisation $t_0 < t_1 < t_2 < \cdots < t_{n+1} = t$, this integral is usually approximated by the sum

$$\mathcal{I}[G^{(n)}] = \sum_{i=1}^{n} G_i^{(n)}\ \Delta W_i\ , \tag{75}$$

where $G_i^{(n)} = G^{(n)}\Big(W(\tau_i), \tau_i\Big)$ with $\tau_i = t_i$ and the Wiener increment $\Delta W_i = W_{i+1} - W_i$ is given by (73). On should expect that the "random variable" $\mathcal{I}[G^{(n)}]$ has zero mean since it is a sum of random numbers ΔW_i with zero mean. However, to guarantee this, appropriate measurability conditions of the random function $G_i^{(n)}$ must imposed to ensure that $G_i^{(n)}$ and the Wiener increment ΔW_i are "independent",

$$\mathcal{E}\Big\{G_i^{(n)}\,\Delta W_i\Big\} = \mathcal{E}\Big\{G_i^{(n)}\Big\}\,\mathcal{E}\Big\{\Delta W_i\Big\} = 0 \tag{76}$$

which means, the nonanticipativeness of the integrand. The appropriate conditions, the mean-square convergence of the integrals $\mathrm{I}[G^{(n)}]$ to $\mathrm{I}[G]$ and the corresponding proofs are discussed in great detail by Kloeden & Platen [49]. Here, we only cite some important results, for instance, the Itô isometry

$$\mathcal{E}\Big\{\mathrm{I}[G]\Big\} = 0\,, \tag{77}$$

$$\mathcal{E}\Big\{\mathrm{I}^2[G]\Big\} = \int_{t_0}^{t} \mathcal{E}\Big\{G^2\Big(W(s), s\Big)\Big\} ds\,, \tag{78}$$

$$\mathcal{E}\Big\{\mathrm{I}[G]\,\mathrm{I}[H]\Big\} = \int_{t_0}^{t} \mathcal{E}\Big\{G\Big(W(s), s\Big) H\Big(W(s), s\Big)\Big\} ds\,, \tag{79}$$

which may be immediately obtained by starting the computations from the approximate form of the Itô integral (75). A crucial point is the fact that the partial sums (75) depend on the particular choice of the intermediate point τ_i within an interval $[t_i,\, t_{i+1}]$ where the integrand $G\Big(W(\tau_i), \tau_i\Big)$ is evaluated. As mentioned above, for the choice $\tau_i = t_i$ the expression (75) define the Itô stochastic integral of the function G. This Itô interpretation and the corresponding calculus is used in this thesis. Another often useful choice of an intermediate point, namely, $\tau_i = (t_i + t_{i+1})/2$ leads to the Stratonovich interpretation, which satisfies the usual transformation rules of classical calculus. Note, that different interpretations lead to different solutions of the SDE which, however, can be related to each other [38, 49].

4.4. **Itô Formula.** By means of the appropriate definitions, the SDE can be integrated and solved. Before reaching the goal, it is still important to know how it is possible to approximate a random function around a point, in words the stochastic equivalent of the Taylor expansion. This will be also the basis for the development of the numerical solution. The reader is referred again to the books of Gardiner and Kloeden & Platen [38, 49] for further details. For this purpose, we consider the stochastical quantity $C(t)$ which obeys the SDE (69), and assume that the function Φ depends on this variable: $\Phi = \Phi(C, t)$. Then, the growth of Φ during the time step dt is given by the expansion

$$\begin{aligned} d\Phi(C,t) &= \Phi(C + dC, t + dt) - \Phi(C,t) \\ &= \dot{\Phi}(C,t)\,dt + \Phi'(C,t)\,dC + \frac{1}{2}\Phi''(C,t)\,dC^2\,, \end{aligned} \tag{80}$$

where the dot and prime indicate the differentiation with respect to t and C, respectively. Since the Wiener increment (73) is proportional to $\sqrt{\Delta t}$, we also have to consider the second order term and get for the growth

$$\begin{aligned} d\Phi(C,t) &= \left[\dot{\Phi} + \Phi' F(C,t) + \frac{1}{2}\Phi'' B^2(C,t)\right] dt \\ &+ \Phi' B(C,t)\, dW(t) \,, \end{aligned} \tag{81}$$

where we have applied that $\Big[dW(t)\Big]^2 = dt$, which is one of the key properties of the Itô calculus. The later relation is called Itô formula or stochastic chain rule and states that changing variables is not obtained by ordinary calculus (exception: Φ is linear in C), because of the appearance of the third term in the square braces of expression (81).

In order to obtain the multi-dimensional version of the Itô formula one has to start from the multi-dimensional generalisation of (69) which is given by

$$d\mathbf{C}(t) = \mathbf{F}(\mathbf{C},t)\, dt + \mathbb{B}(\mathbf{C},t)\, d\mathbf{W}(t) \,, \tag{82}$$

where $\mathbf{C}$, $\mathbf{F} \in \mathbb{R}^{\,\mathrm{d}}$ are d-dimensional vectors, the matrix $\mathbb{B} \in \mathbb{R}^{\,\mathrm{d}\times\mathrm{m}}$ is related to the diffusion tensor according to $\mathbb{D} = \mathbb{B}\,\mathbb{B}^T \in \mathbb{R}^{\,\mathrm{d}\times\mathrm{d}}$, and $\mathbf{W} \in \mathbb{R}^{\,\mathrm{m}}$ represents the m-dimensional Wiener process. Then, one can show that the growth of the function $\Phi = \Phi(\mathbf{C},t)$ has the form

$$d\Phi(\mathbf{C},t) = \mathcal{L}^{(0)}\Phi\; dt + \sum_{q=1}^{m} \mathcal{L}^{(q)}\Phi\; dW^q(t) \tag{83}$$

where

$$\mathcal{L}^{(0)} = \frac{\partial}{\partial t} + \sum_{p=1}^{d} F_p \frac{\partial}{\partial C_p} + \frac{1}{2}\sum_{p,q=1}^{d} D_{pq} \frac{\partial^2}{\partial C_p\, \partial C_q}\; dt \tag{84}$$

and

$$\mathcal{L}^{(q)} = \sum_{p=1}^{d} B_{pq} \frac{\partial}{\partial C_p} \,, \tag{85}$$

are introduced for convenience and D_{pq} and B_{pq} denote the elements of $\mathbb{D}$ and $\mathbb{B}$, respectively. This equation establishes the multi-dimensional form of the Itô formula for multi-dimensional stochastic differentials with multi-dimensional Wiener processes.

4.5. **Equivalence between the FP and SDE Approach.** Finally it is now possible to introduce the most attractive and important property, namely, the link between the FP equation and the SDE; see [38, 49] for further informations and stringent proofs. We consider the stochastic variable $\mathbf{C}(t)$ with the transition probability $P_2(\mathbf{C},t|\mathbf{C}_0,t_0)$, and assume that the arbitrary function $\psi(\mathbf{C})$ is twice continuously differentiable and vanishes at the boundary of the domain Ω. Applying the expectation value operator $\mathcal{E}$ to the Itô formula (83) for ψ, we obtain the expression

$$\begin{aligned} \frac{d}{dt}\mathcal{E}\Big\{\psi(\mathbf{C},t)\Big\} &= \sum_{p} \mathcal{E}\left\{ F_p(\mathbf{C},t)\, \frac{\partial \psi}{\partial C_p} \right\} \\ &+ \frac{1}{2}\sum_{p,q} \mathcal{E}\left\{ D_{pq}(\mathbf{C},t)\, \frac{\partial^2 \psi}{\partial C_p\, \partial C_q} \right\} , \end{aligned} \tag{86}$$

where we already use the fact that the expectation of the last term of the Itô expansion vanishes

$$\mathcal{E}\Big\{ B_{pq}\,\frac{\partial\psi}{\partial C_p}\,dW_q(t)\Big\}=0$$

because of the nonanticipativeness requirement (76) and the result that $\mathcal{E}\big\{dW_q(t)\big\}=0$. Using for the expectation the expression $\mathcal{E}\big\{(...)\big\}=\int\limits_{\Omega} d^3C\,P_2(\mathbf{C},t|\mathbf{C}_0,t_0)\,(...)$, keeping in mind the imposed properties on ψ and performing integration by parts we get the result

$$\int\limits_{\Omega} d^3C\,\psi(\mathbf{C},t)\left\{\frac{\partial\,P_2}{\partial t}+\sum_p\frac{\partial}{\partial C_p}\Big[F_p\,P_2\Big]-\frac{1}{2}\sum_{p,q}\frac{\partial^2}{\partial C_p\partial C_q}\Big[D_{pq}\,P_2\Big]\right\}=0\,. \tag{87}$$

Clearly, because ψ is an arbitrary function, the expression in the curly braces must be zero, yielding the FP equation

$$\frac{\partial\,P_2}{\partial t}=-\sum_p\frac{\partial}{\partial C_p}\Big[F_p\,P_2\Big]+\frac{1}{2}\sum_{p,q}\frac{\partial^2}{\partial C_p\partial C_q}\Big[D_{pq}\,P_2\Big] \tag{88}$$

for the transition probability P_2 of the variable $\mathbf{C}$. Obviously, we recognise the complete equivalence between the SDE (82) and the diffusion process – described by the FP equation (88) – which is defined by the drift coefficients $F_p(\mathbf{C},t)$ and diffusion coefficients $D_{pq}(\mathbf{C},t)$ (cf. equations (27)-(28)). This equivalence will be exploit in the following: instead to solve the FP equation (22) for the distribution function f_α of the particle specie "α", we solve numerically the corresponding SDE (82) for the particles of this ensemble. Due to this close connection, the inter- and intra-species charged particle collisions will be treated by the solution of a Langevin-type SDE and, consequently, fits in a natural way into the PIC method, which is one basic concept of the hybrid PIC/DSMC code development [6]. In the following section we discuss a further consequence of the Itô formula, which is especially important for the construction of discrete approximations of the Langevin-type equation (88)

4.6. **Itô-Taylor Expansion.** In contrast to the Taylor expansion for the function $f:\mathbb{R}\to\mathbb{R}$ of a deterministic variable X, we expect a more complicated series expansion for a stochastic variable C due to the modified chain rule in Itô calculus (see, relations (81) and (83)). The stochastic counterpart of the deterministic Taylor formula for the expansion of a smooth function is, especially, important for the derivation of numerical methods for SDEs. There are several possibilities to introduce a stochastic Taylor series expansion (see, for instance [39, 49]), which is called "Itô-Taylor Expansion" (ITE) in the following. In the context of the present work the ITE is obtained by iterated application of the Itô formula (81) in one dimension or (83) in the multi-dimensional case; more details about this proceeding is found in the books [49, 50]. In order to outline the basic ideas of the ITE (which can be considered as a generalisation of the deterministic Taylor expansion), we begin from the stochastic integral equation:

$$\mathbf{C}(t)=\mathbf{C}(t_0)+\int\limits_{t_0}^{t}F\Big(\mathbf{C}(s),s\Big)\,ds+\sum_{q=1}^{m}\int\limits_{t_0}^{t}dW^q(s)\mathbf{b}_q(\mathbf{C}(s),s)\,. \tag{89}$$

obtained by integration of (82) over $[t_0, t]$. Here, the column vector $\mathbf{b} = \mathbb{B}\ \mathbf{e}_q$ is introduced where $\mathbf{e}_q \in \mathbb{R}^m$ are the usual Cartesian unit vectors in m-dimensional space. Applying the integrated form of the Itô formula (83)

$$\varphi\{\tau\} = \varphi\{t_0\} + \int_{t_0}^{\tau} ds \left[\mathcal{L}^{(0)}\,\varphi\right]\{s\} + \sum_{r=1}^{m} \int_{t_0}^{\tau} dW^r(s) \left[\mathcal{L}^{(r)}\,\varphi\right]\{s\}\,, \tag{90}$$

to the functions $\varphi = F_p$ and $\varphi = B_{pq}$ – the p^{th} row of $\mathbf{F}$ and $\mathbf{b}_q$, respectively – we get after some rearrangements the expression

$$\mathbf{C}(t) = \mathbf{C}(t_0) + \mathbf{F}\{t_0\} \int_{t_0}^{t} ds_2 + \sum_{q=1}^{m} \mathbf{b}_q s_0 \int_{t_0}^{t} dW^q(s_2) + \mathbf{R} \tag{91}$$

with remainder

$$\begin{aligned}
\mathbf{R} &= \int_{t_0}^{t} ds \int_{t_0}^{s} ds_1 \left[\mathcal{L}^{(0)}\mathbf{F}\right]\{s_1\} + \sum_{r=1}^{m} \int_{t_0}^{t} ds \int_{t_0}^{s} dW_{s_1}^r \left[\mathcal{L}^{(r)}\mathbf{F}\right]\{s_1\} \\
&+ \sum_{q=1}^{m} \int_{t_0}^{t} dW_s^q \int_{t_0}^{s} ds_1 \left[\mathcal{L}^{(0)}\mathbf{b}_q\right]\{s_1\} \\
&+ \sum_{q,r=1}^{m} \int_{t_0}^{t} dW_s^q \int_{t_0}^{s} dW_{s_1}^r \left[\mathcal{L}^{(r)}\mathbf{b}_q\right]\{s_1\}
\end{aligned} \tag{92}$$

where $\{t\}$ abbreviates $\{t\} = \Big(\mathbf{C}(t), t\Big)$. To simplify the representation, it is convenient to define the multiple Itô integral of the function f according to [49]

$$\begin{aligned}
\mathcal{I}_{(j_1,j_2,\ldots,j_l)}[f]_{t_0,t} &= \int_{t_0}^{t} \int_{t_0}^{s_l} \ldots \int_{t_0}^{s_2} f(s_1) dW^{j_1}(s_1) \ldots dW^{j_{l-1}}(s_{l-1}) dW^{j_l}(s_l) \\
&= \int_{t_0}^{t} dW^{j_l}(s_l) \int_{t_0}^{s_l} dW^{j_{l-1}}(s_{l-1}) \\
&\ldots \int_{t_0}^{s_2} dW^{j_1}(s_1) f(s_1)
\end{aligned} \tag{93}$$

with the multi-index $\alpha = (j_1, j_2, \ldots, j_l)$, where $j_k \in \{0, 1, .., m\}$ for $k \in \{1, 2, ..., l\}$ and $m = 1, 2, ...$ and the convention that $dW^0(s) = ds$. [1]. With the additional abbreviation $\mathcal{I}_{(j_1,j_2,\ldots(j_l)} = \mathcal{I}_{(j_1,j_2,\ldots,j_l)}[f]_{t_0,t}$ for the Itô integral with constant integrand, the simplest ITE (91) and (92) reads as:

$$\mathbf{C}(t) = \mathbf{C}(t_0) + \mathbf{F}\{t_0\}\mathcal{I}_{(0)} + \sum_{q=1}^{m} \mathbf{b}_q\{t_0\}\mathcal{I}_{(q)} + \mathbf{R} \tag{94}$$

[1] Note, that for f=1 and $j = j_1 = j_2 = \cdots = j_l$ the Itô integral (93) can be expressed according to $\mathcal{I}_{(j,j,\ldots,j);\,t_0,t} = \frac{1}{l!}\Big(\frac{t-t_0}{2}\Big)^{l/2} \mathrm{H}_l\Big(\frac{\mathcal{I}_{(j,j,\ldots,j);\,t_0,t}}{\sqrt{2(t-t_0)}}\Big)$, where $\mathrm{H}_l(z) = (-1)^l \mathrm{e}^{z^2} \frac{d^l}{dz^l} \mathrm{e}^{-z^2}$ are the Hermite polynomials.

with

$$\mathbf{R} = \mathcal{I}_{(0,0)}\Big[\mathcal{L}^{(0)}\mathbf{F}\Big]_{t_0,t} \quad + \quad \mathcal{I}_{(0,r)}\Big[\mathcal{L}^{(r)}\mathbf{F}\Big]_{t_0,t} + \sum_{q=1}^{m}\mathcal{I}_{(0,q)}\Big[\mathcal{L}^{(0)}\mathbf{b}_q\Big]_{t_0,t}$$
$$+ \quad \sum_{q,r=1}^{m}\mathcal{I}_{(r,q)}\Big[\mathcal{L}^{(r)}\mathbf{b}_q\Big]_{t_0,t}. \tag{95}$$

It is obvious from this expression that multiple stochastic integrals are central objects for the representation of an approximate solution of the SDE (82). Clearly, the obtained expansion procedure can be continued by repeated applications of formula (90) (see next chapter). For instance, we obtain for $\varphi = \mathcal{L}^{(r)}B_{pq}$ immediately

$$\mathcal{I}_{(r,q)}\Big[\mathcal{L}^{(r)}\mathbf{b}_q\Big]_{t_0,t} \quad = \quad \Big[\mathcal{L}^{(r)}\mathbf{b}_q\Big]_{t_0}\mathcal{I}_{(r,q)} + \mathcal{I}_{(0,r,q)}\Big[\mathcal{L}^{(0)}\mathcal{L}^{(r)}\mathbf{b}_q\Big]_{t_0,t}$$
$$+ \quad \sum_{s=1}^{m}\mathcal{I}_{(s,r,q)}\Big[\mathcal{L}^{(s)}\mathcal{L}^{(r)}\mathbf{b}_q\Big]_{t_0,t}. \tag{96}$$

For sake of completeness, we notice that the so-called Itô (vector) coefficient functions $\mathbf{k}_{(0)} = \mathbf{F}\{t_0\}, \mathbf{k}_{(q)} = \mathbf{b}_q\{t_0\}, \mathbf{k}_{(r,q)} = \Big[\mathcal{L}^{(r)}\mathbf{b}_q\Big]\{t_0\}$ etc. at $\{t_0\}$ can be evaluated recursively. That means, for multi-index length $l(\alpha) \geq 1$, $l(\alpha) \in \{1,2\}$, we obtain

$$\mathbf{k}_\alpha = \Big[\mathcal{L}^{(m)}\mathbf{k}_{-\alpha}\Big]\{t_0\}, \quad n \in \{0,q\}, \tag{97}$$

where $-\alpha = (j_1, j_2, j_3, ..., j_l) = (j_2, j_3, ..., j_l)$. In essence, we retain from this section that a (sufficient) smooth function of an Itô process can be expanded in an Itô-Taylor series which is a sum of finite multiple Itô integrals with constant integrands and a remainder which is established by a finite number of Itô integrals with non-constant integrands (cf., expression (94)). Moreover, appropriate hierarchical sets (see App. G) are the basis of the ITE with which a characterisation is possible. In the next chapter the ITE is used to construct suitable discrete schemes for the solution of the SDE (82).

5. Numerical Framework

5.1. **Introduction.** In chapter 4 the formal equivalence between the SDE and the FP equation has been shown, which means that in principle it is possible "to choose" which of the two equations to solve. An adoption coherent with the philosophy depicted by Figure 1.2 privileges the former for fitting very well in a Particle-In-Cell scheme, as it will be shown later. It describes essentially the movement of each single (macro)-particle due to friction and diffusion forces corresponding to the distribution function given by (65). The technique to evaluate friction and diffusion forces has been depicted in Chap. 3 while the Wiener process was explicitated in the previous chapter where also a sketch of a possible numerical method was given. It is now time to put the ingredients in the right order to obtain the whole numerical recipe. The nature of the SDE changes the classical phase-space PIC approach and addresses the study field to conceive a scheme working fully in velocity space. For this reason it is seems appropriate here to sketch out the main features of this approach and describe some theoretical aspects which will be the core of this work.

5.2. **A new PIC-based approach for the FP Equation.** The key quantities to solve the Langevin-type differential equation are the velocity dependent friction (27) and diffusion (28) coefficients at each time step $t = t_n$. For this purpose a PIC-type, self-consistent numerical scheme is constructed in the velocity space. Schematically a typical PIC-cycle is depicted in Figure 5.1. The peculiarity of this PIC scheme is the fact that it is built in the velocity space, and then classically divided in two areas, one mesh-free and one grid-based. In the following the different building blocks of the PIC scheme are discussed in detail. For sake of clearness,

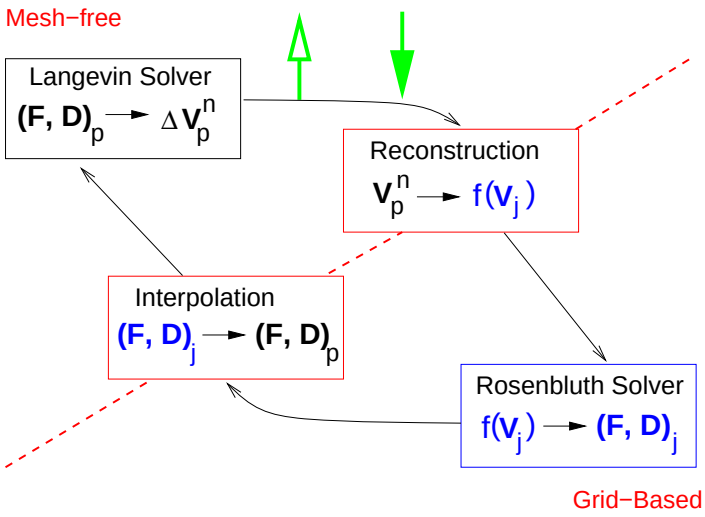

Figure 5.1. Schematical description of the Fokker-Planck solver based on the PIC method in the velocity space.

we consider here a single grid cell of the spatial computational domain, containing a sufficient large number of particles (of a certain specie "α"). Furthermore, if it is skilful and pedagogical

sensible we will introduce the three-dimensional formulation of the numerical schemes, else we switch to lower-dimensional descriptions which could be straightforward generalised.

Associated with each local grid zone is a Cartesian mesh in velocity space with an equidistant spacing Δu, Δv and Δw in $x-$, $y-$, and $z-$direction, respectively, which is built up according to

$$\begin{aligned} u_{i,j,k} &= u_0 + (i-1)\,\Delta u\,, \quad 1 \le i \le I+1 \\ v_{i,j,k} &= v_0 + (j-1)\,\Delta v\,, \quad 1 \le j \le J+1 \\ w_{i,j,k} &= w_0 + (k-1)\,\Delta w\,, \quad 1 \le k \le K+1\,. \end{aligned} \tag{98}$$

Here, u, v, and w are the components of the velocity grid vector $\mathbf{v}_{i,j,k} = \Big(u,\, v,\, w\Big)^T_{i,j,k}$ and $\Big(u_0,\, v_0,\, w_0\Big)^T$ are the coordinates of the starting point of the velocity grid.

Reconstruction Block (Localisation and Assignment). From the actual location of the plasma particles in mesh-free velocity space, the distribution function $f(\mathbf{c})$ is constructed on the Cartesian velocity mesh in two steps. At first the particles have to be located with respect

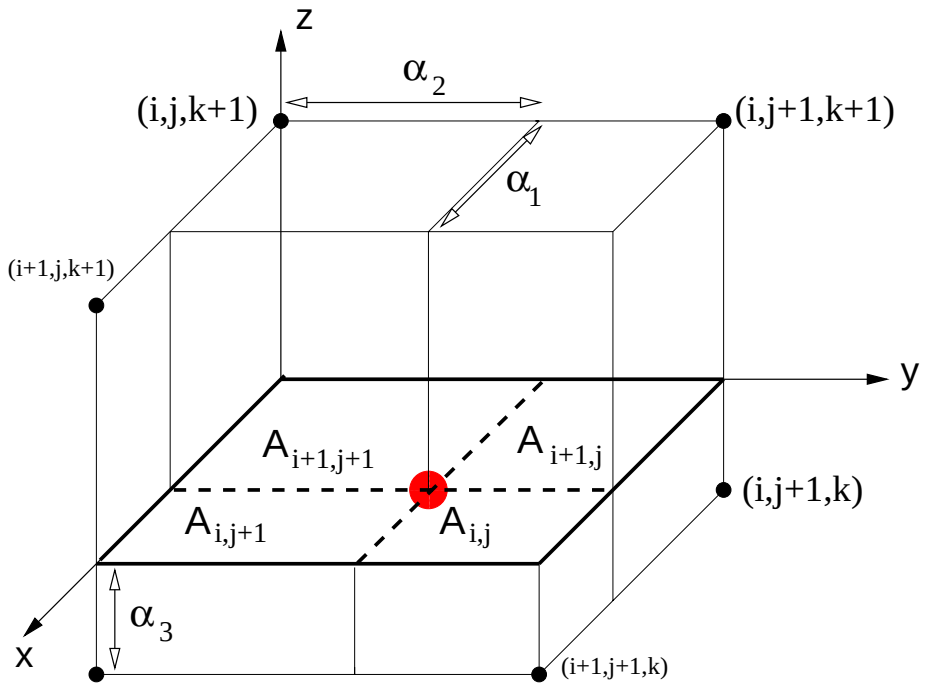

FIGURE 5.2. Assignment of the particle's velocity to the nodes (grid-based model) and interpolation of the results obtained in the nodes onto the particle's position in velocity space (mesh-free model) with the aid of the volume-weighting approach.

to the velocity grid. To identify the address of the cell $Z_{i,j,k}$ where the particle's velocity is

found, we apply the localisation strategy

$$\begin{aligned} i_p &= \mathrm{INT}\Big(\frac{[V_1]_n^p - u_0}{\Delta u}\Big) + 1 \\ j_p &= \mathrm{INT}\Big(\frac{[V_2]_n^p - u_0}{\Delta u}\Big) + 1 \\ k_p &= \mathrm{INT}\Big(\frac{[V_3]_n^p - u_0}{\Delta u}\Big) + 1 \,, \end{aligned} \tag{99}$$

where $\mathbf{V}_n^p = \Big([V_1]_n^p,\, [V_2]_n^p,\, [V_3]_n^p\Big)^T$ is the velocity vector of the p$^{\mathrm{th}}$ particle at time t_n and INT(.) denotes the integer part of a real number. Note, that the strength – namely, the high efficiency – of this approach is a consequence of the equidistant grid spacing. Secondly, after the particle is localised in the grid cell Z_{i_p,j_p,k_p} of the velocity mesh, we have to bridge the gap between the mesh-free and grid-based computations. For this purpose, we introduce the relative weighting coordinates $\alpha^{(p)} = \Big(\alpha_1^{(p)},\, \alpha_2^{(p)},\, \alpha_3^{(p)},\, \Big)$ of the p$^{\mathrm{th}}$ particle at $t = t_n$ according to

$$\begin{aligned} \alpha_1^{(p)} &= \frac{1}{\Delta u}\Big([V_1]_n^p - u_{i_p,j_p,k_p}\Big) \\ \alpha_2^{(p)} &= \frac{1}{\Delta v}\Big([V_2]_n^p - v_{i_p,j_p,k_p}\Big) \\ \alpha_3^{(p)} &= \frac{1}{\Delta w}\Big([V_3]_n^p - w_{i_p,j_p,k_p}\Big) \,. \end{aligned} \tag{100}$$

It is obvious, that the weights $g_{i,j,k}^{(p)}$ of the considered particle have to be calculated with respect to the surrounding eight nodes of the grid (see Figure 5.2). The first step to do this, is to compute the four areas of the section parallel to the $(x,\, y)$-plane, where the particle is located. According to the area-weighting method [51, 14] we get

$$\begin{aligned} A_{i,j} &= \Big(1 - \alpha_1^{(p)}\Big)\Big(1 - \alpha_2^{(p)}\Big) \\ A_{i+1,j} &= \alpha_1^{(p)}\Big(1 - \alpha_2^{(p)}\Big) \\ A_{i,j+1} &= \Big(1 - \alpha_1^{(p)}\Big)\alpha_2^{(p)} \\ A_{i+1,j+1} &= \alpha_1^{(p)}\,\alpha_2^{(p)} \,. \end{aligned} \tag{101}$$

These areas form the bases of eight cuboids

$$\begin{aligned} \begin{matrix} g_{i,j,k}^{(p)} \\ g_{i,j,k+1}^{(p)} \end{matrix} &= A_{i,j} \begin{cases} 1 - \alpha_3^{(p)} \\ \alpha_3^{(p)} \end{cases} \\ \begin{matrix} g_{i+1,j,k}^{(p)} \\ g_{i+1,j,k+1}^{(p)} \end{matrix} &= A_{i+1,j} \begin{cases} 1 - \alpha_3^{(p)} \\ \alpha_3^{(p)} \end{cases} \\ \begin{matrix} g_{i,j+1,k}^{(p)} \\ g_{i,j+1,k+1}^{(p)} \end{matrix} &= A_{i,j+1} \begin{cases} 1 - \alpha_3^{(p)} \\ \alpha_3^{(p)} \end{cases} \\ \begin{matrix} g_{i+1,j+1,k}^{(p)} \\ g_{i+1,j+1,k+1}^{(p)} \end{matrix} &= A_{i+1,j+1} \begin{cases} 1 - \alpha_3^{(p)} \\ \alpha_3^{(p)} \end{cases} \,. \end{aligned} \tag{102}$$

which represent the relative coordinates $\alpha^{(p)}$ depending weights of the p$^{\text{th}}$ particle located in the grid cell Z_{i_p,j_p,k_p}. As one would expect, the weights fulfil the relation

$$\sum_{\mu,\nu\lambda=0}^{1} g^{(p)}_{i+\mu,j+\nu,k+\lambda} = 1 \; , \tag{103}$$

and, obviously can be interpreted as fraction of the volume of the actual grid cell. Furthermore, the applied method may be considered as an extension of the well-known area-weighting method to three dimensions and, hence will be called volume-weighting technique.

Rosenbluth Solver. The reconstructed field particle (scatterer) distribution function on the velocity grid is used for the computation of the Rosenbluth potentials and their derivatives, from which the friction and diffusion coefficients for the test particles are determined. In order to be free of any model assumption – like isotropic distribution of the field particles –, we apply Discrete Fourier Transformation (DFT) techniques [52, 53, 54]. As it is discussed in detail by Brigham [52], the DFT represents a special case of the (continuous) Fourier integral transformation, to which three "modifications" are necessary. The DFT in one dimension may be defined according to

$$f_\tau = \frac{1}{N} \sum_{\sigma=0}^{N-1} \hat{f}_\sigma \, \mathrm{e}^{2\pi i \frac{\tau\sigma}{N}} \; ; \quad \tau = 0, 1, \ldots, N-1 \tag{104}$$

and

$$\hat{f}_\sigma = \sum_{\tau=0}^{N-1} f_\tau \, \mathrm{e}^{-2\pi i \frac{\tau\sigma}{N}} \; ; \quad \sigma = 0, 1, \ldots, N-1 \; , \tag{105}$$

where the signal f_τ in **c**-space and the spectrum $\hat{f}_\sigma$ in **k**-space form a discrete transform pair indicated by $f_\tau \Leftrightarrow \hat{f}_\sigma$ [2]. The application of the DFT implicitly requires a periodicity of the discrete signal and spectrum

$$f_\tau = f_{\tau+mN} \quad \text{and} \quad \hat{f}_\sigma = \hat{f}_{\sigma+mN} \; ; \quad m = 0, \pm 1, \pm 2, \ldots \; , \tag{106}$$

which means, that the N sampling values of both representing one period of a periodic (discrete) function. Instead to apply directly the discrete convolution to the integrals (23) and (24), we use the DFT to get an approximation of the Fourier transform $\hat{f}_{scat}(k_s) = \int_{-\infty}^{\infty} dc_s \, \mathrm{e}^{-2\pi i c_s k_s} \, f_{scat}(c_s)$ of the field particle distribution $f_{scat}(c_s)$, where the quality of this approximation depends strongly on the shape of the signal under consideration (cf., [52]). According to the relations (52) - (53), multiplications are performed in **k**-space to obtain the Fourier transforms of the Rosenbluth potentials and their derivatives. Afterwards, the DFT is applied once again for the approximation of the inverse Fourier transforms from which the friction (27) and diffusion (28) coefficients are computed in velocity space.

Numerical and Algorithmical Aspects of the FFT. A fast Fourier transform (FFT) is an efficient algorithm to compute the DFT and its inverse. FFTs are of great importance

[2] Note, the comparison with the continuous Fourier transformations requires a scaling with K_s and C_s, respectively, which are the constant sampling intervals in **k**- and **c**-space.

to a wide variety of applications, from digital signal processing to solving partial differential equations to algorithms for quickly multiplying large integers [55]. The DFT is defined by the formula (105) and can be rewritten as

$$F_n = \sum_{k=0}^{N-1} W^{n\,k}\, f_k \;; \quad n = 0, 1, \ldots, N-1 \quad \Longleftrightarrow \quad \mathbf{F} = \mathbb{W}\,\mathbf{f} \tag{107}$$

where the complex number W is given by

$$W = \mathrm{e}^{-2\pi i/N} \tag{108}$$

and $\hat{f}_n$ is replaced by F_n for convenience. In other words, the vector $\mathbf{f}$ is multiplied by a matrix $\mathbb{W}$, whose $(n,\, k)$-th element is the constant W to the power $n \cdot k$, yielding the vector $\mathbf{F}$ with components F_n. This matrix multiplication evidently requires N^2 complex multiplications, plus a smaller number of operations to generate the required powers of W. Evaluating these sums directly would take $\mathcal{O}(N^2)$ arithmetical operations [52]. The FFT computes the

1	000	001	010	011	100	101	110	111
2	0	1	2	3	4	5	6	7
3	0				1			
4	0	2	4	6	1	3	5	7
5	00		01		10		11	
6	0	4	2	6	1	5	3	6
7	000	001	010	011	100	101	110	111
8	0	4	2	6	1	5	3	7

FIGURE 5.3. Reordering phase in the case of 8 samples.

same result in only $\mathcal{O}\Big(N\,\log(N)\Big)$ operations. In general, such algorithms depend upon the factorisation of N, but (contrary to popular misconception) there are $\mathcal{O}\Big(N\,\log(N)\Big)$ FFTs for all N, even prime n. The difference between $N\,\log(N)$ and N^2 is immense: With $N = 10^6$, for example, it is the difference between, roughly, 30 seconds of CPU time and two weeks on a microsecond cycle time computer [54]. Since the inverse DFT is the same as the DFT, but with the opposite sign in the exponent and a $1/N$ factor, any FFT algorithm can easily be adapted for it as well. By far the most common FFT is the Cooley-Turkey algorithm. This method (and the general idea of an FFT) was popularised by a publication of J. W. Cooley and J. W. Turkey in 1965 [56], but it was later discovered that those two authors had independently re-invented an algorithm known to Carl Friedrich Gauss around 1805 [57] (and subsequently rediscovered by as many as a dozen individuals in limited forms [58]). This is a divide and conquer algorithm that recursively breaks down a DFT of any composite size

$N = N_1\, N_2$ into many smaller DFTs of sizes N_1 and N_2, along with $\mathcal{O}(N)$ multiplications by complex roots of unity traditionally called twiddle factors. Also, because the Cooley-Turkey algorithm breaks the DFT into smaller DFTs, it can be combined arbitrarily with any other algorithm for the DFT. Finally, although the basic idea is recursive, most traditional implementations rearrange the algorithm to avoid explicit recursion.
One rediscovery of the FFT, that of Danielson and Lanczos in 1942 [59], provides one of the clearest derivations of this algorithm. The Danielson and Lanczos lemma shows that a

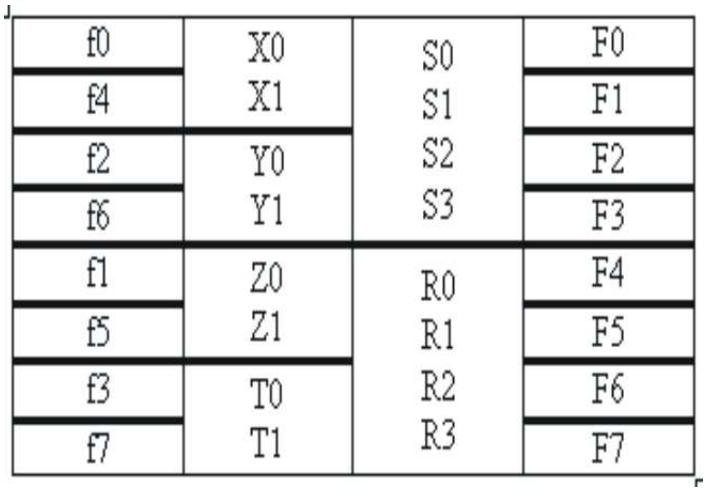

FIGURE 5.4. Combination phase in the case of 8 samples.

discrete Fourier transform of length N can be rewritten as the sum of two discrete Fourier transforms, each of length $N/2$. One of the two is formed from the even-numbered points of the original N, the other from the odd-numbered points. The proof is simply this:

$$\begin{aligned} F_n &= \sum_{j=0}^{N-1} \mathrm{e}^{-2\pi i \frac{j\,n}{N}}\, f_j \\ &= \sum_{j=0}^{N/2-1} \mathrm{e}^{-2\pi i \frac{n}{N}(2j)}\, f_{2j} + \sum_{j=0}^{N/2-1} \mathrm{e}^{-2\pi i \frac{n}{N}(2j+1)}\, f_{2j+1} \\ &= \sum_{j=0}^{N/2-1} \mathrm{e}^{-2\pi i \frac{j\,n}{N/2}}\, f_{2j} + W^n \sum_{j=0}^{N/2-1} \mathrm{e}^{-2\pi i \frac{j\,n}{N/2}}\, f_{2j+1} \\ &= F_n^e + W^n\, F_n^o\ . \end{aligned} \tag{109}$$

In the last line, W is the complex constant, F_n^e denotes the n^{th} component of the Fourier transform of length $N/2$ formed from the even components of the original f_j's, while F_n^o is the corresponding transform of length $N/2$ formed from the odd components. It is worthwhile to note that the evaluation of the DFT by just one splitting of the input sequence requires $N^2/2$ multiplications and $N^2/2$ additions which is a factor-of-two-savings, that is encouraging for further splitting. Although there are ways of treating other cases, by far the easiest case is the

one in which the original N is an integer power of 2. With this restriction on N, it is evident that we can continue applying the Danielson-Lanczos lemma until we have subdivided the data all the way down to transforms of length one. The Fourier transform of length one is just the identity operation that copies its one input number into its one output slot $\Big(\mathcal{F}\{A\,\delta(t)\} = A,$ with $A =$ constant $\Big)$!

This algorithm which belongs to the class of the *decimation-in-time* since it involves the splitting of the input (or time) sequence consists of two phases: a reordering stage in which the input array is successively subdivided into even and odd sequences and a combine phase, in which sequences of length 1 are combined into sequences of length 2 then sequences of length 2 into sequences of length 4 and so on until the final transform sequence is formed from two sequences of length $N/2$. Table 5.3 explains how to perform the former phase in a smart way, by means of the so-called bit-reversing order [54, 52]. Suppose that the input array consists, for simplicity of 8 samples, numbered from 0 to 7 (line 2). Moving the evens on the left side of table and the odds on the right means in other words to separate those positions which have rest 0 from those which have rest 1 when divided by 2, as indicated in the third line, yielding two sequences by four elements each. Inside these two new sequences (line 4) it is still possible to distinguish even and odd positions, which are rearranged as showed in line 6. This step corresponds to a further division by 2 whose rest is indicated as the second digit in line 5. Keeping on splitting the input sequence in an even/odd fashion until N sequences of length 1 remain, and assigning successively a 0 to the even and a 1 to the odd sequences, is evidently nothing else than the standard technique to convert from decimal to binary notation. Observing the first and the penultimate line of the table, it is evident that the original array is now rearranged in a fashion which could be directly obtained by simply reversing the binary sequences of its original entries, i.e. position number 4_{10}, $(100)_2$, goes finally to position 1, because $1_{10} = (001)_2$.

The combine phase starts now with N trivial one-point transforms. Then the sequences of length 1 are combined in pairs (f_0 with f_4, f_2 with f_6 ...) according to formula (109) to form DFTs of length 2 (see table 5.4). Again, DFTs sequences of length 2 are combined in pairs (X_0 and X_1 with Y_0 and Y_1 ...) to form two DFTs of length 4 ($N/2$) and finally these two are combined to form the desired F_k (see table 5.4).

Each combination takes of order N operations, and there are evidently $\log_2(N)$ combinations, so the whole algorithm is of order $N \log_2(N)$ (assuming, as is the case, that the process of sorting into bit-reversed order is no greater in order than $N \log_2(N)$). This, then, is the structure of an FFT algorithm: It has two sections. The first section sorts the data into bit-reversed order, but this takes no additional storage, since it involves only swapping pairs of elements (If k_1 is the bit reverse k_2, then k_2 is the bit reverse of k_1). The second section has an outer loop that is executed $\log_2 N$ times and calculates, in turn, transforms of length 2, 4, 8, .., N. For each stage of this process, two nested inner loops range over the subtransforms already computed and the elements of each transform, implementing the Danielson-Lanczos lemma. The operation is made more efficient by restricting external calls for trigonometric

sines and cosines to the outer loop, where they are made only $\log_2(N)$ times. Computation of the sines and cosines of multiple angles is through simple recurrence relations in the inner loops.

Problems and Remedies. The most important class of signals appearing in practical applications are those with an arbitrary unlimited shape in **c**-space which are not band limited in **k**-space. To obtain a discrete signal one has to multiply the arbitrary distribution function $f_{scat}(c)$ with the sampling (or repetition) function $\mathrm{rep}_{C_s}\delta\big(c\big) = \sum_{n=-\infty}^{\infty} \delta\big(c - n\,C_s\big)$ $\Big($with the transform pair:
$\mathrm{rep}_{C_s}\delta\big(c\big) \Leftrightarrow \frac{1}{C_s}\mathrm{rep}_{1/C_s}\delta\big(k\big)$ $\Big)$ to get

$$f_s(c) = f_{scat}(c)\ \mathrm{rep}_{C_s}\delta\big(c\big) = \sum_{n=-\infty}^{\infty} f_{scat}(nC_s)\ \delta\big(c - n\,C_s\big)\ , \tag{110}$$

where C_s is the sample interval. In general, the spectrum $\hat{f}_{scat}(k)$ of the signal $f_{scat}(c)$ is not band limited and aliasing is natural consequence of the sampling process. To reduce the influence of aliasing it is recommended to sample the signal with high "frequency" $1/C_s$ which means, with a sufficient small C_s.
Clearly, the discrete signal (110) is not suitable for numerical purposes because an infinite number of sampling points are used. Therefore, the sampling signal $f_s(c)$ have to be limited in velocity space by the application, for instance, of the rectangle function of unit height

$$\mathrm{rect}_{C_0}(c) = \begin{cases} 1\ , & \frac{C_s}{2} \le c \le C_0 - \frac{C_s}{2} \\ 0\ , & \text{else} \end{cases}\ , \tag{111}$$

where C_0 is the duration of the limitation and
$\mathrm{rect}_{C_0}(c) \Leftrightarrow \mathrm{e}^{-\pi i k(C_0 - C_s)}\ \frac{sin(\pi k C_0)}{\pi k}$. Then, the velocity limitation yields

$$f_w(c) = f_s(c)\ \mathrm{rect}_{C_0}(c) = \sum_{n=0}^{N-1} f_{scat}(nC_s)\ \delta\big(c - n\,C_s\big)\ , \tag{112}$$

where it is assumed that N equidistant δ-functions occur within the period of observation, that is $C_0 = N\,C_s$. The difficult point concerns the choice of the duration of the observation. It is well-known that for the ideal case of a band limited periodic signal the observation duration C_0 should be the period of the signal or a multiple of this period. Otherwise – greater than a period –, additional "frequency" components are generated in the Fourier transform $\hat{f}_{scat}(k)$, which leads to ripples in the spectrum and sharp discontinuities of the signal in velocity space. These discontinuities are also expected in the case of an arbitrary signal, where the period is determined by the number N of sampling points. A convenient remedy to cure these "errors" (side lobes amplitudes) is to replace the rectangle velocity limitation by a more appropriate window functions. The net effect, for instance, of the Hanning-function is a strong attenuation of the rectangle function induced discontinuities [54, 52].

Interpolation Block. After the grid-based computations are executed, the essential information

(derivation of the Rosenbluth potentials) has to be brought onto the particle location in velocity space. This link between the grid-based and mesh-free numerical model is established by the interpolation step, which is nothing else than the inverse operation of the assignment procedure. The friction and diffusion coefficients $R_p(t_n) = \left\{ F_\rho,\, D_{\rho\sigma};\, \rho,\sigma = 1,2,3 \right\}$ at the velocity $\mathbf{V}_p^n$ of the p^{th} particle at time t_n are computed from the coefficients $R_{i,j,k}^n$ stored at the surrounding nodes $\mathbf{v}_{i,j,k}$ of the actual velocity grid. For this task, we apply the volume-weighting interpolation formula [14]

$$R_p(t_n) = \sum_{\mu,\nu,\lambda=0}^{1} g_{i+\mu,j+\nu,k+\lambda}^{(p)}\, R_{i+\mu,j+\nu,k+\lambda}^{n} \;, \tag{113}$$

where the weights $g_{i,j,k}^{(p)}$ are already determined in the assignment step. The fact that the particle-based weights (113) have to be computed only once at the interface mesh-free/grid-based and used for assignment as well as for interpolation is a very attractive feature, which enhance the efficiency of the numerical scheme. Finally note, that the way of computing the particle weights (102) reveals that interpolation and assignment are multidimensional linear approximations.

Langevin Solver. Simulations of phenomena caused by a non-neutral plasma requires the solution of the time-dependent Maxwell-Vlasov equations in two or even three dimensions in space [4]. The numerical method of choice to solve this non-linear problem is the PIC method. There, the Lorentz force at the charged particle position is responsible for the redistribution of the different particle ensembles. The new phase-space coordinates are obtained by the numerical solution of the deterministic Lorentz equations, where the special tailored leapfrog scheme of Boris is applied [25].

In the context of the present PIC approach, the Langevin "forces", which consists of the deterministic friction and the stochastic diffusion moves the particles in velocity space. Under the action of these velocity-dependent Langevin forces, each particle evolve in velocity space according to the Langevin-type equation (82). However, this equation represents a SDE whose mathematical character contrasts sharply with the deterministic Lorentz equation. Especially, this fundamental difference find expression in the numerical approximation of the stochastic law of dynamics (82).

The numerical solution of SDEs requires to determine random numbers and the schemes are classified in strong and weak convergence approximations. Unfortunately, a clear and stringent distinction between both approximations for a SDE is seldom found in literalture [41, 60, 39]. If one is interested in the individual trajectories of the dynamical system described by the SDE, (explicit) strong Itô-Taylor schemes (see App. H) are appropriate because they ensure a pathwise approximation. Roughly speaking, this kind of approximation need the resolution of the "inner structure" of the random variables, which is difficult to achieve and a very CPU time consuming. Weak and explicit weak Itô-Taylor schemes are reasonable for application where one is only interested in the computation of moments or functionals of moments. Such approximations are not as demanding as pathwise approximations because

they require only that probability distribution of two random variables are (sufficiently) close to each other, but not the actual realisation of these random variable. In the following we present an explicit weak, order two Itô-Taylor scheme.

5.3. **Weak Itô -Taylor Approximations for the Langevin-Type Equation.** In this section, a discrete approximation $\mathbf{V}_n = \mathbf{V}(t_n)$ of an Itô process $\mathbf{C} = \Big\{\mathbf{C}(t)\,|\,t_0 \le t \le T\Big\}$ satisfying the Langevin-type equation (82) on $t_0 \le t \le T$ with initial data $\mathbf{C}_0 = \mathbf{C}(t_0)$ is searched. Especially, for a given discretisation $t_0 < t_1 < t_2 \cdots < t_N = T$ of the interval $[t_0,\, T]$ – in the following with constant Δt –, an iterative scheme of the form $\mathbf{V}_{n+1} = \mathbf{G}\big(\mathbf{V}_n, t_n\big)$, for $n = 0,\, 1,\, 2,\, \ldots\, N-1$, with initial value $\mathbf{V}_0 = \mathbf{C}(t_0)$ is desired, where $\mathbf{G}$ represents a function of the previous approximation step.

Weak Order 1.0 Euler Scheme.

The simplest time discrete approximation of the Itô process $\mathbf{C}$ is the Euler approximation, which shows weak convergence order $\beta = 1.0$ under suitable conditions on the friction and diffusion coefficients (for this and the following, especially, the convergence proofs of the schemes we refer to Kloeden & Platen [49]). The starting point to obtain this scheme is the weak ITE (cf. eq. 94) for the hierarchical set $\Gamma_{1.0}$ (see App. G). In the multi-dimensional case (that is $d = 3$ spacial dimensions and $m = 3$ independent Wiener processes in the following) this truncated expansion reads as

$$\mathbf{C}\big(t_0 + \Delta t\big) = \mathbf{C}\big(t_0\big) + \mathbf{F}\big\{t_0\big\}\,\mathcal{I}_{(0)} + \sum_{q=1}^{m} \mathbf{b}_q\big\{t_0\big\}\,\mathcal{I}_{(q)}\ , \tag{114}$$

where the notation of Chap. 4 is used. A central task in the context of weak schemes is to find appropriate approximations of multiple Itô integrals and, especially, to compute expectation values of products of such integrals in order to get correlations and corresponding moment conditions for these random objects. From definition (93) it is clear that the former Itô integral appearing on the right-hand side (rhs) of (114) is a constant: $\mathcal{I}_{(0)} = \Delta t$. For the latter, multiplicity one integral $\mathcal{I}_{(q)}$ it is immediately obvious – from the zero expectation property of Itô integrals – that $\mathcal{E}\Big\{\mathcal{I}_{(q)}\Big\} = 0$. To get more information about the correlations of this object with others, we have to compute, for instance, $\mathcal{E}\Big\{\mathcal{I}_{(p)}\,\mathcal{I}_{(q)}\Big\}$. It is straightforward to show that

$$\mathcal{E}\Big\{\mathcal{I}_{(p)}\,\mathcal{I}_{(q)}\Big\} = \Delta t\ \delta_{p\,q}\ , \tag{115}$$

where $\delta_{p\,q}$ denotes the Kronecker delta symbol. This short discussion suggests to replace the Itô integral $\mathcal{I}_{(q)}$ by a Gaussian random variable ΔW_n^q with the moment properties $\mathcal{E}\Big\{\Delta W_n^q\Big\} = 0$ and $\mathcal{E}\Big\{\big(\Delta W_n^q\big)^2\Big\} = \Delta t$. Then, the multi-dimensional weak Euler scheme (also known as Euler-Maruyama scheme) may be written in the form

$$\mathbf{V}_{n+1} = \mathbf{V}_n + \Delta t\,\mathbf{F}\big\{t_n\big\} + \sqrt{\Delta t}\,\sum_{q=1}^{m} \mathbf{b}_q\big\{t_n\big\}\,\eta_n^q\ , \tag{116}$$

where we introduced that $\Delta W_n^q = \sqrt{\Delta t}\,\eta_n^q$. Here, η_n^q is a Gaussian random number with mean $\mathcal{E}\Big\{\eta_n^q\Big\} = 0$ and variance $\mathcal{V}ar\Big(\eta_n^q\Big) = \mathcal{E}\Big\{\big(\eta_n^q\big)^2\Big\} - \Big(\mathcal{E}\Big\{\eta_n^q\Big\}\Big)^2 = 1$; this fact is often compactly expressed by the notation $\eta_n^q \sim \mathcal{N}\big(0,\,1\big)$. As mentioned, a characteristic feature of weak approximation is the freedom to replace multiple Itô integrals by simple random numbers which coincide with the lower order moments. Since only an accurate representation of the probability law of an Itô process is important, we can proceed and interchange the Gaussian increments $\Delta W_n^q \sim \mathcal{N}\big(0,\,\Delta t\big)$ by simpler, for instance, two-point distributed random variables $\Delta\hat{W}_n^q$ with $Prob\Big(\Delta\hat{W}_n^q = \pm\sqrt{\Delta t}\Big) = 1/2$. In general, the moments of the independent random numbers $\Delta\hat{W}_n^q$ must fulfil the condition

$$\Big|\mathcal{E}\Big\{\Delta\hat{W}_n^q\Big\}\Big| + \Big|\mathcal{E}\Big\{(\Delta\hat{W}_n^q)^3\Big\}\Big| + \Big|\mathcal{E}\Big\{(\Delta\hat{W}_n^q)^2\Big\} - \Delta t\Big| \leq K\,(\Delta t)^2$$

for some constant K. Finally, keep in mind that according to the definition of $\mathbf{b}_q$ (see section 4.6) no derivatives of the friction and diffusion coefficients with respect to the variable C appear in the weak Euler scheme (116) – a reason why this scheme is "the workhorse" in stochastic computation. And furthermore, note that a first order strong scheme yet requires additional approximations of double stochastic Itô integrals (see App. H).

Weak Order 2.0 Itô-Taylor Scheme.

As one would expected, a higher order accurate weak scheme requires much more numerical effort to include more information about the probability measure of the underlying Itô process. Indeed, the desired order of the weak convergence also determines which truncation of the ITE (94) must be used. To obtain second order of weak convergence, all double stochastic integrals of the ITE are now necessary. In other words, the expansion has to be performed for the hierarchical set $\Gamma_{2.0}$ (see App. G) and reads as

$$\begin{aligned}
\mathbf{C}(t_0+\Delta t) \;&=\; \mathbf{C}(t_0) + \mathbf{F}\big\{t_0\big\}\,\mathcal{I}_{(0)} + \sum_{p=1}^{m}\mathbf{b}_p\big\{t_0\big\}\,\mathcal{I}_{(p)} \\
&+\; \sum_{p,q=1}^{m}\Big[\mathbf{b}_p\cdot\nabla_c\,\mathbf{b}_q\Big]\big\{t_0\big\}\,\mathcal{I}_{(p,q)} + \sum_{p=1}^{m}\Big[\mathbf{b}_p\cdot\nabla_c\,\mathbf{F}\Big]\big\{t_0\big\}\,\mathcal{I}_{(p,0)} \\
&+\; \sum_{p=1}^{m}\Big[\mathcal{L}^{(0)}\,\mathbf{b}_p\Big]\big\{t_0\big\}\,\mathcal{I}_{(0,p)} + \Big[\mathcal{L}^{(0)}\,\mathbf{F}\Big]\big\{t_0\big\}\,\mathcal{I}_{(0,0)}\;, \qquad (117)
\end{aligned}$$

with the notation introduced in Chap. 4, where, additionally, the operator $\mathcal{L}^{(p)}$ (85) is identified by $\mathcal{L}^{(p)} = \mathbf{b}_p\cdot\nabla_c$. Similar as above for $\mathcal{I}_{(0)}$, we obtain from the definition of the Itô integral (96) that $\mathcal{I}_{(0,0)}$ is also a constant given by $\mathcal{I}_{(0,0)} = \frac{1}{2}\big(\Delta t\big)^2$. Furthermore, we notice that the expectation of all other Itô integrals vanish due to (75). In spirit of weak approximation, we now successively replace the remaining Itô integrals by simpler noise increments, for instance, first by independently distributed Gaussian random variables. First of all, we consider the double integral $\mathcal{I}_{(p,0)}$ and ascertain that the second moment – which

is equivalent to the variance – is given by

$$\mathcal{E}\Big\{\mathcal{I}_{(p,0)}\,\mathcal{I}_{(q,0)}\Big\} = \frac{1}{3}(\Delta t)^3\;\delta_{p\,q}\;, \tag{118}$$

while the correlation with the integral $\mathcal{I}_{(p)}$ reads as

$$\mathcal{E}\Big\{\mathcal{I}_{(p)}\,\mathcal{I}_{(q,0)}\Big\} = \frac{1}{2}(\Delta t)^2\;\delta_{p\,q}\;. \tag{119}$$

These results suggest to substitute $\mathcal{I}_{(p,0)}$ by a normally distributed random number ΔZ_n^p with mean $\mathcal{E}\Big\{\Delta Z_n^p\Big\} = 0$, variance $\mathcal{E}\Big\{(\Delta Z_n^p)^2\Big\} = 1/3(\Delta t)^3$ and covariance $\mathcal{E}\Big\{\Delta W_n^p\,\Delta Z_n^p\Big\} = 1/2(\Delta t)^2$, where ΔW_n^p is the random number "image" of $\mathcal{I}_{(p)}$ (cf., relation (115)). For sake of completeness, we have to mention that such a pair of correlated normally distributed random variables is obtained from the relations

$$\Delta W_n^p = \big(\Delta t\big)^{1/2}\,G_1 \quad \text{and} \quad \Delta Z_n^p = \frac{1}{2}\big(\Delta t\big)^{3/2}\Big(G_1 + 3^{-1/2}\,G_2\Big)\;, \tag{120}$$

where $G_1 \sim \mathcal{N}(0,1)$ and $G_2 \sim \mathcal{N}(0,1)$ are two independent standard Gaussian increments. Since $\mathcal{I}_{(0,p)}$ possesses the same probability measure that $\mathcal{I}_{(p,0)}$ does (see, expressions (118) and (119)), we conclude with the help of relation

$$\mathcal{I}_{(0,p)} = \Delta t\,\mathcal{I}_{(p)} - \mathcal{I}_{(0,p)} \tag{121}$$

that the multiple Itô integral $\mathcal{I}_{(0,p)}$ may be replaced by the random number $\Big[\Delta t\,\Delta W_n^p - \Delta Z_n^p\Big]$. In order to reduce the remaining Itô integrals $\mathcal{I}_{(p,q)}$ to appropriate random variables, we consider first the case $p = q$ and refer to the footnote 1. From there we recognise that $\mathcal{I}_{(p,p)}$ is essentially a Hermite polynomial in $\mathcal{I}_{(p)}$:

$$\mathcal{I}_{(p,p)} = \frac{\Delta t}{4}\,H_2\bigg(\frac{\mathcal{I}_{(p)}}{\sqrt{2\,\Delta t}}\bigg) = \frac{1}{2}\Big(\mathcal{I}_{(p)}^2 - \Delta t\Big)\;, \tag{122}$$

and, consequentely, $\mathcal{I}_{(p,p)}$ can be represented by the random number $\frac{1}{2}\Big[(\Delta W_n^p)^2 - \Delta t\Big]$. To investigate the case $p \neq q$, we can start from the ansatz

$$\mathcal{I}_{(p,q)} = \frac{1}{2}\Big(\mathcal{I}_{(p)}\,\mathcal{I}_{(q)} + R_{p,q}\Big)\;, \tag{123}$$

where $R_{p,q}$ is still unknown. Clearly, with the result (122), $R_{p,q}$ can be identified for $p = q$ with $R_{p,q} = -\Delta t$. Setting p and q equal to $p = \mu + 1$ and $q = \mu$ for $\mu = 1, 2, \ldots$, it is pretty evident that the mean and variance of $R_{\mu+1,\mu}$ are given by $\mathcal{E}\Big\{R_{\mu+1,\mu}\Big\} = 0$ and $\mathcal{E}\Big\{R_{\mu+1,\mu}^2\Big\} = (\Delta t)^2$, respectively, where the relation $\mathcal{E}\Big\{\mathcal{I}_{(p,q)}\,\mathcal{I}_{(r,s)}\Big\} = 1/2(\Delta t)^2\,\delta_{pr}\,\delta_{qs}$ is applied. By means of the observation $W^{\mu+1}\,\mathcal{I}_{(\mu)} = \mathcal{I}_{(\mu+1,\mu)} + \mathcal{I}_{(\mu,\mu+1)}$ and the replacement $\mathcal{I}_{(p)} \leftrightarrow W^p$, we further find that $R_{\mu,\mu+1} = -R_{\mu+1,\mu}$. This brings to the conclusion that $R_{p,q}$ in (123) can be replaced, for instance, by a Gaussian random variable of the form

$$R_n^{p,q} = \Delta t\;G_n^{p,q} \quad \text{and} \quad R_n^{q,p} = -R_n^{p,q} \tag{124}$$

with $G_n^{p,q} \sim \mathcal{N}(0,1)$ for $p > q$, which has the desired property, namely, $R_n^{p,q} \sim \mathcal{N}\Big(0, (\Delta t)^2\Big)$. Proceeding further on in the spirit of weak approximation we finally replace ΔZ_n^p by the simpler random number $\Delta Z_n^p = \frac{1}{2}\Delta t\,\Delta W_n^p$ which obeys obviously the expectation values $\mathcal{E}\Big\{(\Delta Z_n^p)^2\Big\} \sim (\Delta t)^3$ and $\mathcal{E}\Big\{\Delta W_n^p\,\Delta Z_n^p\Big\} \sim (\Delta t)^2$. Note, that also ΔW_n^p and $R_n^{p,q}$ could be

substituted by simpler three- and two-point distributed random numbers, respectively, with corresponding probability properties. Replacing then in the ITE (117) the multiple Itô integrals by the simpler random numbers which are introduced in the preceding considerations, we obtain after some rearrangements

$$\begin{aligned}
\mathbf{V}_{n+1} &= \mathbf{V}_n + \Delta t \left(\mathbf{F}\big\{t_n\big\} + \frac{\Delta t}{2}\Big[\mathcal{L}^{(0)}\,\mathbf{F}\Big]\big\{t_n\big\} + \frac{1}{2}\sum_{p=1}^{m} W_n^p \Big[\mathbf{b}_p \cdot \nabla_c\,\mathbf{F}\Big]\big\{t_n\big\} \right) \\
&+ \sum_{p=1}^{m} \Delta W_n^p \left(\mathbf{b}_p\big\{t_n\big\} + \frac{\Delta t}{2}\Big[\mathcal{L}^{(0)}\,\mathbf{b}_p\Big]\big\{t_n\big\} \right) \\
&+ \frac{1}{2}\sum_{p=1}^{m} \Bigg(\Big[\mathbf{b}_p \cdot \nabla_c\,\mathbf{b}_p\Big]\big\{t_n\big\}\,\Big[(\Delta W_n^p)^2 - \Delta t\Big] \\
&+ \sum_{\substack{q=1 \\ q\neq p}}^{m} \Big[\mathbf{b}_q \cdot \nabla_c\,\mathbf{b}_p\Big]\big\{t_n\big\}\,\Big[\Delta W_n^p\,\Delta W_n^q + R_n^{p,q}\Big] \Bigg)\,, \qquad (125)
\end{aligned}$$

which represents the desired (non derivative free) order $\beta = 2.0$ weak Itô-Taylor scheme in its preliminary form. Concerning the consistency of this weak scheme we refer to Appendix I.
It is obvious from (125) that the order two weak Itô-Taylor scheme requires the evaluation of derivatives up to second order of the friction and derived diffusion coefficients. However, in self-consistent computations these coefficients are not analytically known in the course of the simulation and, hence, it is desireable to avoid the use of such derivatives. Schemes which fulfil this requirement are known as explicit schemes and are not just an extensions of deterministic Runge-Kutta methods.
To obtain a completely derivative free order two weak Itô-Taylor scheme from (125) several approximations have to be performed which are described in the following.

- First approximation: Starting from

  $$\Delta\mathbf{F} = \mathbf{F}\big(\mathbf{V}_{n+1}^{\star}\big) - \mathbf{F}\big(\mathbf{V}_n\big)\,,$$

  where the auxiliary vector $\mathbf{V}_{n+1}^{\star}$ is estimated from

  $$\mathbf{V}_{n+1}^{\star} = \mathbf{V}_n + \mathbf{F}(\mathbf{V}_n)\,\Delta t + \sum_{p=1}^{m} \mathbf{b}_p(\mathbf{V}_n)\,\Delta W_n^p \qquad (126)$$

  and $\Delta\mathbf{F}$ is determined by means of the Itô formula (83), get

  $$\frac{1}{2}\Big[\mathbf{F}\big(\mathbf{V}_{n+1}^{\star}\big) + \mathbf{F}\big(\mathbf{V}_n\big)\Big] \approx \mathbf{F} + \frac{\Delta t}{2}\Big[\mathcal{L}^{(0)}\,\mathbf{F}\Big] + \frac{1}{2}\sum_{p=1}^{m} W_n^p \Big[\mathbf{b}_p \cdot \nabla_c\,\mathbf{F}\Big] \qquad (127)$$

  Note, that the "predictor step" (126) represents nothing else than the first order weak Euler scheme already introduced by (116).
- Second approximation: Introducing the support vector

  $$\mathbf{T}_p^{\pm} = \mathbf{V}_n + \mathbf{F}(\mathbf{V}_n)\,\Delta t \pm \mathbf{b}_p(\mathbf{V}_n)\,\sqrt{\Delta t} \qquad (128)$$

and performing a deterministic Taylor expansion for $\Psi\Big(\mathbf{T}_p^{\pm}\Big)$ up to first order in Δt, we obtain

$$\mathbf{b}_p \cdot \nabla_c \Psi \approx \frac{1}{2\sqrt{\Delta t}} \Big[\Psi\Big(\mathbf{T}_p^{+}\Big) - \Psi\Big(\mathbf{T}_p^{-}\Big) \Big] \tag{129}$$

and

$$\begin{aligned} \Psi\Big(\mathbf{T}_p^{+}\Big) + \Psi\Big(\mathbf{T}_p^{-}\Big) &\approx 2\,\Psi\Big(\mathbf{V}_n\Big) + 2\,\Delta t \Bigg(\mathcal{L}^{(0)}\,\Psi \\ &- \frac{1}{2} \sum_{\substack{q \\ q \neq p}} \sum_{i,k} B_{iq}\, B_{kq} \frac{\partial^2 \Psi}{\partial c_i \partial c_k} \Bigg) , \end{aligned} \tag{130}$$

where B_{iq} are the coefficients of matrix $\mathbb{B}$. From the latter relation (130) we conclude that

$$\begin{aligned} \sum_p \Delta W_n^p \left(\mathbf{b}_p + \frac{\Delta t}{2}\, \mathcal{L}^{(0)}\, \mathbf{b}_p \right) &\approx \frac{1}{4} \sum_p \Delta W_n^p \Bigg(\mathbf{b}_p\Big(\mathbf{T}_p^{+}\Big) \\ &+ \mathbf{b}_p\Big(\mathbf{T}_p^{-}\Big) 2\, \mathbf{b}_p\Big(\mathbf{V}_n\Big) \\ + \Delta t \sum_{\substack{q \\ q \neq p}} \sum_{i,k} B_{iq}\, B_{kq} \frac{\partial^2}{\partial c_i \partial c_k} &\ \mathbf{b}_p \ \Big(\mathbf{V}_n\Big) \Bigg) . \end{aligned} \tag{131}$$

- Third approximation. A further deterministic Taylor expansion for $\Psi\Big(\mathbf{U}_q^{\pm}\Big)$ up to Δt with the auxiliary vector

$$\mathbf{U}_q^{\pm} = \mathbf{V}_n \pm \mathbf{b}_p(\mathbf{V}_n)\, \sqrt{\Delta t}\, , \quad q \neq p \tag{132}$$

yields

$$\mathbf{b}_q \cdot \nabla_c \Psi \approx \frac{1}{2\sqrt{\Delta t}} \Big[\Psi\Big(\mathbf{U}_q^{+}\Big) - \Psi\Big(\mathbf{U}_q^{-}\Big) \Big] \tag{133}$$

and

$$\Psi\Big(\mathbf{U}_q^{+}\Big) + \Psi\Big(\mathbf{U}_q^{-}\Big) - 2\,\Psi\Big(\mathbf{V}_n\Big) \approx \Delta t \sum_{i,k} B_{iq}\, B_{kq} \frac{\partial^2 \Psi}{\partial c_i \partial c_k} \, . \tag{134}$$

Inserting the latter result into (131), we immediately get

$$\begin{aligned} \sum_p \Delta W_n^p \left(\mathbf{b}_p + \frac{\Delta t}{2}\, \mathcal{L}^{(0)}\, \mathbf{b}_p \right) &\approx \frac{1}{4} \sum_p \Delta W_n^p \Bigg(\mathbf{b}_p\Big(\mathbf{T}_p^{+}\Big) \\ &+ \mathbf{b}_p\Big(\mathbf{T}_p^{-}\Big) 2\, \mathbf{b}_p\Big(\mathbf{V}_n\Big) \\ + \sum_{\substack{q \\ q \neq p}} \mathbf{b}_p\Big(\mathbf{U}_q^{+}\Big) + \mathbf{b}_p\Big(\mathbf{U}_q^{-}\Big) &- 2\, \mathbf{b}_p\Big(\mathbf{V}_n\Big) \Bigg) . \end{aligned} \tag{135}$$

Substituting the expressions (127), (135), (129) and (133) into (125), we obtain an explicit order $\beta = 2.0$ weak Itô-Taylor scheme [49] which reads as

$$\begin{aligned}
\mathbf{V}_{n+1} &= \mathbf{V}_n + \frac{\Delta t}{2}\Big[\mathbf{F}\big(\mathbf{V}^{\star}_{n+1}\big) + \mathbf{F}\big(\mathbf{V}_n\big)\Big] \\
&+ \frac{1}{4}\sum_{p=1}^{m}\Bigg\{\Big[\mathbf{b}_p(\mathbf{T}_p^{+}) + \mathbf{b}_p(\mathbf{T}_p^{-}) + 2\,\mathbf{b}_p(\mathbf{V}_n)\Big]\,\Delta W_n^p \\
&+ \sum_{\substack{q=1\\ q\neq p}}^{m}\Big[\mathbf{b}_p(\mathbf{U}_q^{+}) + \mathbf{b}_p(\mathbf{U}_q^{-}) - 2\,\mathbf{b}_p(\mathbf{V}_n)\Big]\,\Delta W_n^p\Bigg\} \\
&+ \frac{1}{4\sqrt{\Delta t}}\sum_{p=1}^{m}\Bigg\{\Big[\mathbf{b}_p(\mathbf{T}_p^{+}) - \mathbf{b}_p(\mathbf{T}_p^{-})\Big]\Big[(\Delta W_n^p)^2 - \Delta t\Big] \\
&+ \sum_{\substack{q=1\\ q\neq p}}^{m}\Big[\mathbf{b}_p(\mathbf{U}_q^{+}) - \mathbf{b}_p(\mathbf{U}_q^{-})\Big]\Big[\Delta W_n^p\,\Delta W_n^q + R_n^{p,q}\Big]\Bigg\} \qquad (136)
\end{aligned}$$

where we skip the explicit time dependence of the vector functions $\mathbf{F}$ and $\mathbf{b}_p$, the subscripts "n" and "$n+1$" abbreviate, respectively, the time levels t_n and $t_{n+1} = t_n + \Delta t$. Furthermore, the occurring auxiliary vectors are defined by the relations (126), (128) and (132).

6. Results

6.1. **Introduction.** The goal of this section is the assessment of the Fokker-Planck module which is used to describe the effects of Coulomb collisions in plasmas. The program has been developed according to the building block structure depicted in Fig. 2.1. Each of these puzzle pieces has been tested separately and together to prove the approximation characteristics of the whole numerical code; in this respect the benefits of the renormalisation technique for energy and momentum conservation are shown. The problem of obtaining a good resolution of the distribution function, even in presence of a low number of particles, has been successfully overcome by means of a noise reduction method. The renormalisation technique normally used for avoiding finite sample instabilities problems in equilibrium status has been applied for the conservation of global energy and momentum in transient conditions. Afterwards, this tool was used to get a better insight of the collision phenomenon initially for the inter-species and intra-species cases separately and then coupled. Finally, results for self-consistent study of the time scaling are also presented.

6.2. **Building Blocks Validation.** In this section the three dimensional extension of the results obtained in [61] is presented; in fact the isotropic hypothesis is here abandoned in favour of a most general, cartesian treatment. The validation of the 3D-Rosenbluth solver is skipped since the evaluation of the Friction and Diffusion forces for a known case has been already discussed in Sec. 3.7. Here again the L_2 Norm of the error has been assumed as the figure of merit for the comparison between numerical and exact solution since level curves, slices and so on, can only give a partial visualisation of the numerical evaluation.

6.2.1. *Experiment 1: Mesh-free/Grid-based Handling.* Since interpolation is the inverse operation of the assignment procedure, in this experiment we restrict ourselves to inspect only the latter.

As pointed out in the previous chapters, an accurate reconstruction of the distribution function is fundamental for the evaluation of the forces acting on the particles. A trade-off between the discretisation interval (basically the ratio of the interval width and the number of grid points N_G), the number of particles N_p must be found in order to get a smooth, accurate distribution function in a reasonable computation time. For this, we generate $N = 3 \cdot 10^4$ Gaussian distributed (pseudo) random numbers with mean $\mu = 0$ and variance $\sigma^2 = 1$ which represent the velocity in x, y and z directions of the N_p particles in the mesh-free velocity space. After the localisation with respect to the velocity grid, each particle contributes according to its weights (99) to the particle distribution function whose slices at different heights are projected on the plane $c_z = 0$ and depicted in Fig. 6.1 and Fig. 6.2 for a coarse ($N_G = 32$) and in Fig. 6.3 and Fig. 6.4 two finer ($N_G = 64$ and $N_G = 128$ respectively) velocity grids. As expected, the 32 points resolution is quite poor, a fact that is especially evident if contour lines are extracted from the intersection between the distribution function evaluated at $c_z = 0$ and a surface perpendicular to the plane (c_x, c_z). As highlighted both by the two-dimensional plot and by the L_2 norm of the error, a much better agreement between

the numerical resolution and the analytical expression is obtained increasing the number of grid points, as shown in 6.3. It is worthwhile to note how this is not always the remedy, since an excessive number of grid points can result in a noisy distribution function, as shown in Fig. 6.4.

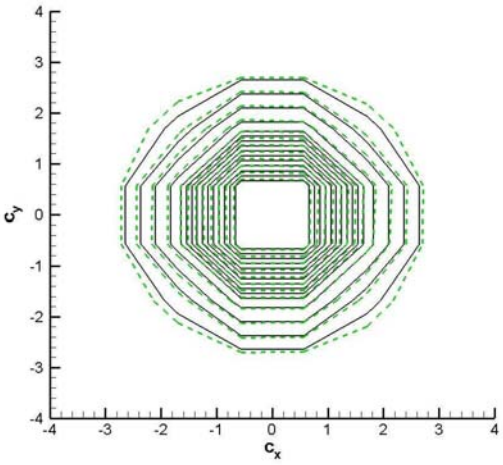

FIGURE 6.1. Level lines of the distribution function reconstructed on a 32 grid points with $3 \cdot 10^4$ particles (continuous line) and comparison with the the numerical resolution (dashed line), $L_2\{err\} \sim 0.52$ %.

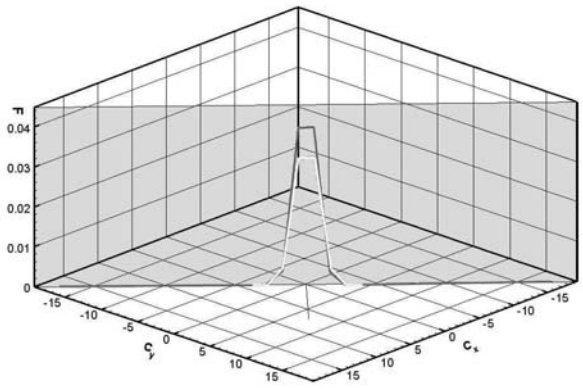

FIGURE 6.2. Profiles extracted from the intersection of $f_{num}(c_x, c_y, 0)$ and $f_{exact}(c_x, c_y, 0)$, light and bold line respectively, with a surface $\perp$ (c_x, c_y). Very poor resolution and mismatch are pretty evident

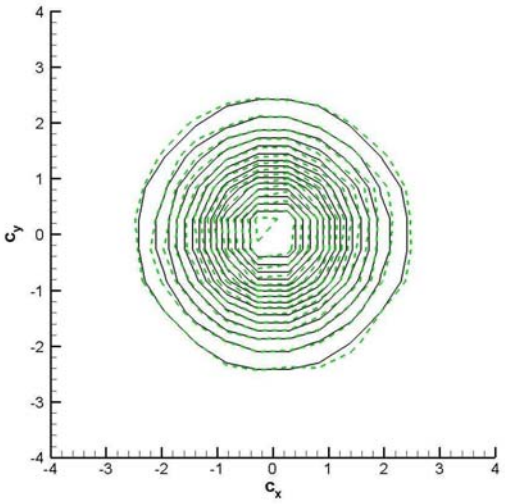

FIGURE 6.3. The 64 N_G reconstruction shows is good agreement with f_{exact}, shows a high resolution and very low $L_2\{err\} \sim 0.12$ %

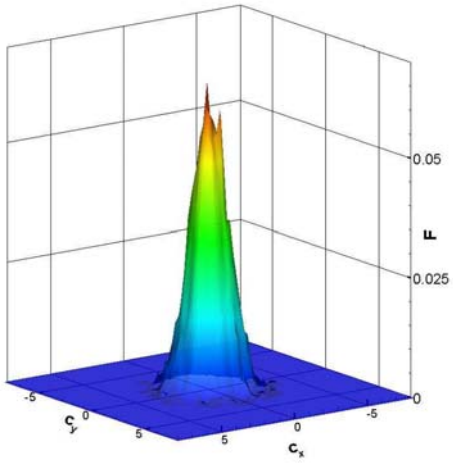

FIGURE 6.4. 128 grid points $f_{num}(c_x, c_y, 0)$ displays a very noisy shape as a result of a too small ΔC^3, $L_2\{err\} \sim 2.01$ %

6.2.2. *Experiment 2: Mesh-free Approximations (Langevin Solver).* The particles law of motion in mesh-free velocity space is established by the SDE (116) and (136), where the friction and diffusion coefficients are unknown functions of velocity and time. The intention of the present experiment is to study the approximation behaviour and quality of the applied explicit Itô-Taylor scheme (114), which is one building block of the Fokker-Planck module. To do this, we start from the very simple – but analytical

solvable – situation, where the friction vector and diffusion matrix are given by

$$\mathbf{F}(\mathbf{C},t) = -\,\alpha\,\mathbf{C} \quad \text{and} \quad \mathbb{B}(\mathbf{C},t) = \begin{pmatrix} \beta_{11} & 0 & \beta_{13} \\ 0 & \beta_{22} & 0 \\ \beta_{31} & 0 & \beta_{33} \end{pmatrix} \tag{137}$$

respectively, with constants α and β_{ij}. The corresponding linear SDE (which is the Langevin equation) reads as

$$d\mathbf{C}(t) = -\,\alpha\,\mathbf{C}(t)\,dt + \sum_{q=1}^{3} \mathbf{b}_q dW_t^q \tag{138}$$

which possesses the analytical solution [49] for the mean $\mathbf{m}(t)$ and for the second moment $\mathbb{P}(t)$

$$\begin{aligned} \mathbf{C}(t) &= \mathbf{C}(t_0)\,e^{-\alpha(t-t_0)} \\ \mathbb{P}(t) = \mathbb{P}(t_0)\,e^{-2\alpha t} &+ \frac{1}{2\,\alpha}\left(1 - e^{-2\alpha t}\right)\,\mathbb{M} \end{aligned} \tag{139}$$

where the matrix $\mathbb{M}$ is given by

$$\mathbb{M} = \begin{pmatrix} \beta_1^2 + \beta_{13}^2 & 0 & \beta_{13}(\beta_{11} + \beta_3) \\ 0 & \beta_{22}^2 & 0 \\ \beta_{13}(\beta_{11} + \beta_3) & 0 & \beta_{33}^2 + \beta_{13}^2 \end{pmatrix} \tag{140}$$

and represents the diffusion matrix. It is easy to prove that if the off-diagonal terms are set to zero, this experiment reduces to that of three independent, one dimensional Ornstein-Uhlenbeck processes already discussed in [61]. The purpose is here the validatation of the three dimensional version of the Langevin solver and so, for sake of simplicity and without losing of generality, only the $x-$ and $z-$directions have been coupled.

A system of 10^4 particles has been initialised with three $\delta-$functions centred in different positions and its time evolution has been monitored through the mean and the variance of the distribution functions in the three directions. These are the measurable particle quantities that can be compared with the analytical counterpart. The discretise equation of motion (138) is used to advance the particles in velocity space with $\Delta t = 10^{-2}$ where the constants are fixed equal to $a = 0.5$ and $\beta_{11} = 1.\,,\ \beta_{22} = 2.\,,\ \beta_{33} = 3.\,,$ and $\beta_{13} = \beta_{31} = 1.5$. The observables of the numerical experiment in mesh-free space are the mean and variance which are determined according to

$$\tilde{m}_c^{(i)}(t) = \frac{1}{N}\sum_{p=1}^{N} C_p^{(i)}(t) \tag{141}$$

and

$$\left[\tilde{s}_c^{(i)}(t)\right]^2 = \frac{1}{N-1}\sum_{p=1}^{N}\left[C_p^{(i)}(t) - \tilde{m}_c^{(i)}(t)\right]^2\,, \tag{142}$$

respectively, where $C_p^{(i)}(t)$ denotes the actual velocity of the particles in the $i-$th direction. These quantities as well as their analytical counterparts (139) are recorded each 10 temporal cycles. The results for the mean value and the variance for the distribution functions in the three velocity directions are depicted in Figures 6.5 and 6.7, respectively, where the Euler

approximation (line with filled squares) and the exact solution (full line) is plotted. Obviously, the overall agreement of the numerical result with the analytical solution is very satifactory. The deviations between the Euler approach and the exact result seen for the mean value in Figure 6.5 can be "cured" by using, for instance, a second order weak scheme (see Fig. 6.6). We emphasise that this equilibrium state is reached approximately at $t = 10$ (see also Figure 6.7); afterward, the change of the shape is hardly visible in this representation. The improvement gained in the first moment is not so evident in the variance plot owing to the noise generated by the further random numbers needed for this scheme. To gain a further insight in the relaxation dynamics we plot in Fig. 6.8 the temporal evolution of the distribution function $f(c_x)$ on the velocity grid. As expected, the broadening of the distribution function is very rapid at early time. Another comparison between the numerical results of the Euler scheme (open circles) and the exact solution (full line) is seen in Fig. 6.9, where the particle distribution function on the velocity grid is plotted at time $t = 20$. Moreover, it is interesting to note that in this special case also the quantity $< c_x c_z >$ can be exactly evaluated and therefore compared to the numerical results. Figure 6.10 shows a very good agreement of the first and second order values with the analytical expression.

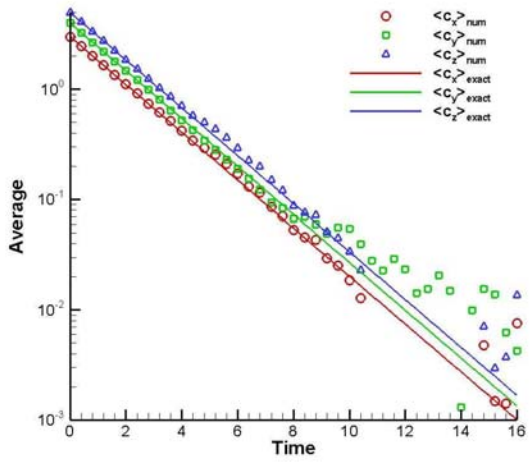

FIGURE 6.5. Temporal evolution of the mean value of the Ornstein-Uhlenbeck process. Full line: exact solution, symbols: Euler approximation

6.2.3. *Experiment 3: Convergence Analysis.* The results obtained in the previous experiment suggest a deeper investigation about the approximation characteristics of the two numerical schemes (116) and (136). For this purpose, a one dimensional stochastic process involving two different Wiener processes

$$dC(t) = \alpha C(t)dt + \beta_1 C(t)dW^1(t) + \beta_2 C(t)dW^2(t) \tag{143}$$

is considered, where $\alpha = -0.5$, $\beta_1 = 0.02$ and $\beta_2 = 0.03$. This very simple stochastic equation in the random variable $C(t)$ is solved on the time interval $t \in [0, 1]$ with initial value

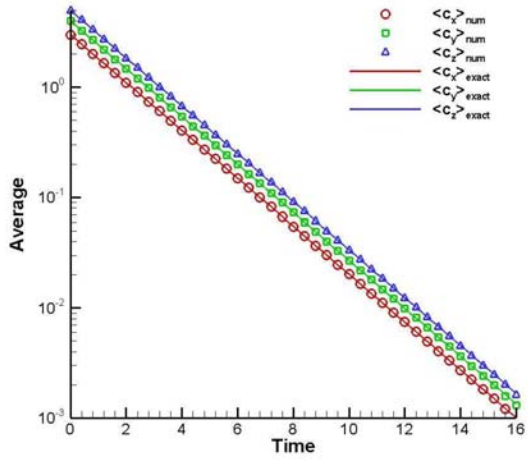

FIGURE 6.6. Second order evaluation of the mean value of the Ornstein-Uhlenbeck process. Full line: exact solution, symbols: numerical approximation

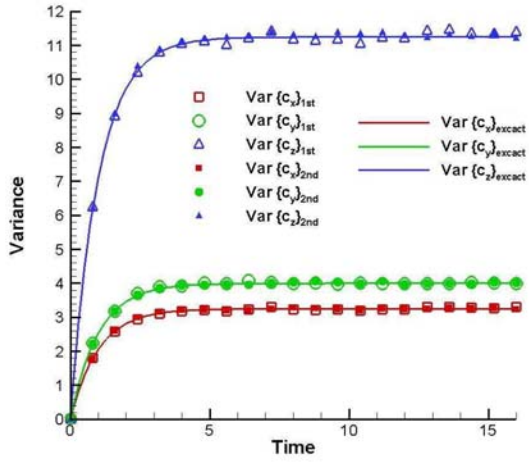

FIGURE 6.7. Comparison between the time-dependent variance obtained with a weak Euler (open symbols) and a 2nd order weak scheme (filled symbols) and the analytical result (full line)

$C(t_0) = 3.0$ and where W^1 and W^2 are the two independent Wiener process.
Due to the zero expectation property of the Itô integrals, an ordinary differential equation for the mean m of (143) is obtained:

$$m(t) = m(t_0)e^{\alpha(t-t_0)}. \tag{144}$$

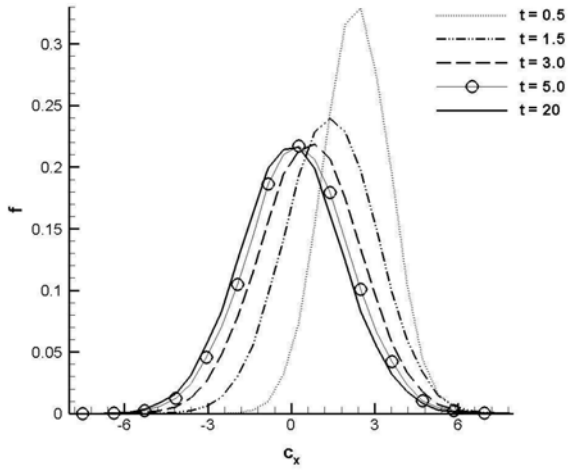

FIGURE 6.8. Temporal snapshots of the collisional relaxation of $f(c_x)$ in the three dimensional Ornstein-Uhlenbeck process

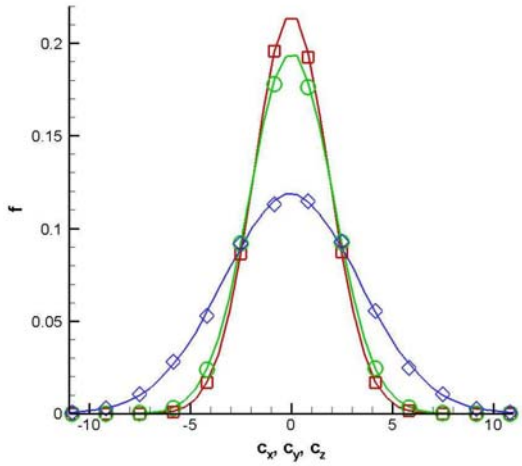

FIGURE 6.9. Comparison between the numerical (symbols) and analytical (full line) particle distribution functions recorded on the velocity grid at $t = 20$

Following [49], the experiment is organised in $M = 40$ batches of $N = 100$ trajectories each. Then, the mean error of the $j-$th batch is computed from

$$\hat{\mu_j} = \frac{1}{N} \sum_{k=1}^{n} C_{j,k}(T) - m(T) \tag{145}$$

where $C_{j,k}(T)$ represents the solution obtained with the weak schemes (116) and (136) at $t = T$ and $m(T)$ is determined from eq. (144). Obviously $\hat{\mu_j}$ can take both positive and

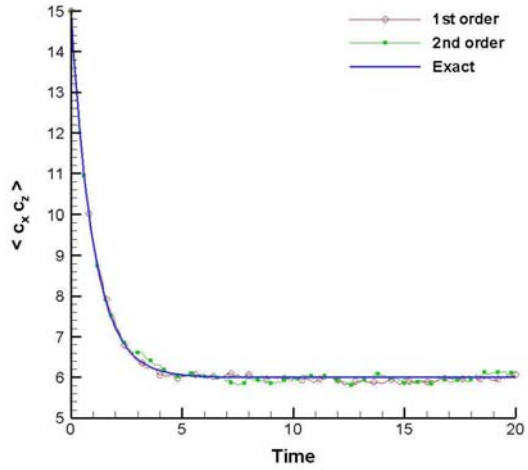

FIGURE 6.10. Temporal evolution of the cross moment $< c_x c_y >$ evaluated with a first order (circles) and a second (squares) weak scheme

negative values. The average over all batches

$$\hat{\mu} = \frac{1}{M} \sum_{j=1}^{M} \hat{\mu_j} \tag{146}$$

is evaluated for different discretisation $\Delta t = 2^{-n}$ of the considered time interval and plotted as a function of the discretisation exponent (see Fig. 6.11). From the slope of the curves

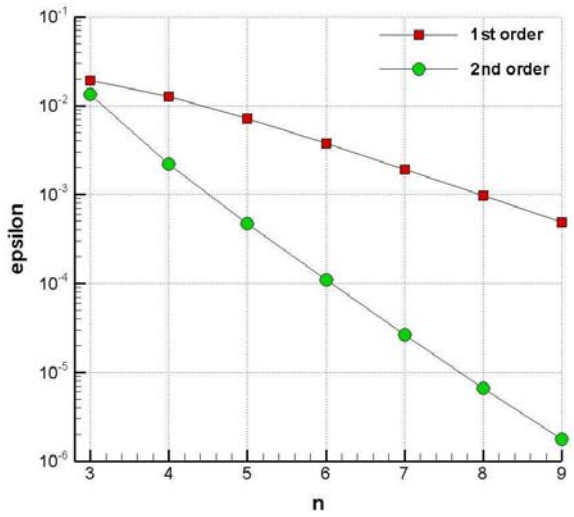

FIGURE 6.11. Error trend as function of the half-time exponent n for the first (square) and second (circles) order weak schemes

an experimental order of convergence of ~ 0.999 and ~ 2.541 for the first and second order

respectively, and therefore in good agreement with the designed orders of convergence.
This as well as the other results presented in this section convince us from the quality and reliability of the Langevin solver which is now used for self-consistent collision simulations.

6.3. **Intra-species Collisions Validation.** In order to perform an even more general investigation of intra-species collision, all the quantities have been treated as dimensionless. The reference sizes are the mass and charge of the electron and a density of 10^{18} m^{-3}. The thermal velocity is derived from a Maxwellian distribution function of electrons at a temperature of 10 eV. From these parameters one obtains that one time unit is equivalent to $1.78 \cdot 10^{-7}$ seconds.
The particles velocities are updated according to the scheme of equation (116) and the friction and diffusion forces are evaluated by means of eq. (54) and (55).

6.3.1. *Stationary Solution.* This numerical experiment is designed for the assessment of the applied numerical methods coded in the FP module. Moreover, diagnostic tools are introduced to get a better characterisation of the relaxation dynamics as well as to perform cross checks on known physical quantities.
This experiment starts considering the three dimensional normal distribution function $F(\vec{c}) = \prod_{i=1}^{3} f_i(c_i)$ (with $f_i(c_i) = \frac{1}{\sqrt{2\pi}\sigma_i} exp\{-\frac{c_i-\mu_i}{2\sigma_i^2}\}$ which is a solution of the FP equation [30].
The numerical experiment is initialised as follows: In the mesh-free velocity space, the initial velocities $c_p^{(i)}(t = 0)$ of the $N = 3 \cdot 10^5$ particles are independent identically distributed Gaussian random numbers (with mean zero and variance $\sigma^2 = 1.$). This procedure ensures that the initial velocity distribution of the particles (see Fig. 6.12) – which is the probability density function of the random numbers $c_p^{(i)}(t = 0)$ – is a Maxwellian [39] of the form

$$h(c, 0) = g_0(c) = \frac{2}{\sqrt{2\pi}} \frac{c^2}{\sigma^3} \exp\left(-\frac{c^2}{2\sigma^2}\right), \tag{147}$$

(see Fig. 6.13). Subsequently, the PIC cycle seen in Figure 5.1 is $3 \cdot 10^3$ times passed through, which is equivalent to a nondimensional simulation time of approximately 30 times unit. Throughout this computation the velocity grid which is needed for the Rosenbluth solver consists of $2^6 = 64$ grid points in each direction. Since the system is in an equilibrium configuration, the shape of the distribution functions as well as their moments are not expected to change during the overall simulation time. For this purpose, mean and variance values are recorded each 100 cycles and plotted respectively in Fig. 6.14 and 6.15. Despite some spurious oscillations around the equilibrium position, the mean behaviour can be considered satisfactory. The same cannot be said for the variance which increases almost linearly in time. This phenomenon, known in literature as artificial warming, is presumably due to the grid interfaces operations namely, interpolation and assignment procedures. The hypothesis that such a deviation from the stationary solution is attributable to the grid is confirmed by the fact that the numerical solution is improved by increasing the number of grid points, as clearly shown in Fig. 6.15. Raising N_G can be costy besides dangerous since it can generate

a very noisy distribution function which in turn results in wrong friction and diffusion forces. The renormalisation technique originally introduced by Lemons et al. [60] to cure instability problems arising in finite samples simulations is here revisited to provide global energy and momentum conservation. This simple and cheap operation (from a computational point of view)

$$\vec{v}_\alpha \rightarrow \vec{V}_\alpha = \vec{\mu} + \left(\vec{v}_\alpha - \vec{\mu}^{\,\prime}\right)\sqrt{\frac{(\sigma^2)}{(\sigma^2)^\prime}}\,; \quad \alpha = 1, \ldots, N_p \tag{148}$$

eliminates any instabilising fluctuations in the moments of f_e by linear transforming the particles velocities without changing the shape of the distributions so that their means and variances recover the desired values while the system evolves stochastically. Prime symbol indicate the values before collision while $\vec{\mu}$ and (σ^2) are the mean and variance afterwards. In fact, the mean values of the particle velocity in the $x-$, $y-$, and $z-$ direction and the global energy are conservation quantities which cannot change during time in a reservoir simulation. Starting from these considerations, at each time step, the energy of the whole system is given by the sum of the variances in the three directions and is not allowed to change,i.e.:

$$E(t) = E(t=0) = \sigma_x^2(t) + \sigma_y^2(t) + \sigma_z^2(t) = \text{const.}\,. \tag{149}$$

The numerical error is evaluated as:

$$err = E_0 - \sigma_x^2(t) + \sigma_y^2(t) + \sigma_z^2(t) \tag{150}$$

where $E_0 = E(t=0)$, and in the spirit of the equipartition principle is equally subdivided in the three directions. Now the prime $(\sigma^2)'$ in eq. (148) means actual value while (σ^2) indicates a "desired" value, that is:

$$\sigma^2(t_n) = (\sigma^2)'(t_n) - err/3\,. \tag{151}$$

The mean value represents a sort of group or stream velocity and in case of absence of external forces it also is not allowed to change. Despite the physical constrain, numerical error causes it to oscillate around its initial value, but the same logic can be applied if $\vec{\mu}$ is interpreted as:

$$\vec{\mu}(t_n) = (\vec{\mu}(t_n))'(t_n) - \vec{\mu}_0 \tag{152}$$

where $\vec{\mu}_0 = \vec{\mu}(t=0)$. The benefits are immediately evident from a first glance to Figs. 6.16 and 6.17. No unreal heating takes place now and the global energy is conserved – besides very small oscillations. This correction assures also that mean energy (temperature) and momentum are conserved during the simulation.

6.3.2. *Arbitrary Anisotropic Initial Distribution.*. A further numerical experiment of this session is tailored to study the collisional relaxation of an arbitrary anisotropic initial velocity distribution to its equilibrium from first principles. The shape of the initial velocity distributions (see Fig. 6.18) in the $i-$th direction of the velocity (in a cartesian frame of reference)

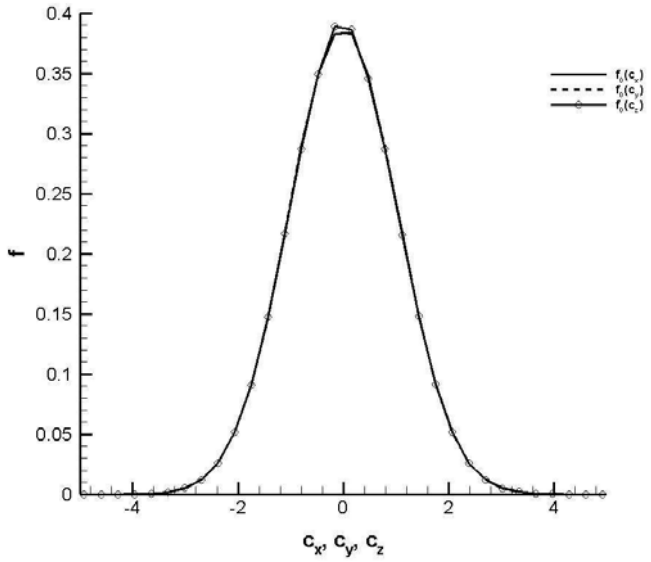

FIGURE 6.12. Initial velocity distribution function for c_x, c_y, c_z

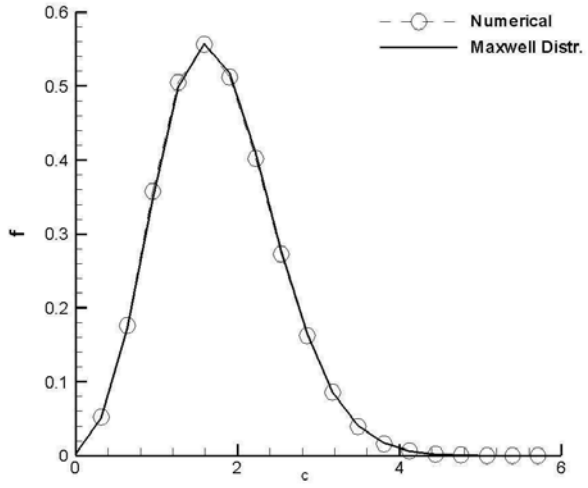

FIGURE 6.13. Initial distribution function for the modulus of the particles velocity and corresponding analytical curve

is given by

$$h(c^{(i)},0) = \begin{cases} \alpha^{(i)} \frac{c^{(i)}}{\tilde{v}^{(i)\,3}}, & \text{for } c^{(i)} \leq \tilde{v}^{(i)} \\ 0, & \text{for } c^{(i)} > \tilde{v}^{(i)} \end{cases}, \tag{153}$$

where $\tilde{v}^{(i)}$ and $\alpha^{(i)}$ are normalisation constants set differently for each directions. To establish such a velocity distribution, the initial velocities $c_p^{(i)}(t_0)$ of the $N_p = 3{\cdot}10^5$ particles are chosen

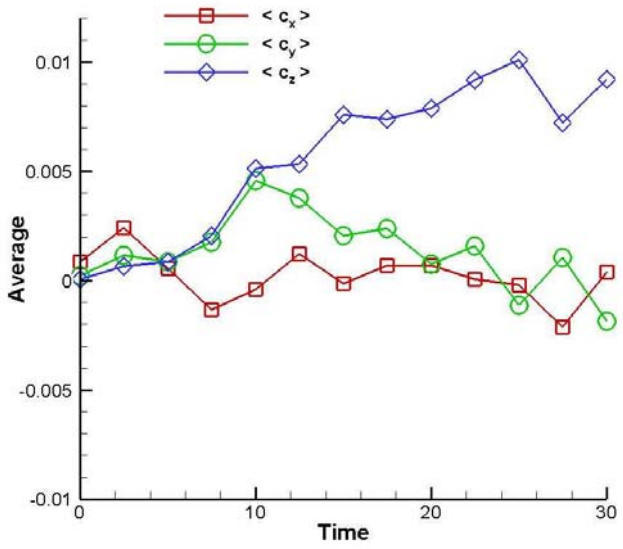

FIGURE 6.14. Mean time evolution

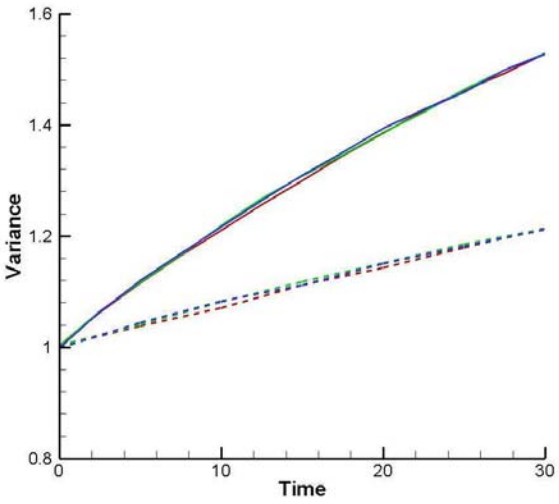

FIGURE 6.15. Variances evolution time for the three components of the velocities evaluated on a 64 points grid (continuous lines) and on a 128 (dashed lines) one

according to $c_p^{(i)}(t_0) = \tilde{v}\, U_p^{1/3}$ where the $U_p \in [0, 1]$ are uniform random numbers between 0 and 1. The first measurement of interest is the temporal evolution of the $H_e(t)$-function [35, 37] applied in the form

$$H_\alpha(\mathbf{x}, t) = - < \ln(f_\alpha) >_\alpha \tag{154}$$

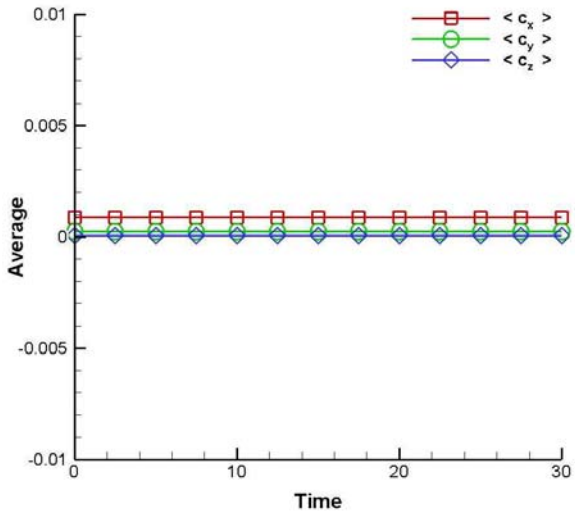

FIGURE 6.16. Mean time behaviour when correction is applied

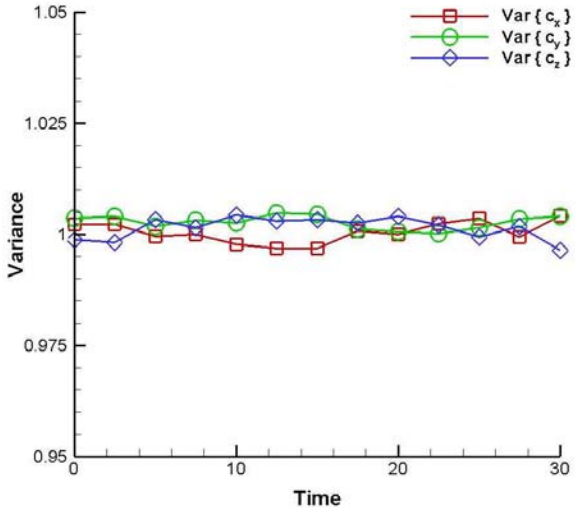

FIGURE 6.17. Variances evolution time recorded on a 64 grid points when renormalisation is active

which can be ascribed to Boltzmann (1872). This quantity can be used to show that the entropy of a closed system can only increase in the course of time till it approaches a limit for very large times (H-theorem) [62, 37, 9]. It is well-known that the FP operator acting on f_e is dissipative in the sense of satisfying Boltzmann's H-theorem [63]. In other words a system of charged particles in non-equilibrium condition evolves in the course of time to its equilibrium conditions and relaxes to a Maxwellian shaped distribution with positive entropy production. In this respect, this quantity provides an appropriate measure of the extent to which the

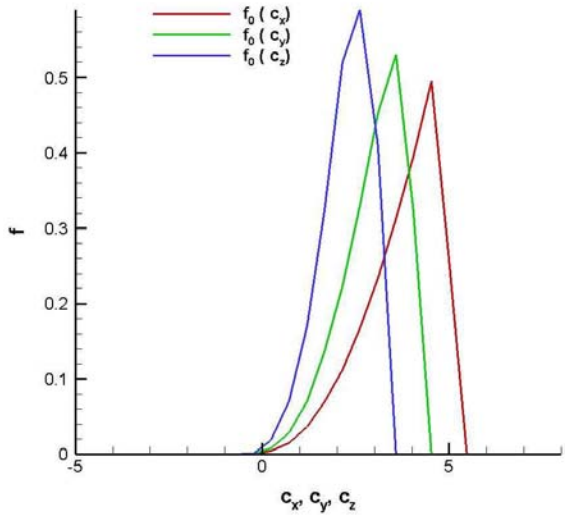

FIGURE 6.18. "Exotic" initialisation with three different parabola shaped distribution functions

conditions of a system deviates from that corresponding to equilibrium. It can further be shown [35] that when the equilibrium is reached, collisions are not responsible anymore for the rate of change of $H(\mathbf{x}, t)$. As shown in Figure 6.19, in this experiment the H-function stays approximately constant – besides small numerical oscillations – and slightly around the stationary value, remarking the fact that the whole code can hold a steady-state solution quite well and confirming a very good synergy of the blocks previously considered. From Figure 6.19

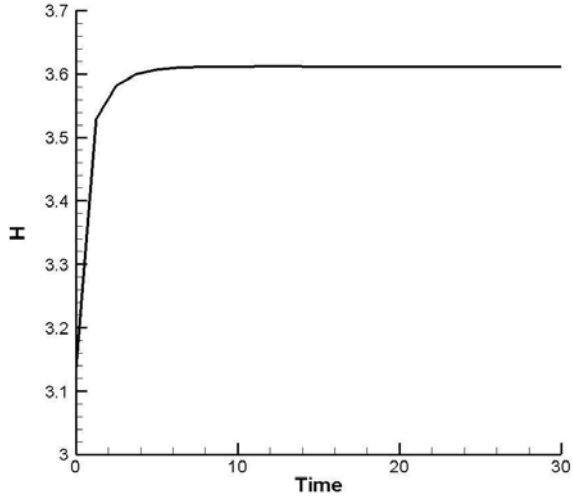

FIGURE 6.19. Temporal evolution of the H_e-function for the initial velocity distribution defined by relation (153)

we conclude that the equilibrium velocity distribution should be achieved after approximately 1000 temporal cycles when we expect to find Gaussian shaped distribution functions in all the directions as confirmed by Fig. 6.20. As customary in this work, numerical results which

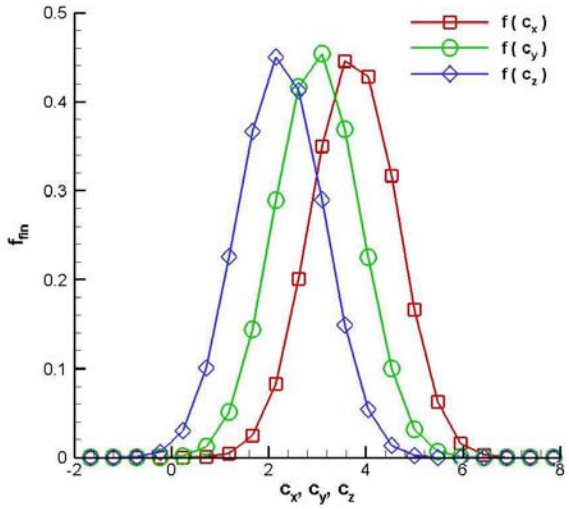

FIGURE 6.20. Final configuration of the particle velocity distribution functions

are measured from particle quantities, namely mean and variance, are shown in Fig. 6.21 and 6.22 where the correction (148) is now applied. The mean values of all velocity components remain constant since there is no external force to cause a stream motion of the particles; on the other side the diffusion process provides, by means of the friction and diffusion forces, mechanisms that allow energy internal exchanges such that the system reaches the thermal equilibrium in agreement with the equipartition principle.

6.3.3. *High Energy Tail Thermalisation.* One characteristic aspect of the numerical simulation of the thermalisation process operated is the underestimation of the high energy tail of the velocity distribution function as evidenced in [61] and references therein. To demonstrate that this phenomenon persists also in a non-isotropic simulation, the three particle velocities have been initialised with uniform distribution functions centred in zero (see Fig. 6.23). As expected, at the end of the simulation the speed c is Maxwellian distributed, but the plot of $f(c)/c^2$, where $c = \sqrt{c_x^2 + c_y^2 + c_z^2}$, in logarithmic scale reveals that the tail of this distribution is not so close to the "thermalized" shape while the core agrees already very well exact solution.

6.4. **Characteristic Time Scales.** One interesting and practicle problem is to know the time in which collisions can produce large alteration in the original velocity distribution; for example how rapidly an initial anisotropic distribution function relaxes to a Maxwellian because of collisions. The time required for the whole process to take place is known as "relaxation time" and it is clearly a not defined one [64]. One way to obtain estimations of

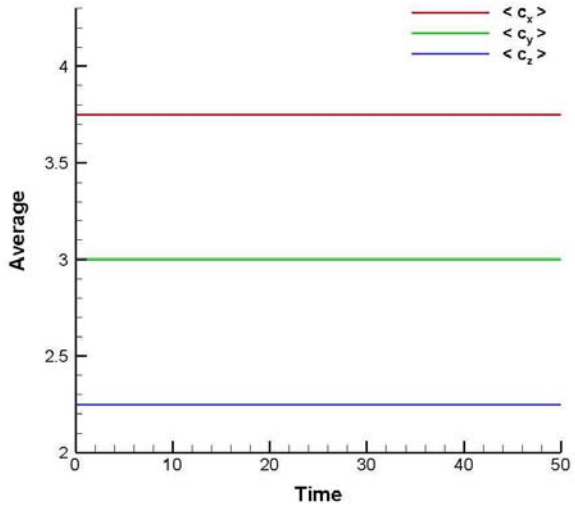

FIGURE 6.21. Constant behaviour of the mean values of the three distribution functions in absence of external forces

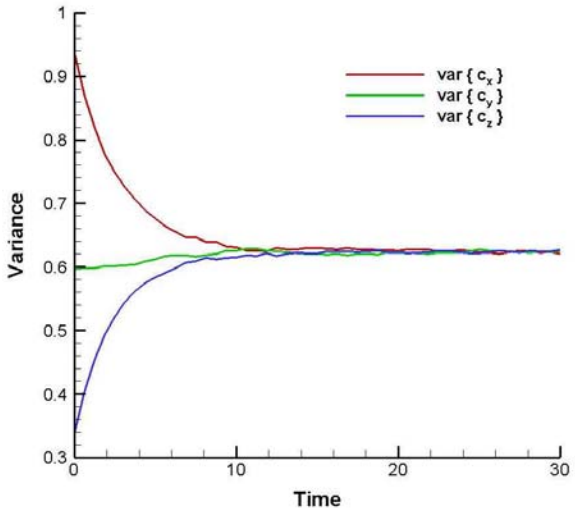

FIGURE 6.22. Temporal change of the three variances for the "three parabolas" experiment. Final fulfilment of the equipartition principle

such parameter is to consider the scattering of one particle and try to get information about the time scaling of a distribution of particles with the same initial velocity conditions. This classical method known as test-particle approach was developed by Chandrasekhar [36] and Spitzer [64], and a variation can be found, for instance, in Montgomery & Tidman [30].
One relaxation time investigated by the test-particle method is the so-called slowing down

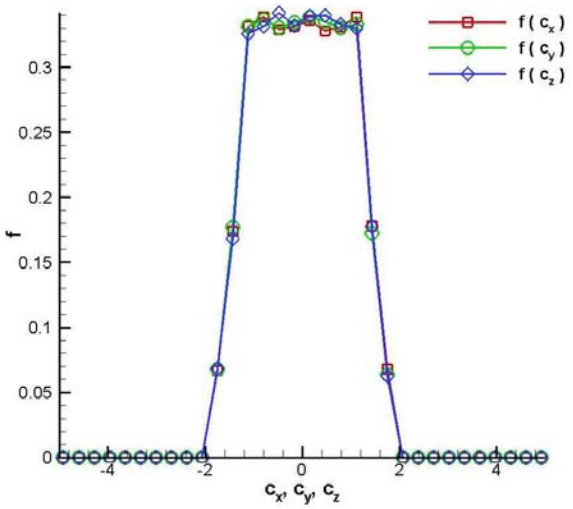

FIGURE 6.23. Initial configuration with three uniform distribution functions having variances three

time. This time scale gives rate at which collisions decrease the mean velocity of the test particles. These particles are initially "injected" into the plasma as a monochromatic "beam" which has only a constant c_z velocity component and are "traced" up to the time where they are stopped. Note that it can be shown [30] that the slowing down time is only related to the friction force coefficients of the FP equation. Another relaxation time of interest in the test-particle approach is the so-called deflection time, which may be considered as the typical time scale for an initially anisotropic distribution becomes isotropic [31]. Per construction this time scale is associated with the transverse velocity components of the test particles which are zero initially and is a measure of gradual deflection of the test particles by 90 degrees caused by the cumulative effects of collisions. Simple considerations reveal that the rate of increase of the transversal velocities is only due to the diffusion term of the FP equation [30]. For the parameters used below one obtains for the slowing down and deflection time the values $\tau_{slo} \approx 62.25$ and $\tau_{def} \approx 130.3$, respectively.

In the context of the present work we intend to study the self-consistent dynamical evolution of the velocity distribution, where both friction and diffusion force are similarly important. Clearly, to switch off one of the dynamical aspects seems to be ideal but would contradict our self-consistent approach. In order to filter out characteristic times required by a whatever distribution function to reach an equilibrium state because of collisions we propose the following proceeding. The particles in the numerical experiments are subdivided in two groups: The first one consists of the background (abbreviated by BG) particles (constant number $N_{BG} = 3 \cdot 10^5$) which are Maxwellian distributed (that is Gaussian distributed in each velocity component; $\mu_{BG} = 0.$, $\sigma^2_{BG} = 1.$) initially, and the second group is the beam particles (labelled as b). In all numerical experiments discussed below, the latter group represent an

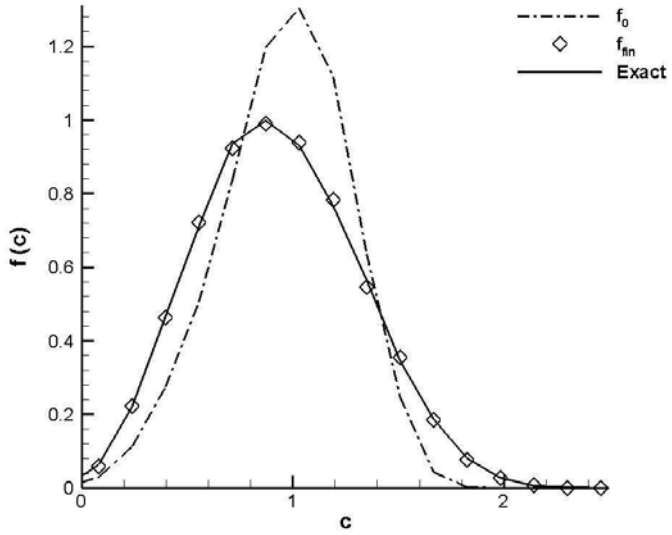

FIGURE 6.24. Initial (dashed-dotted line) and final (open symbols) speed distribution and compare with the exact (full line) solution for the time t=20

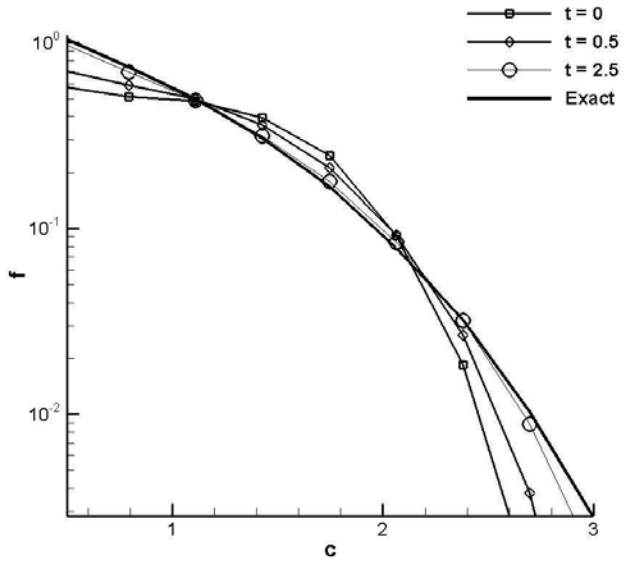

FIGURE 6.25. Temporal snapshots of $f(c)/c^2$ in logarithmic scale. Due to the scarce population of the high energy tail, it takes more time to be close to the exact solution

ideal monochromatic beam that hits initially the background particles with velocity only in the z-direction $\left(c_z^{(b)}(t=0)=5\right)$. To get an intuition of the complex non-linear dynamics

resulting from the self-consistent computations, we will compare the simulations with a reference experiment, where the Maxwellian distributed BG-particles are not affected by the beam particles. In this sense the distribution function changes only because of the beam particles, which are advanced according to (82), where the non-linear velocity-dependent friction force and diffusion coefficients are obtained exactly by the background characteristics. In fact, this experiment can be considered as an interface between the pure test-particle approach, where the coefficients are held constant for all the particles all the time (namely, at the initial values), and a real simulation. Also in the style of the test-particle approach, we use the mean value $< c_z >$ and the "transversal" variance σ_y^2 of the beam particles as measurable quantities which are recorded as function of time and seen in Figures 6.26 and 6.27 as full lines. Moreover, in these Figures the results of two self-consistent simulations ($3 \cdot 10^3$ cycles with $\Delta t = 5 \cdot 10^{-2}$) are depicted, where the beam to background particle ratios (pr) are fixed to pr=1/50 (lines with filled circles) and pr=1/10 (lines with open squares). We remark that in both self-consistent simulations the global velocity distribution functions established by the beam and background particles are highly non-Gaussian up to $t \leq\sim 35$ (see Fig. 6.28). In the following we mainly restrict the discussion to the reference experiment and the self-consistent pr= 1/50 simulation.
In order to get better insight of relaxation dynamics we introduce also the beam particle averaged z-component of the friction force

$$\langle F_z(t) \rangle = \frac{1}{N_b} \sum_{i=1}^{N_b} F_z(\vec{c}_i, t) \tag{155}$$

and the "velocity-normalised" yy-component of the diffusion tensor given by

$$\left\langle \frac{D_{22}}{|\vec{c}|}(t) \right\rangle = \frac{1}{N_b} \sum_{i=1}^{N_b} \frac{D_{22}(\vec{c}_i, t)}{|\vec{c}_i(t)|} \, , \tag{156}$$

where N_b is the number of beam particles. The temporal evolution of the friction $\langle F_z(t) \rangle$ and diffusion $\left\langle \frac{D_{22}}{|\vec{c}|}(t) \right\rangle$ coefficients obtained from the reference (full line) and the pr= 1/50 (line with filled circles) simulation are depicted in Figure 6.30 and 6.31. By fitting these and the previous curves we tried to extract the time constants τ that characterise the phenomenon and summarised them in the Tables 1 till 4.

At first sight we recognise that mean values as well the variances of the three experiments (see Figs. 6.27 and 6.26) show approximately the same basic features which appear to be a hint that the underlying relaxation dynamics is essentially similar. However, the relaxation dynamics of the self-consistent experiments are much faster than the reference simulation. This observation seemed to be a direct consequence of the non-Maxwellian global velocity distribution. Note, that the "heating" of the beam particles (Fig. 6.27)– which may be considered as a measure of the rapidly increasing asymmetry of the beam particles distribution function (see Fig 6.29) – is less pronounced in the self-consistent experiments which seemed to be a consequence of the non-Maxwellian global velocity distribution. The "decay" of these maxima seen in Figure 6.27 can be associated with further characteristic time scales. It is not

$< c_z(t) >$	$\tau_c^{1/50}$	τ_c^{ref}
$t \in [0, 15]$	slow scale dynamics	slow scale dynamics
$t \in [15, 30]$	fast scale dynamics	fast scale dynamics
$t \in [28, 50]$	≈ 12	–
$t \in [30, 90]$	–	≈ 16

TABLE 1. Time constants τ_c for $< c_z >$

$< F_z(t) >$	$\tau_F^{1/50}$	τ_F^{ref}
$t \in [0, \sim 25]$	transient dynamics	–
$t \in [0, \sim 40]$	–	transient dynamics
$t \in [28, 70]$	≈ 12	–
$t \in [40, 80]$	–	≈ 16

TABLE 2. Time constants τ_F for $< F_z >$

surprising that the time constants for the mean value and the variance in perpendicular direction are different. Actually, from the study of the Ornstein-Uhlenbeck process – the simplest linear diffusion process – it is known that the time constant for the variance is larger than the one for the first moment [61]. Furthermore, we observe that the global velocity distribution of the self-consistent pr= 1/50 simulation is now close to the background Maxwellian of the reference experiment for times $t \geq\sim 35$. Consequently, it seems to be possible that the (fast) initial non-Maxwellian driven relaxation dynamics turn into the Maxwellian dominated equilibrium dynamics. It is obvious from Figure 6.30, that the non-Maxwellian global velocity distribution leaves its mark especially during the first ~ 30 time units. We recognise there that the shape of the friction coefficient of the pr= 1/50 experiment is different from that one of the reference simulation and, furthermore, that the self-consistent relaxation dynamics is much faster than in the non self-consistent case. It is interesting that these characteristic initial scales are not seen in the temporal evolution of the diffusion coefficients plotted in Figure 6.31. On closer inspection of the curves plotted in Figures 6.30 and 6.31, we recognise points of inflection located roughly in the intervals $\sim 20 \leq t \leq\sim 30$ and $\sim 30 \leq t \leq\sim 40$ for the pr= 1/50 and non self-consistent simulation, respectively. On the contrary we have found a very good agreement between friction and mean value time constants. At first, it is astonishing that the friction time constant of the self-consistent experiment is also visible in the transversal diffusion coefficient. Under the working hypothesis that the relaxation dynamics turns into a Maxwellian dynamics for $t \geq\sim 35$, we expect a behaviour similar to the reference experiment: The onset of the friction and diffusion should start approximately at the same time and the rise of these coefficients should occur at the same characteristic time constant for the pr= 1/50 simulation, that is $\tau_F^{1/50} \approx \tau_D^{1/50}$.

6.5. **Inter-Species Collisions.** Due to the fact that the velocity of the electrons $c = |\vec{c}|$ is much larger than that of the ions (labelled from now on as "X") $w_X = |\vec{w_X}|$ and, furthermore,

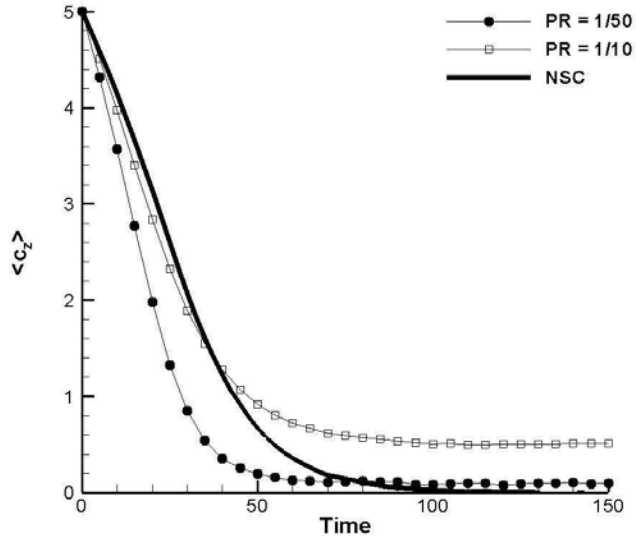

FIGURE 6.26. Velocity mean value of the beam particles $< c_z^{(b)}(t) >$ as a function of time for the self-consistent simulations with particle ratios pr=1/50 (line with filled circles) and pr=1/10 (line with open squares) and the non self-consistent reference experiment (full line)

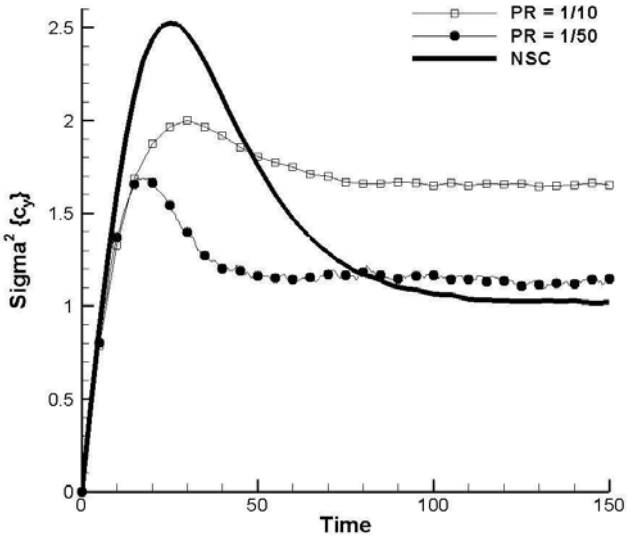

FIGURE 6.27. Temporal evolution of the transversal variance $\sigma_y^2(t)$. Full line: reference simulation; line with filled circles: pr=1/50 and line with open squares: pr=1/10 experiment

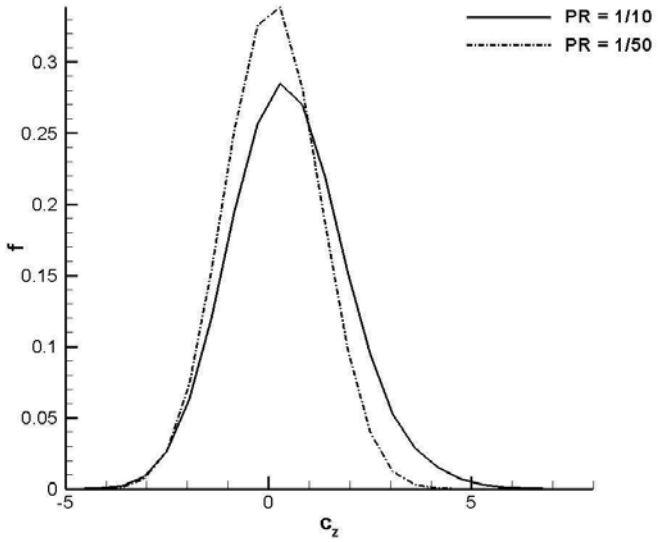

FIGURE 6.28. $f_{global}^{PR=1/50}$ (continuous line) and $f_{global}^{PR=1/10}$ (dash-dotted line)recorded at $t = 30$

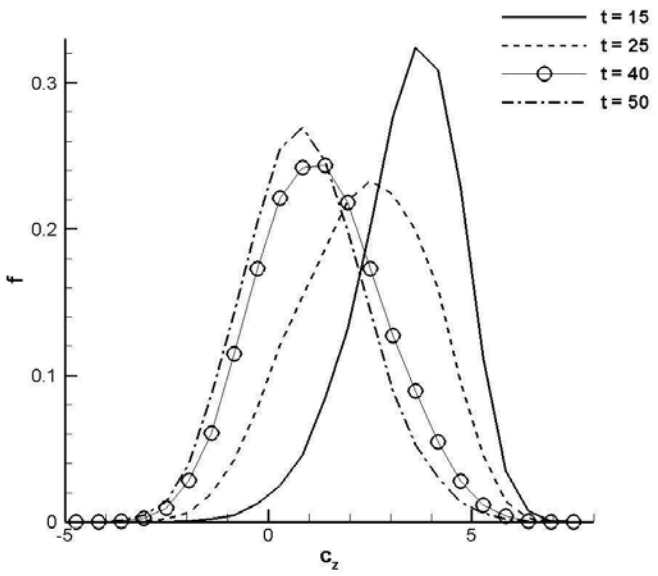

FIGURE 6.29. Beam particles distribution functions for PR = 1/50 recorded at time $t = 15, 25, 40, 50$

to the smallness of their mass ratio ($m_e/m_X \ll 1$) the mathematics of this collisional event can be drastically simplified. Clearly, this means, that the electrons are scattered off by (nearly) infinitely massive ions with velocity $w_X \approx 0$, where the energy coupling is quite weak (see Sec. 4.6). In the following, the situation $\overline{v}_X^2/c^2 \ll 1$ and $V_p^X = 0$ (see also [40]) is

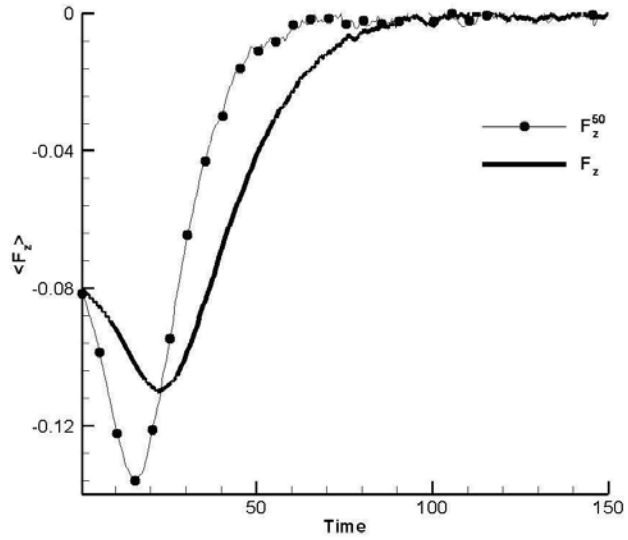

FIGURE 6.30. Temporal evolution of the z-component of the averaged friction force obtained from the reference (full line) and pr=1/50 (line with filled circles) experiment

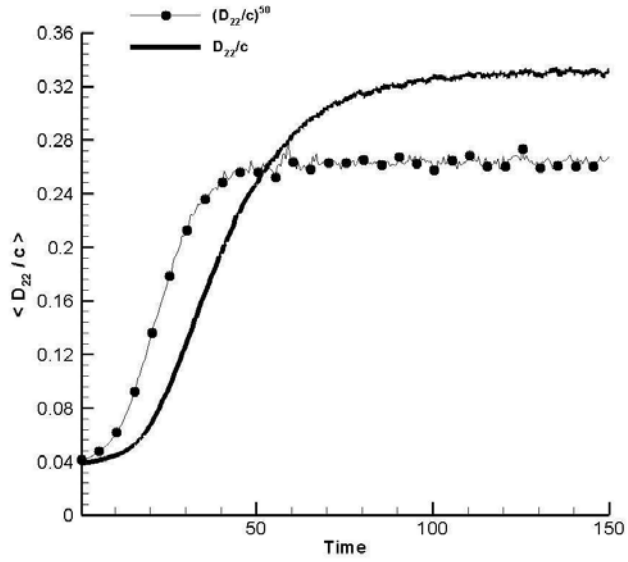

FIGURE 6.31. The normalised averaged diffusion coefficient as a function of time computed with the reference (full line) and the self-consistent pr=1/50 (line with filled circles) simulation

$\sigma_y^2(t)$	$\tau_\sigma^{1/50}$	τ_σ^{ref}
$t \in [0,\, 20]$	steep rise up to the max	–
$t \in [0,\, 30]$	–	steep rise up to the max
$t \in [22,\, 40]$	≈ 58	–
$t \in [35,\, 70]$	–	≈ 58

TABLE 3. Time constants τ_σ for $\sigma_y^2(t)$

$\left\langle \frac{D_{22}}{\vert\vec{c}\vert}(t) \right\rangle$	$\tau_D^{1/50}$	τ_D^{ref}
$t \in [0,\, \sim 25]$	transient dynamics	–
$t \in [0,\, 40]$	–	transient dynamics
$t \in [22,\, 80]$	≈ 10	–
$t \in [40,\, 120]$	–	≈ 19

TABLE 4. Time constants τ_D for $\left\langle \frac{D_{22}}{\vert\vec{c}\vert}(t) \right\rangle$

examined; a first analysis reveals that in this case $\mathbb{D}^{(X)}$ represents the transversal diffusion since $\hat{\mathbf{c}}^T\, \mathbb{D}^{X)} = 0$. Second, due to the special properties of the matrix

$$\mathbb{H} = \mathbb{I} - \hat{\mathbf{c}}\, \hat{\mathbf{c}}^{\,T} \tag{157}$$

namely, $\mathbb{H}^T = \mathbb{H}$ and $\mathbb{H}^T\, \mathbb{H} = \mathbb{H}$ the derived tensor $\mathbb{B}^{(e\,X)}$ can be written as

$$\mathbb{B}^{(X)} = \alpha\, c\, \mathbb{H} \tag{158}$$

with the abbreviation $\alpha^2 = \Gamma_P^{(e\,X)}\, n_X\ c^{-3}$. Assuming that the energy of the electrons is conserved exactly, i.e. $c = |\,\mathbf{c}\,| =$ constant, the SDE (82) takes the form

$$d\hat{\mathbf{C}}(t) = -\alpha^2\, \hat{\mathbf{C}}(t)\, dt + \alpha\, \mathbb{H}\, d\vec{W}(t)\ , \tag{159}$$

where $\hat{\mathbf{C}}$ is identified with $\hat{\mathbf{c}}$. Some preliminary observations are mandatory: This equation is a SDE for the sines and cosines of the polar and azimuthal angles. Since the matrix $\mathbb{H}$ is not linear in $\hat{\mathbf{c}}$ an exact solution of equation (159) is not expected. However, using the zero expectation property of the Itô integral and the Itô formula it is possible to find ordinary differential equations for both the mean and second moment. The solution of these equation are directly given by

$$M_i(t) = \mathrm{e}^{-\alpha^2\,(t-t_0)}\, M_i(t_0) \tag{160}$$

and

$$P_{ij}(t) = 1/3\, \delta_{ij} + \Big[P_{ij}(t_0) - 1/3\, \delta_{ij}\Big]\, \mathrm{e}^{-3\,\alpha^2\,(t-t_0)}\ , \tag{161}$$

where δ_{ij} denotes the Kronecker symbol, $M_i(t)$ and $P_{ij}(t)$, $i,\, j = 1, 2, 3$, are the elements of the expectation values $\mathcal{E}\Big\{\hat{\mathbf{C}}\Big\}$ and $\mathcal{E}\Big\{\hat{\mathbf{C}}\, \hat{\mathbf{C}}^T\Big\}$, respectively, and t_0 is the initial time. Note,

that the higher the electron velocity the slower the final moments are reached. The evaluation of the forces according to (47) and (48) is not self-consistent, i.e. the ions will not be affected by the impinging of the electrons resulting only in a change of direction for the electron velocity. This means in turn that the cumulative effects of impacts cannot thermalize the electrons because they cannot change their velocity but only their direction. It has been already remarked that for scattering of electrons off infinitely massive ions electron energy must be conserved exactly in each collision. Actually multiplying eq. (159) by $\hat{C}^{n\,T}$ on the left-hand side one obtains that

$$\hat{C}^{n\,T}\left[\hat{C}^{n+1} - \hat{C}^{n}\right] = -\alpha^2\,\Delta t \tag{162}$$

i.e., because of the friction $\left|\,\mathbf{c}^{n+1}\,\right| \neq |\,\mathbf{c}^{n}\,|$. This is a direct consequence of the approximations (45) and (3.30) which exclude any diffusion in the direction parallel to the velocity vector. Inspired by [40], a remedy is proposed here to overcome this inaccuracy. Since the second term on the rhs of eq. (159) is responsible for the randomisation of the directions, the friction force is dropped and $\hat{C}^{n+1}$ is evaluated as:

$$\hat{C}^{n+1} = \hat{C}^{n} + \alpha\,\mathbb{H}\,\vec{\eta}\,. \tag{163}$$

where the components of $\vec{\eta}$ are Gaussian random numbers. With the eigenvector (or cosine directors) matrix of $\mathbb{H}$ given by

$$\mathbb{P} = \begin{pmatrix} \hat{C}_1 & -\beta\,\hat{C}_2 & -\beta\,\hat{C}_1\,\hat{C}_3 \\ \hat{C}_2 & \beta\,\hat{C}_1 & -\beta\,\hat{C}_2\,\hat{C}_3 \\ \hat{C}_3 & 0 & \beta^{-1} \end{pmatrix},$$

where $\beta = 1/\sqrt{\hat{C}_1^{\,2} + \hat{C}_2^{\,2}}$ equation (163) can be rewritten according to

$$\hat{C}^{n+1} = \hat{C}^{n} + \alpha\,\hat{b}^{n}\,. \tag{164}$$

with $\hat{b}^{n} = \mathbb{P}\left(\nu_2\mathbf{e}_1 + \nu_3\mathbf{e}_3\right)$ where ν_2 and ν_3 are obtained from and $\vec{\nu} = \mathbb{P}^T\,\vec{\eta}$. In fact, $a\hat{b}^{n}$ represents the transversal component to the direction $\hat{C}$ since $\hat{C}^{n\,T}\,\hat{b}^{n} = 0$. This observation is illustrated in Fig 6.32, where $\hat{C}^{n}$ is forced to be reduced by a factor $1+\delta$. Finally, solving the equation

$$\hat{C}^{n+1} = (1+\delta)\,\hat{C}^{n} + \alpha\hat{b}^{n}\,.$$

for δ with the requirements that the kinetic energy is exactly conserved one gets

$$\delta = -\frac{\alpha^2}{2}(\nu_2^2 + \nu_3^2) \tag{165}$$

neglecting terms in δ^2.

The equations (160) and (161) represent a natural benchmark for the inter-species collision case: a beam of electrons entering the ions reservoir with $\vec{C}(t_0) \equiv (3,0,0)$ is considered and the event dynamics is monitored through the distribution functions and its moments. Picture 6.33 plots the mean value of the speed with respect to time for the said initial conditions. As one can see, the result is dramatic if no correction is applied. Moreover a closer inspection in the variances plot (see fig. 6.34) reveals the onset of finite samples instability observed in

[60]. By enforcing the particle velocities to fulfil energy conservation in each single collision eliminates the instability problem. The residual – only numerical – error can be totally removed by means of the renormalisation technique (cf. eq. 148) as demonstrated in fig. 6.35 (note the ordinate scale).
Some interesting considerations on the physical process can be extracted from the time development of the means and the variances in the three velocity directions: As reported in Fig. 6.36 and Fig. 6.37, the electrons "loose" completely their initial drift velocity and this initial kinetic energy is transformed in thermal (internal) energy which is re-distributed in each direction again according to the equipartition principle. This phenomenon is due to the approximation of infinite ion mass and is not observed in the case of intra-species collisions. The variances in figure 6.37 show that the $x-$ component of the velocity has a slower dynamics with respect to y and z due to the initial non-zero group velocity which represents a sort of inertia, a fact noticeable in eq. (161). Probably the most interesting features are drawn from the shape of the distribution functions recorded at time $t = 200$ (see Fig. 6.38), that is when a steady-state is reached: unlike the (e-e) case in which the velocities were Gaussian distributed around their initial mean value, here they are equally distributed around the zero mean value.

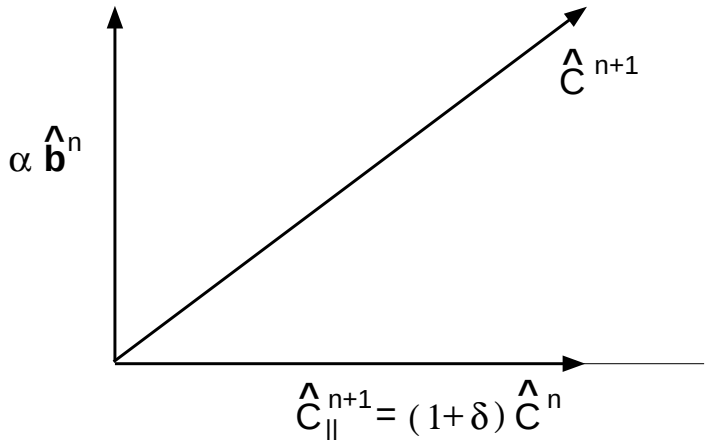

FIGURE 6.32. $\hat{C}^n$ and $\hat{C}^{n+1}$ as appear in a rotated system of reference with an axe parallel to $\hat{C}^n$. The transversal component is randomised by the diffusion force, while the parallel one is forced to fulfil energy conservation

6.6. **Coupled Calculations.** The very good results obtained in the previous simulations for both physical processes (intra- and inter-species collisions) separately, suggests to run the two routines together for a more realistic simulation of plasma collisions. As in the last section, the ions are thought to be immobile with respect to the faster and lighter electrons. The velocity of the latter are initialised with three Gaussian with different variances, respectively, $\sigma_x^2(t_0) = 1.0$, $\sigma_y^2(t_0) = 2.25$ and $\sigma_z^2(t_0) = 4.0$; as shown in Fig. 6.39 the electron impact the ion reservoir with an additional stream velocity $c_x(t_0) = 3.0$ in the $x-$ direction. For a better understanding of the coupled simulation, we first perform a numerical experiment with the

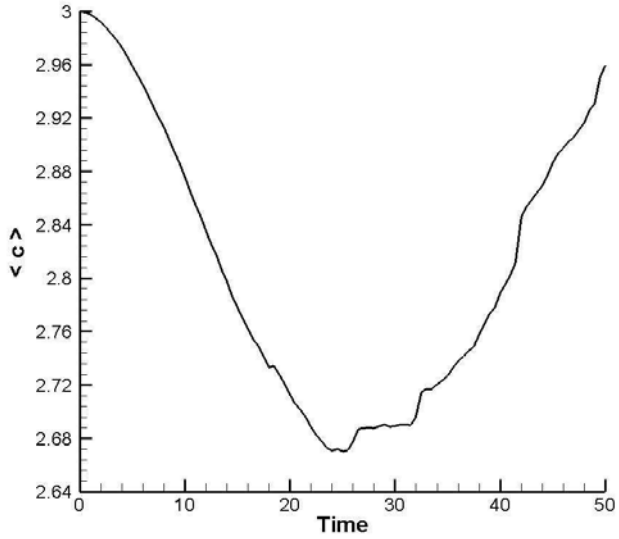

FIGURE 6.33. Mean speed with respect to time when local energy conservation is ignored. The unusual behaviour indicates the onset of instability phenomena

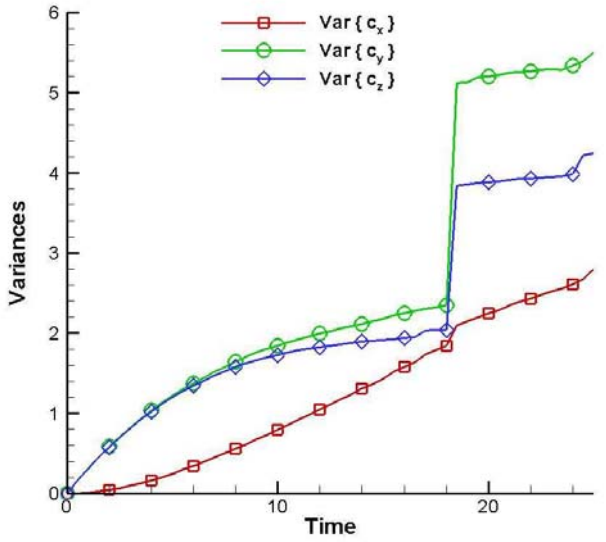

FIGURE 6.34. Variances instable behaviour due to finite sample calculations

described initial data, where the inter-species collisions were switched off. The result of this computation is depicted in Fig. 6.40. Obviously, the variances arrive after ~ 80 time units the equilibrium value $1/3\left[\sigma_x^2(t_0)+\sigma_y^2(t_0)+\sigma_z^2(t_0)\right] \approx 2.4$ while the mean value of c_x stays

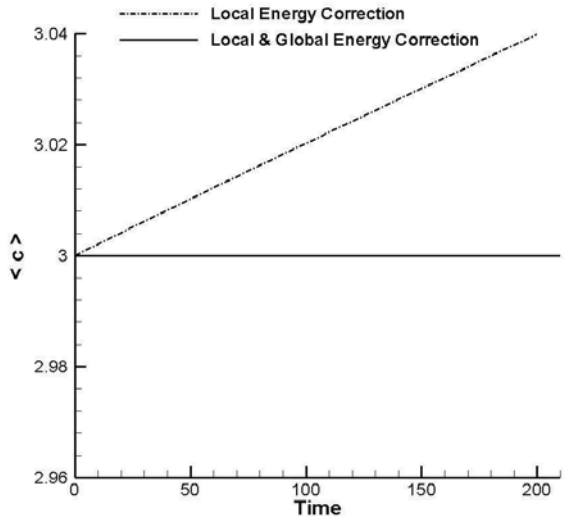

FIGURE 6.35. The local conservation energy (dashed-dotted line) guarantees a stable behaviour of the speed while the local energy conservation together with the (full line) renormalisation eliminates any residual numerical error

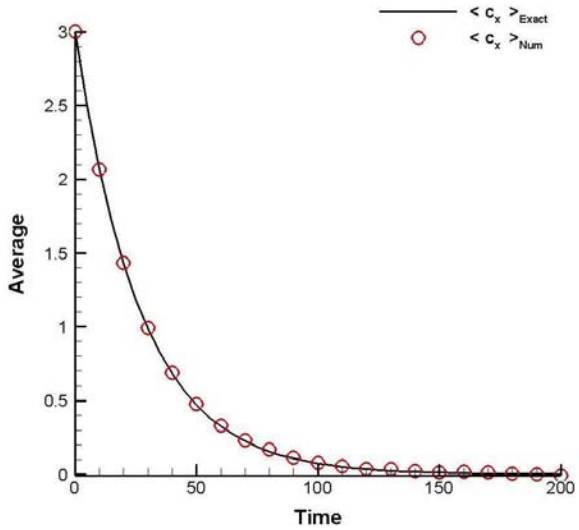

FIGURE 6.36. Mean value decay (symbols) for the $x-$ direction of the velocity in the (e-X) case and comparison with the exact solution (full line)

constant the initial velocity $c_x(t_0) = 3.0$ since no mechanism is available to convert the initial kinetic energy into the thermal internal energy; i.e to turn "coherent flow" into "disordered motion". The result of the coupled intra-inter-species simulation is seen in Fig. 6.41. In contrast to the previous experiment, the inter-species collision part provides a device which re-distributes the initial velocity uniformly in each direction resulting in the "decay" of the

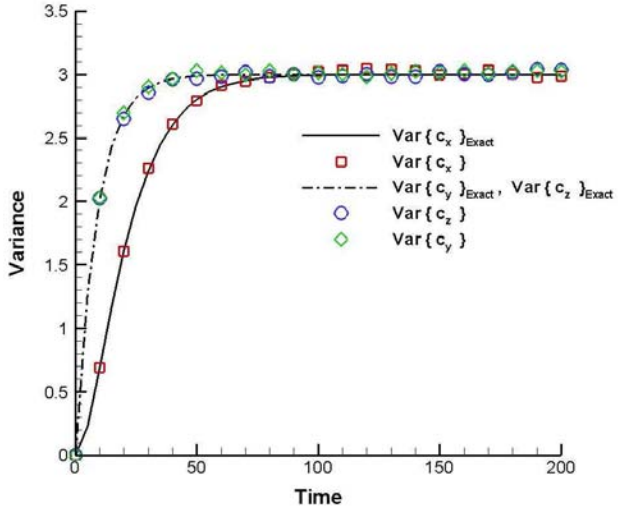

FIGURE 6.37. Variances time values (symbols) and comparison with the exact curves (full lines)

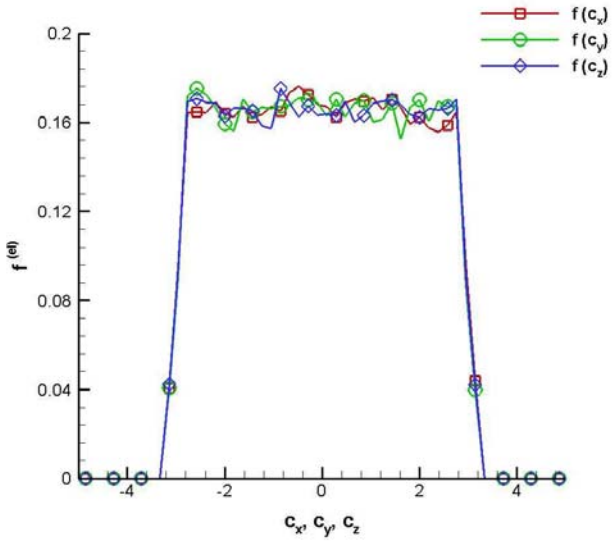

FIGURE 6.38. Final, equiprobable configuration of the distribution functions

mean velocity while the variances (thermal energy) are to reach a common value (see also Figs. 6.36 and 6.37). Consequently, in the coupled numerical experiment the initial kinetic energy is transformed in thermal energy (due to inter-species interaction) and it is clear from Fig. 6.41 that in this case the distribution in each direction will posses a value which is one third of the sum of that achieved for the intra-species case for the same initial condition (see Fig. 6.40) plus one third of the square of the initial flow velocity. Moreover, it is obvious from Fig. 6.41 that the coupled calculation is slower than the two independent processes seen in

the Figs. 6.37 and 6.40. This observation may be traced back to the fact that the parameter α^2 in eq. (159) is no longer a constant (as it is assumed there) during the simulation. In fact, a comparison of the dashed curve in Fig. 6.41 with Fig. 6.36 admits the conclusion that α^2 is smaller in the coupled simulation. The final distribution functions in each direction are plotted in Fig. 6.42: Although transient non-Gaussian shapes may occur due to inter-species collisions, the final result of collisional relaxation is of course a Maxwellian, i.e. a Gaussian distribution function in each direction in velocity space.

6.7. **Noise Reduction Technique.** As mentioned above, statistical noise is one of the major problems that afflicts particle codes. In reservoir simulations, like those performed in this work, the problem can be tackled by increasing the number of particles, but this would necessarily increase the computational time. Ideally, one would like to have as many particles as possible during the reconstruction phase, but then relatively few during the so-called push phase. On the other side, in all the other situations where the spatial coordinate is of concern, the problem is to have a sufficient number of particles in each cell to be able to resolve a smooth distribution function. By means of the Gauss-Hermite polynomial expansion it is possible to fulfil both these requirements. For sake of simplicity the Euler scheme is considered so that each particle then moves according to

$$\mathbf{C}_{n+1}^{(\nu)} = \mathbf{C}_{n}^{(\nu)} + \Delta t\, \mathbf{F}_{n}^{(\nu)} + \sqrt{\Delta t}\, \mathbb{B}_{n}^{(\nu)}\, \vec{\eta}_{n}^{(\nu)} \quad \alpha = 1, \ldots, N_P \tag{166}$$

which in turn can be regarded as a Gaussian distributed random number drawn from a probability density with mean vector $\mathbf{C}_{M,n}^{(\nu)} = \mathbf{C}_{n}^{(\nu)} + \Delta t\, \mathbf{F}_{n}^{(\nu)}$ and variance matrix $\mathbb{V} = \Delta t\, \mathbb{B}_{n}^{(\nu)}\, \mathbb{B}_{n}^{(\nu)\,T} = \Delta t\, \mathbb{D}_{n}^{(\nu)}$, i.e. the normalised density distribution is given by $P(\mathbf{C}, t) = \frac{\sqrt{|\mathbb{D}^{-1}|}}{\left(2\pi\Delta t\right)^{3/2}} \exp\{-\frac{1}{2\Delta t}\mathbf{w}^{T}\mathbb{D}^{-1}\mathbf{w}\}$ with $\mathbf{w} = \mathbf{C} - \mathbf{C}_{M,n}^{(\nu)}$. Applying the transformation

$$\mathbf{C} = \mathbf{C}_{M,n}^{(\nu)} + \sqrt{2\,\Delta t}\, \mathbb{B}_{n}^{(\nu)}\, \mathbf{x}\,, \tag{167}$$

we introduce the sample average for an arbitrary function $\psi(\mathbf{C})$ according to

$$\langle \psi(\mathbf{C}) \rangle = \pi^{3/2} \int\limits_{\mathbb{R}^3} d^3x\, \psi(\mathbf{x})\, \mathrm{e}^{-\mathbf{x}^T\,\mathbf{x}} \approx \pi^{3/2} \sum_{i,j,k=1}^{N} \Omega_{i,j,k}\, \psi(\vec{\xi}_{i,j,k}) \tag{168}$$

which can be approximated by a Gauss-Hermite quadrature formula ([65]). Here, $\vec{\xi}_{i,j,k} = \left(\xi_1^{(i)}, \xi_2^{(j)}, \xi_3^{(k)}\right)^T$ and $\Omega_{i,j,k} = \omega_1^{(i)}\, \omega_2^{(j)}\, \omega_3^{(k)}$, where $\xi_m^{(n)}$ is the nth zero of the Hermite polynomial H_N of order N and the weights $\omega_m^{(n)}$ are obtained from $\omega_m^{(n)} = \frac{2^{N-1}N!\sqrt{\pi}}{N^2\left[H_{N-1}\left(\xi_m^{(n)}\right)\right]^2}$. From the latter relation for $\psi = 1$ it is immediately clear that the weights $\pi^{3/2}\Omega_{i,j,k}$ possess the property $\sum\limits_{i,j,k=1}^{N} \Omega_{i,j,k} = 1$. Furthermore, identifying the components of the vector (167) with ψ we obtain, we obtain the mean velocity

$$\langle \mathbf{C} \rangle = \pi^{3/2} \sum_{i,j,k=1}^{N} \Omega_{i,j,k}\, \vec{\mathcal{K}}_{i,j,k} = \mathbf{C}_{M,n}^{(\nu)}\,, \tag{169}$$

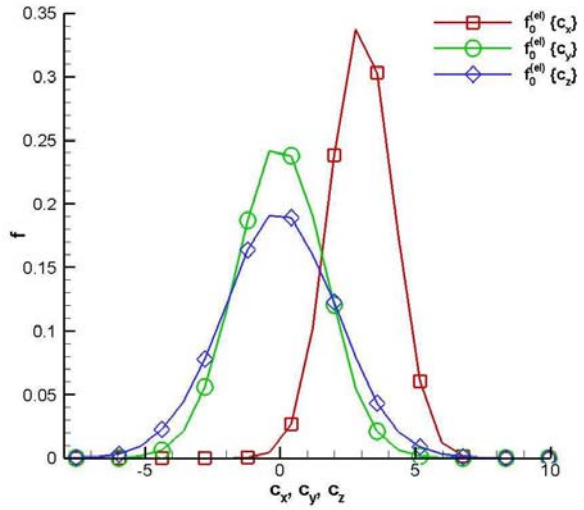

FIGURE 6.39. Anisotropic initialisation of the electron velocities for the coupled collision case. A Gaussian distribution function with different variance is prescribed in each direction. The $x-$ component has an additional stream velocity

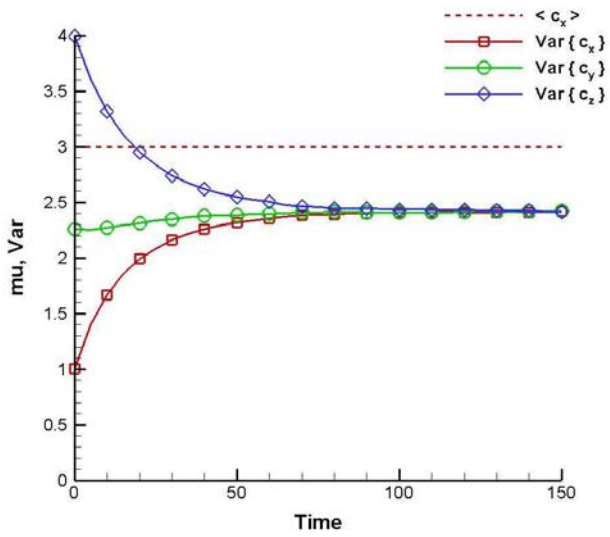

FIGURE 6.40. Mean and variance time evolution of the three velocity distribution functions during a (e,e) collision process. In this case, the mean value remain constant during the simulation and the variances fulfil the equipartition principle

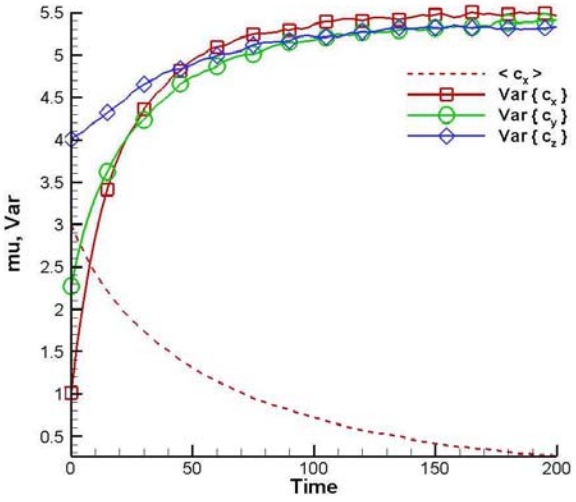

FIGURE 6.41. Mean and variance time evolution of the three velocity distribution functions during a (e,e)-(e,X) collision process. The thermal energy increases at expenses of the initial kinetic energy in the $x-$ direction

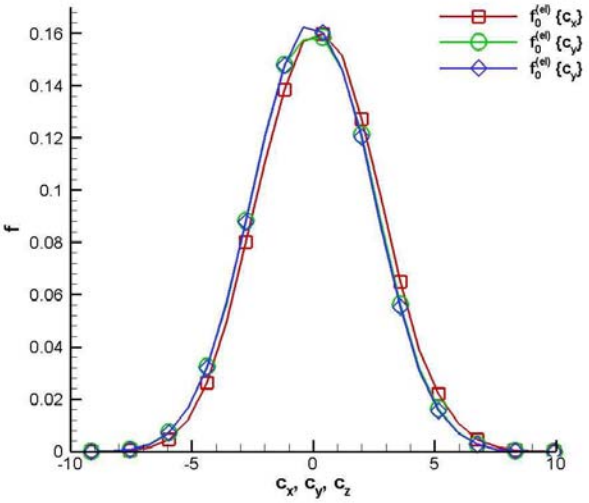

FIGURE 6.42. Distribution functions recorded at the end of the simulation. The shape recalls a Gaussian profile

where the velocities $\vec{\mathcal{K}}_{i,j,k}$ are given by

$$\vec{\mathcal{K}}_{i,j,k} = \mathbf{C}_{M,n}^{(\nu)} + \sqrt{2\,\Delta t}\,\mathbb{B}_n^{(\nu)}\,\vec{\xi}_{i,j,k}\ . \tag{170}$$

Obviously, the $\mathcal{K}_{i,j,k}$ can be regarded as the velocities of the $N_c = N^3$ "children" of the "parent" velocity $\mathbf{C}_{n+1}^{(\alpha)}$. These children, each with weight $\Omega_{i,j,k}$, possess the same mean vector (169) and variance matrix as the Gaussian random vector $\mathbf{C}_{n+1}^{(\nu)}$.

As benchmark, is here considered a reservoir of $3 \cdot 10^5$ electrons initialised according to

$$f(c_i, t_0) = \frac{1}{\sqrt{2\pi\sigma_i}} exp\{-\frac{(c_i - \mu_i)^2}{2\sigma^2}\} \tag{171}$$

where $\mu_1 = 0$, $\mu_2 = 0$ and $\mu_3 = 3$ and $\sigma_1 = 1$, $\sigma_2 = 1$ and $\sigma_3 = 1.5$, and the Coulomb collisions are let to operate the relaxation process. The CPU time obtained on a "Intel Centrino DUO" processor for this calculation ($\sim 11460 sec.$) also is used as reference. The same experiment has been repeated for three different numbers of "children" ($N_c = 3^3, 5^3$ and 10^3 respectively) while the number of "parents" (N_p) has been adjusted to preserve N_{tot} for comparison reasons. As expected, the best agreement with this test-case is obtained when $N_p = 11112$ and $N_c = 3^3$. The snapshots taken at $t = 25$ for the $y-$ and $z-$ component reveal almost no deviation from those resolved from the $3 \cdot 10^5$ distributions (see Fig. 6.43), while the variances curves in time are quite smooth (see Fig. 6.44). Even if from the computational time point of view this is very convenient ($\sim 2123 sec.$), the purpose is also to investigate very frequent cases in which the number of particles is particularly low and for this reason we restrict the analysis to $N_c = 10^3$ and $N_c = 5^3$ only. The two cases are also very similar in CPU time the former requiring $\sim 1844 sec.$ and the latter $\sim 1930 sec.$. As Figure 6.45 shows, the distribution function obtained with this technique looks broader than the test-case one, but definitively smoother than the one reconstructed with only 300 computational particles. Moreover, the time development of the variances is noisy (see 6.46) reflecting the poor statistics, linked with only 300 particles. It is important to remark here that per construction, the "children" bring no direct improvement in the moments of the distribution functions but only in its shape. When $N_c = 5^3$ and consequently $N_p = 2400$ the distribution function has both properties expected from this numerical tool, i.e. it is smooth and very close to the reference one (see Fig. 6.47). Finally, the comparison of the variances time trend for these cases reported in Figures 6.48 and 6.49 persuades that a number of ~ 2000 "parents" with 5^3 children each is the best trade-off between CPU time, resolution and moments of the distribution functions. However, the situation is catchier when the random velocity of particle ν is computed with the weak scheme (136), because this variable is, in general, not a simple Gaussian one. To get the mean of this velocity we have to estimate additional the quantity $\left[\mathcal{L}^{(0)}\,\vec{F}\right]$ (cf. expression (117)), what can be managed with the two support vectors explained previously by the relations (128) and (132). Moreover, one can show that the variance of the velocity determined with (136) in lowest order in Δt is the same as for the Euler velocity (166). Alternatively, it is possible to compute the total variance of the random vector (136) with the aid of the auxiliary vector (128) and model then (136) similar to the particle random velocity (166).

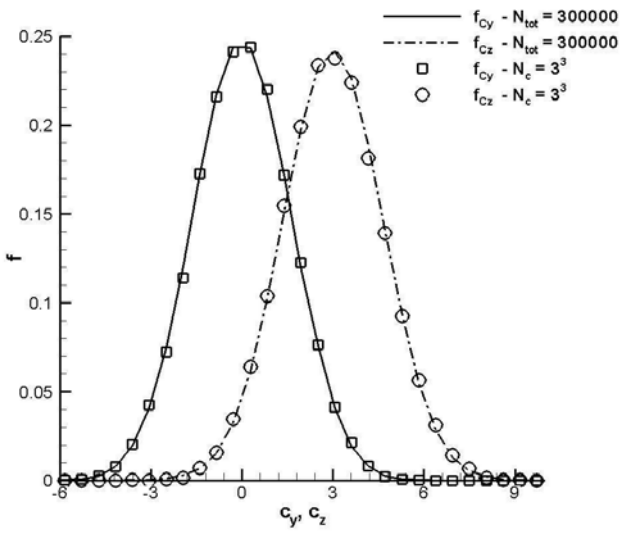

FIGURE 6.43. Comparison between the distribution functions in $y-$ and $z-$directions obtained with $3 \cdot 10^5$ field particles (lines) and with $N_p = 11112$ and $N_c = 3^3$ (symbols)

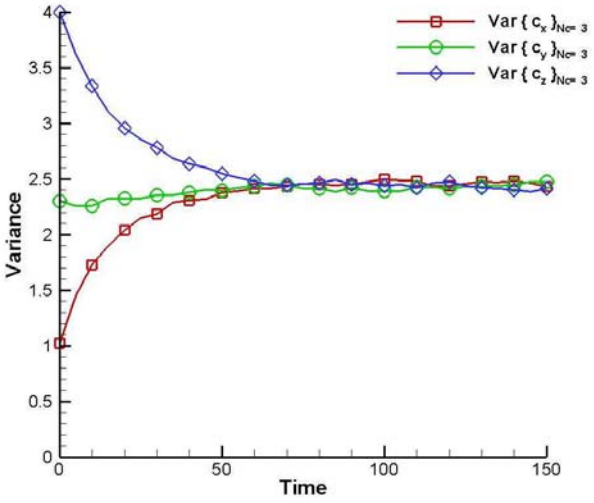

FIGURE 6.44. Variances time development for the case study $N_p = 11112$ and $N_c = 3^3$

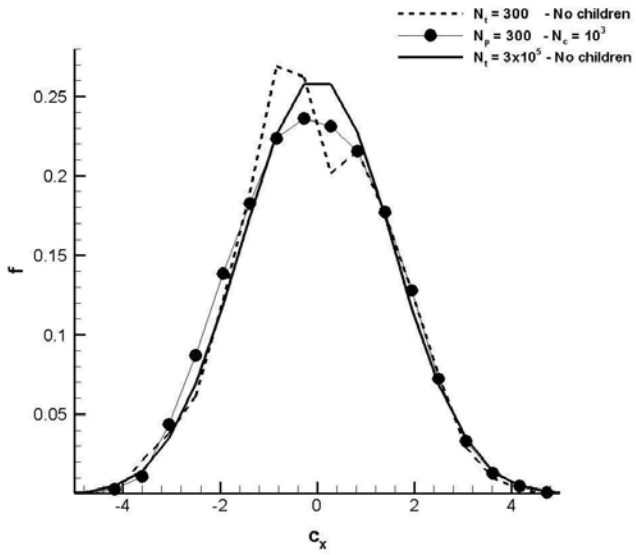

FIGURE 6.45. $f(c_x)$ for 300 and $3 \cdot 10^5$ field particles (dashed and bold line respectively) and in the case $N_p = 300$, each with 10^3 children (line with symbols) recorded after 600 cycles

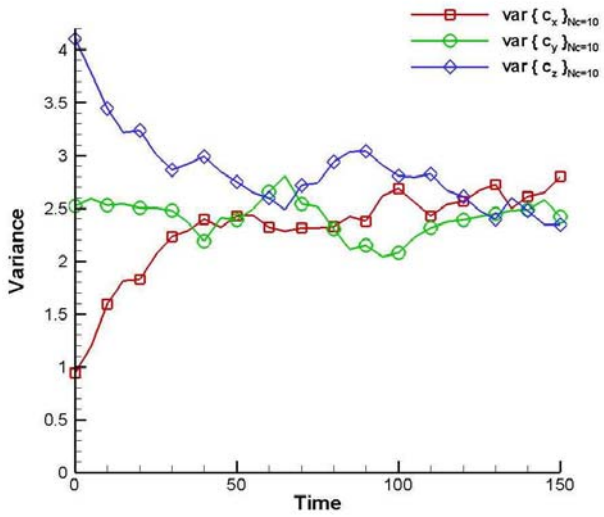

FIGURE 6.46. Variances time development for the case study $N_p = 300$ and $N_c = 10^3$

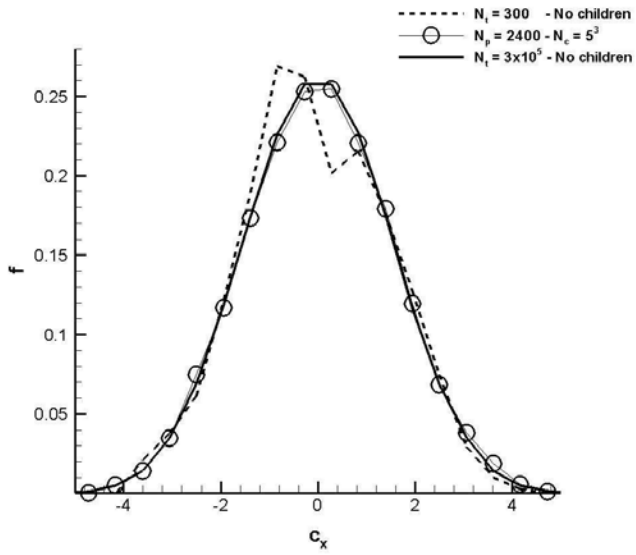

FIGURE 6.47. $f(c_x)$ for 300 and $3 \cdot 10^5$ field particles (dashed and bold line respectively) and in the case $N_p = 2400$ and $N_c = 5^3$ (line with symbols) recorded after 600 cycles

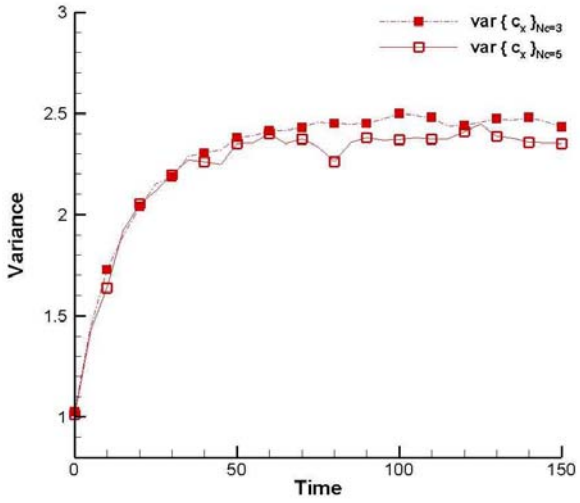

FIGURE 6.48. $\sigma^2(c_x)$ time trend for the two test cases $N_c = 3^3$ (line with filled symbols) and $N_c = 5^3$ (line with filled symbols)

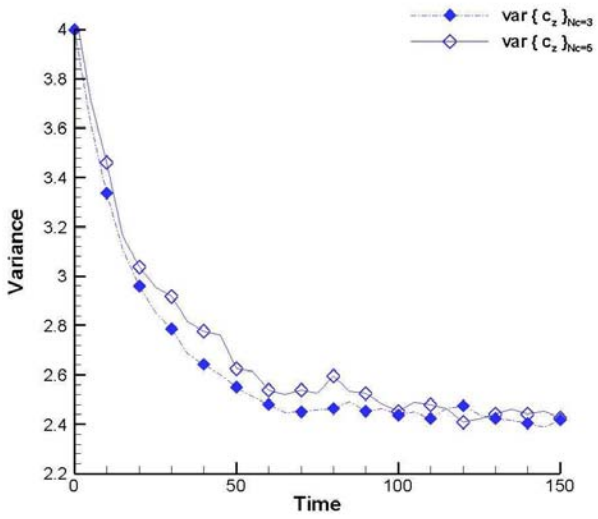

FIGURE 6.49. $\sigma^2(c_z)$ time trend for the two test cases $N_c = 3$ and $N_c = 5$

7. Conclusions

In the course of this work, a three dimensional fully self consistent Particle In Cell PIC code for Coulomb collisions simulation has been developed and tested in each single part with analytical solutions. The particles velocities have been evaluated at each time step from the numerical solution of the stochastic differential equation for which a first and second order weak scheme has also been implemented. The corresponding three dimensional velocity distribution function has been reconstructed on a velocity grid by means of a linear interpolation procedure and it has been used to update the friction and diffusion force via a Fast Fourier Transform technique. For the intra-species case, (scattering of charges of the same species) a detailed study of the relaxation process has been presented together with a deep insight in related physical features like the characteristic time scales and the high energy tail delay with respect to the core of the distribution. Pure numerical aspects have also been of concern: a renormalisation technique has been adapted to cure the artificial warming phenomenon and to guarantee the global conservation of momentum and energy.

The concept developed for intra-species electron scattering has been adapted to electron-ion inter-species collision. Due to the natural approximations the key quantities, that is the friction and diffusion coefficient, are now available in analytical form so that the velocity grid computations in the PIC cycle can be skipped. Some interesting aspects of the stochastic differential equation related to the lowest order approximation have been found: In this case an analytical solution of both the first and the second moment can be derived. These results serve as natural benchmark to test the local energy conservation approach for inter-species collision simulation. Furthermore, a coupled electron-electron and electron-ion collision simulation has been presented. In contrast to pure intra-species computations, due to inter-species colliosions, the coupled simulation possesses a mechanism to convert coherent flow of the electrons into disordered motion. Consequently, the numerical experiment shows that a non-isotropic initial configuration in velocity spaces relaxes to a Maxwellian, i.e. a Gaussian distribution function with zero mean and the variance in each direction in velocity space. Moreover, one of the major problems that affects the solution of particle codes is the statistical noise linked with a relative low number of particles. A numerical method has been engineered to tackle this problem by generating "ficticious" particles from the original grid particles in order to resolve a smoother distribution function during the reconstruction phase. Of course, these "children" as they have been called, posses specific properties namely the same mean value and the same variance of the distribution function where their "parents" come from. Very satisfactory results demonstrated the good quality of the proposed numerical tool.

The near futures goals to establish the final hybrid PIC-Monte-Carlo code PicLas are twofold. First, it is planned to couple the Fokker-Planck solver with the Direct-Simulation-Monte-Carlo module in order to study the interplay of the electron distribution function with inelastic reactions like excitation and ionisation of neutral atoms and molecules. Second, the coupling of the Fokker-Planck module with the Maxwell-Vlasov solver developed at IAG should bring

deeper insight in the complex interaction of collective plasma phenomena with charged particle Coulomb collisions.

References

[1] R.G. Jahn. *Physics of Electric Propulsion*. McGraw-Hill, New York, 1968.

[2] A. Nawaz, M. Auweter-Kurtz, H. Kurtz, and H.P. Wagner. Pulsed plasma thrusters for primary propulsion and attitude control of a small all electrical satellite. International Space Propulsion Conference, Sardinia, Italy June 7-8, 2004.

[3] A. Nawaz, U. Bauder, H. Böhrk, G. Herdrich, and M. Auweter-Kurtz. Electrostatic Probe and Camera Measurements for Modeling the iMPD SIMP-LEX. 43rd AIAA/ASME/SAE/ASEE Joint Propulsion Conference and Exhibit, July 8-11, Cincinnati, Ohio, AIAA-2007-75328, 2007.

[4] C.-D. Munz, R. Schneider, E. Sonnendrücker, E. Stein, U. Voß, and T. Westermann. A finite-volume particle-in-cell method for the numerical treatment of the Maxwell-Lorentz equations on boundary-fitted meshes. *Int. J. Numer. Meth. Engng.*, 44:461–487, 1999.

[5] C.-D. Munz, R. Schneider, and U. Voß. A finite-volume particle-in-cell method for the numerical simulation of devices in pulsed power technology. *Surv. Math. Ind.*, 8:243–257, 1999.

[6] M. Auweter-Kurtz, M. Fertig, D. Petkow, T. Stindl, M. Quandt, C.-D. Munz, P. Adamis, M. Resch, S. Roller, D. D'Andrea, and R. Schneider. Development of a hybrid PIC/DSMC code. IEPC-2005-71, Proceedings of the 29th International Electric Propulsion Conference, Princeton, USA, 2005.

[7] D. Petkow, M. Fertig, T. Stindl, M. Auweter-Kurtz, M. Quandt, C.-D. Munz, S. Roller, D. D'Andrea, and R. Schneider. Development of a 3-Dimensional, Time Accurate Particle Method for Rarefied Plasma Flows. AIAA-2006-3601, Proceedings of the 9th AIAA/ASME Joint Thermophysics and Heat Transfer Conference, San Francisco, USA, 2006.

[8] M. Laux. *Direkte Simulation verdünnter, reagierender Strömungen*. PhD thesis, Institut für Raumfahrtsysteme, Universität Stuttgart, Germany, 1996.

[9] G.A. Bird. *Molecular Gas Dynamics and the Direct Simulation of Gas Flows*. Clarendon Press, Oxford, 1994.

[10] T. Westermann. Numerische Simulation von technisch relevanten Ionen-Dioden mit der Particle-inCell Methode. *Kernforschungszentrum Karlsruhe,* **KfK 4510**, 1989.

[11] T. Westermann. Numerical modelling of the stationary Maxwell-Lorentz system in technical devices. *Int. J. Num. Mod.*, 7:43–67, 1994.

[12] M. Fedoruk, C.-D. Munz, P. Omnes, and R. Schneider. A Maxwell-Lorentz solver for self-consistent particle-field simulations on unstructured grids. *Forschungszentrum Karlsruhe – Technik und Umwelt,* **FZKA 6115**, 1998.

[13] C.K. Birdsall and A.B. Langdon. *Plasma Physics via Computer Simulation*. Adam Hilger, Bristol, Philadelphia, New York, 1991.

[14] R. Hockney and J. Eastwood. *Computer Simulation using Particles*. McGraw-Hill, New York, 1981.

[15] C.-D. Munz, P. Omnes, and R. Schneider. A three-dimensional finite-volume solver for the Maxwell equations with divergence cleaning on unstructered meshes. *Computer Physics Communications*, 130:83 – 117, 2000.

[16] Y.J. Lee, C.-D. Munz, and R. Schneider. Lagrangian and symmetry structure of the divergence cleaning model based on generalized Lagrange multipliers. *Int. J. of Mod. Phys. C*, 15:59–114, 2004.

[17] C.-D. Munz, P. Omnes, R. Schneider, E. Sonnendrücker, and U. Voß. Divergence correction techniques for Maxwell solvers based on a hyperbolic model. *J. Comput. Phys.*, 161:484 – 511, 2000.

[18] G.B. Jacobs and J.S. Hesthaven. High-order nodal discontinuous Galerkin particle-in-cell method on unstructured grids. *J. Comput. Phys.*, 214:96 – 121, 2006.

[19] K.S. Yee. Numerical solution of the initial boundary value problems involving Maxwell's equation in isotropic media. *IEEE Trans. Antennas and Propagation*, AP-14:302–307, 1966.

[20] J. Quintenz, D. Seidel, M. Kiefer, T. Pointon, R. Coats, S. Rosenthal, T. Mehlhorn, M. Desjarlais, and N. Krall. Simulation codes for light-ion diode modeling. *Laser Particle Beams*, 12:283–324, 1994.

[21] C.-D. Munz, R. Schneider, and U. Voß. A finite-volume method for the Maxwell equations in the time domain. *SIAM J. Sci. Comput.*, 22:449 – 475, 2000.

[22] F. Assous, P. Degond, E. Heintze, P.-A. Raviart, and J. Segre. On a finite-element method for solving the three-dimensional Maxwell equations. *J. Comput. Phys.*, 109:222–237, 1993.

[23] T. Schwartzkopff, F. Lörcher, C.-D. Munz, and R. Schneider. Arbitrary high order finite-volume methods for electromagnetic wave propagation. *Computer Physics Communications*, 174:689–703, 2006.

[24] A. Taube, M. Dumbser, C.-D. Munz, and R. Schneider. A high order discontinuous Galerkin method with local time stepping for the Maxwell equations. *International Journal of Modelling: Electronic Networks, Devices and Fields.*, DOI 10.1002/jnm.700, 2008.

[25] J. P. Boris. Relativistic plasma simulations – Optimization of a hybrid code. In *Proc. 4th Conf. on Num. Sim. of Plasmas*, pages 3–67, NRL Washington, Washington DC, 1970.

[26] V. Fuchs and J.P. Gunn. On the integration of equations of motion for particle-in-cell codes. *J. Comput. Phys.*, 214:299–315, 2006.

[27] M. Quandt, C.-D. Munz, and R. Schneider. A high order relativistic particle push method for PIC simulations. *IEPC-2007-71, Proceedings of the 30th International Electric Propulsion Conference, Florence, Italy*, 2007.

[28] D. D'Andrea, M. Fertig, C.-D. Munz, S. Roller, and R. Schneider. Long range particle collisions for the PIC/DSMC simulations for code PicLas. *IEPC-2005-36, Proceedings of the 30th International Electric Propulsion Conference, Florence, Italy*, 2007.

[29] K. Nishikawa and M. Wakatani. *Plasma Physics*. Springer, Berlin, Heidelberg, 2000.

[30] D. Montgomery and D. Tidman. *Plasma Kinetic Theory*. McGraw-Hill, New York, 1964.

[31] D. Diver. *A Plasma Formulary for Physics, Technology, and Astrophysics*. Wiley-VCH Verlag, Berlin, 2001.

[32] T.J.M. Boyd and J.J. Sanderson. *The Physics of Plasmas*. Cambridge University Press, Cambridge, 2003.

[33] A. Nawaz, M. Auweter-Kurtz, G. Herdrich, and H. Kurtz. Impulse measurement and thermal investigation of simp-lex. AIAA/ASME/SAE/ASEE Joint Propulsion Conference and Exhibit Sacramento, CA, 9-12 July, USA, 2006.

[34] M. Mitchner and C. Kruger. *Partially Ionized Gases*. Wiley, New York, 1973.

[35] R.C. Tolman. *The Principles of Statistical Mechanics*. Dover Publications, New York, 1979.

[36] S. Chandrasekhar. *Principles of Stellar Dynamics*. University of Chicago Press, Chicago, 1942.

[37] S.R. DeGroot and P. Mazur. *Non-Equilibrium Thermodynamics*. Dover Publications, New York, 1984.

[38] C. W. Gardiner. *Handbook of Stochastic Methods*. Springer Verlag, Berlin, Heidelberg, New York, 1985.

[39] J. Honerkamp. *Stochastische Dynamische Systeme*. VCH Verlagsgesellschaft, Weinheim, 1990.

[40] W. Manheim, M. Lampe, and G. Joyce. Langevin representation of Coulomb collision in PIC simulation. *J. Comput. Phys.*, 138:563–584, 1997.

[41] B.J. Albright, D. Winske, D.S. Lemons, W. Daughton, and M.E. Jones. Quite simulation of Coulomb collision. *IEEE Trans. Plasma Sci.*, 31:19–24, 2003.

[42] M. Rosenbluth, W. MacDonald, and D. Judd. Fokker-Planck equation for an inverse-square force. *Phys. Rev.*, 107:1–6, 1957.

[43] G. Horwitz and E. Dagan. The covariant Boltzmann-Fokker-Planck equation and its associated short-time transition probability. *J. Phys. A: Math. Gen.*, 21:1017–1028, 1988.

[44] M.R. Spiegel. *Vektoranalysis*. McGraw-Hill, Schaum's Outline, Hamburg, New York, 1984.

[45] S. Hassani. *Mathematical Physics*. Springer, New York, Berlin, 1999.

[46] H. Risken. *The Fokker-Planck Equation*. Springer-Verlag, Berlin, 1989.

[47] A. Einstein. Über die von der molekularkinetischen Theorie der Wärme geforderte Bewegung von in ruhenden Flüssigkeiten suspendierten Teilchen. *Ann. Phys.*, 17:549–560, 1905.

[48] M. Smoluchowski. Zur kinetischen Theorie der Brownschen Molekularbewegung und der Suspensionen. *Ann. d. Physik*, 21:756–780, 1906.

[49] P.E. Kloeden and E. Platen. *Numerical Solution of Stochastic Differential Equations*. Springer-Verlag, Berlin, Heidelberg, New York, 1999.

[50] P.E. Kloeden, E. Platen, and H. Schurz. *Numerical Solution of SDE Through Computer Experiments*. Springer-Verlag, Berlin, Heidelberg, New York, 2003.

[51] R. Morse and C. Nielson. Numerical simulation of the Weibel instability in one and two dimensions. *Physics of Fluids*, 14:830–840, 1971.

[52] E.O. Brigham. *The Fast Fourier Transform and its Application*. Prentice-Hall, Englewood Cliffs, 1988.

[53] W.L. Briggs and V.E. Henson. *The DFT*. SIAM, Philadelphia, 1995.

[54] W. H. Press, B. P. Flannery, S. A. Teukolsky, and W. T. Vetterling. *Numerical Recipes*. Cambridge University Press, Cambridge, 1987.

[55] H.J. Nussbaumer. *Fast Fourier Transform and Convolution Algorithms*. Springer, Berlin, Heidelberg, New York, 1981.

[56] J. W. Cooley and J. W. Tukey. An algorithm for the machine calculation of complex Fourier series. *Math. Comput.*, 19:297–301, 1965.

[57] C. F. Gauss. *"Nachlass: Theoria interpolationis methodo nova tractata", Werke, Band 3*. Königliche Gesellschaft der Wissenschaften, Göttingen, 1866.

[58] M. T. Heideman, D. H. Johnson, and C. S. Burrus. Gauss and the history of FFT. *IEEE Acoustics, Speech, and Signal Processing Magazine*, 1:14–21, 1984.

[59] G.C. Danielson and C. Lanczos. Some improvements in practical Fourier analysis and their application to X-ray scattering from liquids. *J. Franklin Inst.*, 233:315–380, 435–452, 1942.

[60] D.S. Lemons, J. Lackman, M.E. Jones, and D. Winske. Noise-induced instability in self-consistent Monte Carlo calculations. *Physical Review E*, 52:6855–6861, 1995.

[61] D. D'Andrea, C.-D. Munz, and R. Schneider. Modeling of electron-electron collisions for particle-in-cell simulations. **FZKA 7218** *Research Report, Forschungszentrum Karlsruhe – in der Helmholtz-Gemeinschaft*, 2006.

[62] A. Sommerfeld. *Thermodynamik und Statistik, Band V*. Verlag Harri Deutsch, Thun, Frankfurt/M., 1977.

[63] R.D. Hazeltine and J.D. Meiss. *Plasma Confinement*. Addison-Wesley, Redwood City, CA, 1991.

[64] L. Spitzer. *Physics of Fully Ionised Gases*. Interscience Publishers, Inc., New York, 1956.

[65] M. Abramowitz and I.A. Stegun. *Handbook of Mathematical Functions*. Dover Publications, New York, 1972.

Appendix A. Boltzmann Collision Integral and Fokker-Planck Approximation

The Boltzmann collision interal (cf. [30, 31]) is given by

$$\left(\frac{\delta f_\alpha}{\delta t}\right)_{\rm col} = \sum_\beta n_\beta(\mathbf{x},t) \int d^3w\, d\Omega\, g\, Q_{\alpha\beta} \left[\Phi_{\alpha\beta}(\mathbf{c}',\mathbf{w}') - \Phi_{\alpha\beta}(\mathbf{c},\mathbf{w})\right] , \tag{A-1}$$

where $\Phi_{\alpha\beta}(\mathbf{c},\mathbf{w}) = f_\alpha(\mathbf{c})\, f_\beta(\mathbf{w})$ is the product of the test and field particle distribution functions. Here, the index β runs over all "scattering" populations (field particles), n_β is the local number density of the field particle specie "β", $g = |\mathbf{g}| = |\mathbf{c} - \mathbf{w}|$ is the absolute value of the relative velocity, $Q_{\alpha,\beta} = Q_{\alpha,\beta}(g,\chi,\varphi)$ is the differential scattering cross section (in the CM system) between the particles of the species "α" and "β" and the element of solid angle $d\Omega$ is given by $d\Omega = \sin\chi\, d\chi\, d\varphi$ (χ: scattering angle, φ: azimuthal angle). Moreover, the prime refers to the value of a quantity after a collision and unprimed denotes the values before the collision. In order to obtain from the collision integral (A-1) the Fokker-Planck approximation, the following laws and approximations are applied. First, to describe charged particles interaction we use the Rutherford differential scattering cross section (see Appendix B). During the elastic collision $\mathbf{g}$ is rotated to $\mathbf{g}' = \mathbf{c}' - \mathbf{w}'$ with $|\mathbf{g}'| = |\mathbf{g}|$ and, furthermore, $\mathbf{c}' = \mathbf{c} + \Delta\mathbf{c}$ and $\mathbf{w}' = \mathbf{w} + \Delta\mathbf{w}$ is assumed for small angle (large impact parameter) scattering, where $\Delta\mathbf{c}$ and $\Delta\mathbf{w}$ are, respectively, given by $\Delta\mathbf{c} = m_{\alpha\beta}/m_\alpha\, \Delta\mathbf{g}$ and $\Delta\mathbf{w} = -m_{\alpha\beta}/m_\beta\, \Delta\mathbf{g}$. Then, a Taylor series expansion of $\Phi_{\alpha\beta}(\mathbf{c}',\mathbf{w}')$ is performed up to second order. Taking into account conservation of momentum and performing some rearrangements, we can write $\Delta\mathbf{g} = \mathbf{g}' - \mathbf{g}$ according to

$$\Delta\mathbf{g} = g\, \vec{\omega}(\chi,\varphi) , \tag{A-2}$$

where the angle-dependent part is given by

$$\vec{\omega}(\chi,\varphi) = \begin{pmatrix} -2\sin^2(\chi/2) \\ \sin\chi\, \cos\varphi \\ \sin\chi\, \sin\varphi \end{pmatrix} . \tag{A-3}$$

Besides, the vector quantity (A-2) the tensor quantity

$$\Delta\mathbf{g}\, \Delta\mathbf{g}^T = g^2\, \vec{\omega}\, \vec{\omega}^T \tag{A-4}$$

appears in the resulting expression of the approximated Boltzmann collision integral. For small angle cut-off $\chi_{\rm min}$ (see Appendix B), the integration over the azimuthal and scattering angles yields

$$\begin{aligned} < \Delta\mathbf{g} > &= \int_0^{2\pi} d\varphi \int_{\chi_{\rm min}}^{\pi} d\chi\, \sin\xi\, Q_{\alpha\beta}(\chi,\varphi)\, \Delta\mathbf{g} \\ &= \frac{4\pi C^2}{m_{\alpha\beta}^2 g^2} \ln\left[\sin\left(\frac{\chi}{2}\right)\right] \mathbf{e}_x , \quad \mathbf{e}_x = \frac{\mathbf{g}}{g} \end{aligned} \tag{A-5}$$

for the vector and

$$< \Delta\mathbf{g}\,\Delta\mathbf{g}^T > \;=\; \int_0^{2\pi} d\varphi \int_{\chi_{\min}}^{\pi} d\chi\, \sin\chi\, Q_{\alpha\beta}(\chi,\varphi)\,\Delta\mathbf{g}\,\Delta\mathbf{g}^T$$

$$= \; -\frac{4\pi C^2}{m_{\alpha\beta}^2 g^2} \ln\left[\sin\left(\frac{\chi}{2}\right)\right] \frac{1}{g}\left(\mathbb{I} - \mathbf{e}_x\,\mathbf{e}_x^T\right) \qquad \text{(A-6)}$$

for the tensor quantity, where expressions like $8\pi\left[1+\cos\chi_{\min}\right]$ and $8\pi\cos^2\left(\chi_{\min}/2\right)$ are neglected, because they are very small compared to $\ln\left[\sin\left(\frac{\chi}{2}\right)\right]$ for small $\chi = \chi_{\min}$. After performing some straightforward but lengthy algebra, we finally obtaion the FP equation (19) given in Section 2, which represents the lowest order approximation to the Boltzmann integral (A-1) and takes into account small-angle scattering of point charges on the Coulomb potential.

Appendix B. Differential Rutherford Scattering Cross Section

The classical Rutherford differential scattering cross section of two charged particles of types "α" and "β" is given by (see, for instance [34])

$$Q_{\alpha\beta}(g,\chi,\varphi) = \frac{1}{4}\Big(\frac{C}{m_{\alpha\beta}}\Big)^2 \frac{1}{g^4\,\sin^4\Big(\frac{\chi}{2}\Big)} \tag{B-1}$$

where $m_{\alpha\beta}$ denotes the reduced mass and the constant C is given by $C = -\frac{q_\alpha\, q_\beta}{4\pi\,\epsilon_0}$. This result is obtained for a Coulomb potential ($V = C/r$) for which it is well-known that the total cross section for isotropic scattering

$$\sigma_T(g) = 2\pi \int^{\pi} Q_{\alpha\beta}(g,\chi)\,\sin\chi d\chi \tag{B-2}$$

diverges at the lower boundary ($\xi = 0$) as a consequence of this potential. Under the assumption that the Coulomb fields of all particles are screened by the collective behavior of these charges, the effective range of the Coulomb force may be estimated by the Debye length λ_D:

$$\frac{1}{\lambda_D^2} = \sum_\alpha \frac{n_\alpha\, q_\alpha^2}{\epsilon_0\, k\, T_\alpha}\,. \tag{B-3}$$

Clearly, this length represents a natural estimation of the maximal impact parameter $b_{\max} = \lambda_D$, to which the minimal cut-off scattering angle $\chi_{\min}$ is related according to

$$\sin\Big(\frac{\chi}{2}\Big) = \frac{b_0}{b}\Big[1+\Big(\frac{b_0}{b}\Big)^2\Big]^{-1/2} = \frac{1}{\sqrt{1+\Big(\frac{b}{b_0}\Big)^2}} \tag{B-4}$$

for $b = \lambda_D$, where $b_0 = \frac{|C|}{m_{\alpha\beta}\,g^2}$ is the impact parameter for $\chi = \pi/2$ scattering. In the case, where $b_0/\lambda_D \ll 1$, the minimal scattering angle is simply given by

$$\sin\Big(\frac{\chi_{\min}}{2}\Big) \approx \frac{b_0}{\lambda_D} = \frac{1}{\Lambda}\,, \tag{B-5}$$

where Λ is defined by $\Lambda = \lambda_D/b_0$ and can be interpreted as the measure of the number of particles in a sphere of radius λ_D and is sometimes called "*plasma parameter*" in the literature. For practical estimations and calculations it is sensible to approximate the mean kinetic energy roughly by the thermal energy – $\frac{1}{2}m_{\alpha\beta}\,g^2 \approx \frac{3}{2}\,k_{\rm B}\,T_\alpha$ – and replace b_0 by

$$\overline{b}_0 = \frac{|q_\alpha\, q_\beta|}{12\pi\epsilon_0\, k_{\rm B}\, T_\alpha}\,. \tag{B-6}$$

Clearly, expression (B-5) relates the small scattering angle cut-off to maximal impact parameter $b_{\max} = \lambda_D$, which reflects the collective screening in a plasma. Obviously, it is not amazing that the cut-off scattering angle $\chi_{\min}$ is responsible for the main contribution to the totat Coulomb cross section according to (B-2):

$$\sigma_T(g) = \pi\,\lambda_D^2\,. \tag{B-7}$$

Especially, if the parameter Λ is very large, large-angle collisions among plasma particles can be neglected and the collisional dynamics is dominated by small-angle collisions, which is well-modeled by the Fokker-Planck approach.

Appendix C. Short-time Solution of the FP equation

To obtain the short-time solution $S(\mathbf{c},t)$ of the FP equation (22) in Section 3 for given initial data

$$S_0(\mathbf{c},t) = \delta\Big(\mathbf{c}-\mathbf{c}_0\Big)\;, \tag{C-1}$$

it is sufficient to study the solution of the equation

$$\frac{\partial S}{\partial t} = -F_p\,\frac{\partial\, S}{dc_p} + \frac{1}{2}D_{pq}\,\frac{\partial^2\, S}{\partial c_p \partial c_q}\;. \tag{C-2}$$

This is correct, because for small τ the solution of the FP equation will be sharply peaked and, hence, the derivatives of the friction $F_p = F_p(\mathbf{c},t)$ and the diffusion $D_{pq} = D_{pq}(\mathbf{c},t)$ coefficients can be neglected compared to those of S. Consequently, we will assume that F_p and D_{pq} are approximately constant within the time interval $[t,\, t+\tau]$. To find the solution of problem (C-2), we apply Fourier transformation techniques and exploit some properties of this transformation to obain the result

$$\hat{S}(\mathbf{k},\tau) = \frac{\mathrm{e}^{-i\mathbf{k}\cdot\mathbf{c}_0}}{(2\pi)^{3/2}}\,\exp\!\left\{-\Big(i\mathbf{F}\cdot\mathbf{k}+\frac{1}{2}\mathbf{k}^T\,\mathbb{D}\,\mathbf{k}\Big)\,\tau\right\}\;, \tag{C-3}$$

where τ denotes the small time increment. To get the inverse Fourier transformation of the latter equation we define the following auxiliary vector and matrix

$$\mathbf{V} \;=\; \mathbf{c}-\mathbf{c}_0-\tau\,\mathbf{F} \tag{C-4}$$

$$\tilde{\mathbb{D}} \;=\; \big[\tau\,\mathbb{I}\big]\,\mathbb{D}\;, \tag{C-5}$$

where $\mathbb{I}$ denotes the identity. Since the diffusion matrix $\mathbb{D}$ (and consequently $\tilde{\mathbb{D}}$) is a symmetric matrix, it is convenient to apply the substitution

$$\mathbf{z} = \mathbf{k} - i\,\tilde{\mathbb{D}}^{-1}\mathbf{V} \tag{C-6}$$

to find the relation

$$\mathbf{k}^T\,\tilde{\mathbb{D}}\mathbf{k} - 2i\,\mathbf{V}\cdot\mathbf{k} = \mathbf{z}^T\,\tilde{\mathbb{D}}\mathbf{z} + \mathbf{V}^T\,\tilde{\mathbb{D}}^{-1}\mathbf{V}\;. \tag{C-7}$$

To solve the remaining integral $\int\limits_{-\infty}^{\infty} d^3z\,\exp\!\Big\{-\frac{1}{2}\mathbf{z}^T\,\tilde{\mathbb{D}}\mathbf{z}\Big\}$, we once again apply the fact that $\tilde{\mathbb{D}}$ is symmetric, which guarantees that there exists an orthogonal matrix $\mathbb{O}$ with the property $\tilde{\mathbb{S}} = \mathbb{O}^T\tilde{\mathbb{D}}\,\mathbb{O} = \mathsf{diag}[\tilde{s}_1^2,\,\tilde{s}_2^2,\,\tilde{s}_3^2]$. Finally, a straightforward computation leads to the result

$$\begin{aligned} S(\mathbf{c},\tau) \;&=\; \frac{\sqrt{|\tilde{\mathbb{D}}^{-1}|}}{(2\pi)^{3/2}}\,\exp\!\Big\{-\frac{1}{2}\mathbf{V}^T\,\tilde{\mathbb{D}}^{-1}\mathbf{V}\Big\} \\ &=\; \frac{\sqrt{|\mathbb{D}^{-1}|}}{(2\pi\,\tau)^{3/2}}\,\exp\!\Big\{-\frac{1}{2\,\tau}\big(\delta\mathbf{c}-\tau\,\mathbf{F}\big)^T\,\mathbb{D}^{-1}\big(\delta\mathbf{c}-\tau\,\mathbf{F}\big)\Big\} \end{aligned} \tag{C-8}$$

which represents the back transformation of expression (C-3) and the solution of (C-2), where $\delta\mathbf{c} = \mathbf{c}-\mathbf{c}_0$. Clearly, this result represents a (two parameter) Gaussian distribution for $\delta\mathbf{c}$ with mean value $\tau\,\mathbf{F}$ and variance $\tau\,\mathbb{D}$. Note, that the matrix of the standard deviation $\mathbb{B}$ can be expressed according to

$$\sqrt{\tau}\,\mathbb{B} = \sqrt{\tau}\,\mathbb{O}\,\mathbb{S}^{1/2}\mathbb{O}^T\;,$$

where $\mathbb{O}$ is a orthogonal matrix and $\mathbb{S} = \mathbb{O}^T \mathbb{D}\, \mathbb{O} = \mathsf{diag}[s_1^2,\, s_2^2,\, s_3^2]$. Under the assumption that $\mathbb{D} = \mathsf{diag}[D_1,\, D_2,\, D_3]$ holds, we can immediately recast equation (C-8) into the form

$$S(\mathbf{c}, \tau) = \prod_{\alpha=1}^{3} \frac{1}{\sqrt{2\pi\,\tau}\,\sigma_\alpha} \exp\left\{ -\frac{(c_\alpha - \mu_\alpha)^2}{2\sigma_\alpha^2} \right\}, \tag{C-9}$$

where the abbreviations

$$\mu_\alpha = v_{0,\alpha} + \tau\, F_\alpha \quad \text{and} \quad \sigma_\alpha^2 = \tau\, D_\alpha \tag{C-10}$$

are used, which are, respectively, the mean value and the variance of the α^{th} Gaussian normal distribution.

Appendix D. Three Dimensional Solution of the Lenard-Bernstein Model

In the following we briefly sketch the analytical solution of the Lenard-Bernstein model (see, [29] for the one-dimensional and [37, 46] for the three-dimensional case), which is also known in the literature as the Ornstein-Uhlenbeck process. The model is established by the assumption that the friction force and the (symmetric) diffusion tensor are given by

$$\mathbf{F}(\mathbf{x},\mathbf{c},t) = -\mathbb{A}\,\mathbf{c} \quad \text{and} \quad \mathbb{D}(\mathbf{x},\mathbf{c},t) = \mathbb{D}(\mathbf{x},t)\;, \tag{D-1}$$

where the matrix $\mathbb{A} \in \mathbb{R}^{3\times 3}$, in general, may be depend on $\mathbf{x}$ and t. Then, the FP equation for the transition probability $P(\mathbf{c},t) = P(\mathbf{c},t|(\mathbf{c}_0,t_0)$ can be written as

$$\partial_t P(\mathbf{c},t) - A_{pq}\,c_q\,\frac{\partial P(\mathbf{c},t)}{\partial c_p} = Tr(\mathbb{A})P(\mathbf{c},t) + \frac{1}{2}D_{pq}\,\frac{\partial^2 P(\mathbf{c},t)}{\partial c_p \partial c_q}\;, \tag{D-2}$$

where $Tr(\mathbb{A})$ denotes the trace of the matrix $\mathbb{A}$. This equation is complemented by the initial condition $P_0(\mathbf{c}) = P(\mathbf{c},t_0|\mathbf{c}_0,t_0) = \delta(\mathbf{c}-\mathbf{c}_0)$. In order to replace the left-hand side of the latter equation by the substantial derivative, we introduce the variable transformation

$$\mathbf{u} = \mathrm{e}^{\mathbb{A}\,(t-t_0)}\mathbf{c} \quad \Leftrightarrow \quad \mathbf{c} = \mathrm{e}^{-\mathbb{A}\,(t-t_0)}\mathbf{u} \tag{D-3}$$

and get after some algebra the equation for $P(\mathbf{u},t) = P(\mathbf{u},t|\mathbf{u}_0,t_0)$

$$\frac{dP(\mathbf{u},t)}{dt} = Tr(\mathbb{A})\,P(\mathbf{u},t) + \frac{1}{2}\nabla_u^T\,\mathrm{e}^{\mathbb{A}\,(t-t_0)}\,\mathbb{D}\,\mathrm{e}^{\mathbb{A}^T\,(t-t_0)}\,\nabla_u\,P(\mathbf{u},t) \tag{D-4}$$

with the initial data $P_0(\mathbf{u}) = P(\mathbf{u},t_0|\mathbf{u}_0,t_0) = \delta(\mathbf{u}-\mathbf{u}_0)$. Applying a Fourier transformation according to $\hat{P}(\mathbf{k},t) = \frac{1}{\left(2\pi\right)^{3/2}}\int\limits_{-\infty}^{\infty} d^3u\,\mathrm{e}^{-i\mathbf{k}\cdot\mathbf{u}}P(\mathbf{u},t)$, yields an ordinary differential equation in time whose solution reads as

$$\hat{P}(\mathbf{k},t) = \frac{1}{\left(2\pi\right)^{3/2}}\exp\left\{Tr(\mathbb{A})\,(t-t_0) - i\mathbf{u}_0^T\,\mathbf{k} - \frac{1}{2}\mathbf{k}^T\,\mathbb{M}\,\mathbf{k}\right\}\;, \tag{D-5}$$

where the initial condition $\hat{P}_0(\mathbf{k}) = \frac{1}{(2\pi)^{3/2}}\mathrm{e}^{-i\mathbf{k}\cdot\mathbf{u}_0}$ already has been inserted and $\mathbb{M}$ is given by

$$\mathbb{M} = \int\limits_{t_0}^{t} \mathrm{e}^{\mathbb{A}\,(s-t_0)}\,\mathbb{D}\,\mathrm{e}^{\mathbb{A}^T\,(s-t_0)}ds\;. \tag{D-6}$$

To perform the integration with respect to time, we consider

$$\mathrm{e}^{\mathbb{A}\,(s-t_0)}\,\mathbb{D}\,\mathrm{e}^{\mathbb{A}^T\,(s-t_0)} = \frac{d}{ds}\Big[\mathrm{e}^{\mathbb{A}\,(s-t_0)}\,\mathbb{G}\,\mathrm{e}^{\mathbb{A}^T\,(s-t_0)}\Big] \tag{D-7}$$

and conclude that $\mathbb{G}$ has to be a symmetric matrix (since $\mathbb{D}$ is symmetric) defined by

$$\mathbb{D} = \mathbb{A}\,\mathbb{G} + \mathbb{G}\,\mathbb{A}^T\;. \tag{D-8}$$

Then expression (D-6) reads as

$$\mathbb{M} = \mathrm{e}^{\mathbb{A}\,(t-t_0)}\,\mathbb{G}\,\mathrm{e}^{\mathbb{A}^T\,(t-t_0)} - \mathbb{G} \tag{D-9}$$

which reveals that $\mathbb{M}$ is also a (real) symmetric matrix. Performing the inverse Fourier transformation of the expression (D-5) we obtain the intermediate result

$$P(\mathbf{u},t) = \frac{\mathrm{e}^{Tr(\mathbb{A})\,(t-t_0)}}{(2\pi)^3} \int\limits_{-\infty}^{\infty} d^3k\, \exp\!\Big\{-\frac{1}{2}\mathbf{k}^T\,\mathbb{M}\,\mathbf{k} + i\,\mathbf{V}^T\mathbf{k}\Big\}\,, \tag{D-10}$$

where the abbreviation $\mathbf{V} = \mathbf{u} - \mathbf{u}_0$ is introduced. With the auxiliary vector

$$\mathbf{x} = \mathbf{k} - i\,\mathbb{M}^{-1}\,\mathbf{V} \tag{D-11}$$

the exponent of the integrand can be reformulated in such a way that only the integral $\int\limits_{-\infty}^{\infty} d^3x\, \exp\!\Big\{-\frac{1}{2}\mathbf{x}^T\,\mathbb{M}\,\mathbf{x}\Big\}$ has to be evaluated. Since $\mathbb{M}$ is symmetric, we can find the (orthogonal) eigenvector matrix $\mathbb{B}$ of $\mathbb{M}$ which has the property $\mathbb{B}^T\,\mathbb{M}\,\mathbb{B} = \mathrm{diag}[\lambda_1,\,\lambda_2,\,\lambda_3]$. With the new vector $\mathbf{y} = \mathbb{B}^{-1}\,\mathbf{x}$ and the fact that $d^3x = |\mathbb{B}|\,d^3y$ we can perform the integration and finally obtain for the distribution function

$$P(\mathbf{u},t) = \mathrm{e}^{Tr(\mathbb{A})\,(t-t_0)}\,\frac{\sqrt{|\mathbb{M}^{-1}|}}{(2\pi)^{3/2}}\,\exp\!\Big\{-\frac{1}{2}\mathbf{V}^T\mathbb{M}^{-1}\mathbf{V}\Big\}\,, \tag{D-12}$$

where $\mathbb{M}^{-1}$ is the inverse of (D-9). Switching back to the original variables $\mathbf{c}$ according to (D-3), we immediately get

$$P(\mathbf{c},t) = \frac{\sqrt{|\mathbb{H}|}}{(2\pi)^{3/2}}\,\exp\!\Big\{-\frac{1}{2}\Big(\mathbf{c} - \mathrm{e}^{-\mathbb{A}\,(t-t_0)}\,\mathbf{c}_0\Big)^T\,\mathbb{H}\,\Big(\mathbf{c} - \mathrm{e}^{-\mathbb{A}\,(t-t_0)}\,\mathbf{c}_0\Big)\Big\}\,, \tag{D-13}$$

where $\mathbb{H} = \mathrm{e}^{\mathbb{A}^T\,(t-t_0)}\,\mathbb{M}^{-1}\,\mathrm{e}^{\mathbb{A}\,(t-t_0)}$ and the identity $|\mathrm{e}^{\mathbb{A}\tau}| = \mathrm{e}^{Tr(\mathbb{A})\tau}$ is taken into account. Furthermore, we note that the transition probability is normalized:

$$\int\limits_{-\infty}^{\infty} d^3c\, P(\mathbf{c},t) = 1\,. \tag{D-14}$$

Using the identities

$$\nabla_\xi \mathrm{e}^{-\frac{1}{2}\xi^T\,\mathbb{H}\,\xi} = -\mathbb{H}\,\xi\,\mathrm{e}^{-\frac{1}{2}\xi^T\,\mathbb{H}\,\xi}$$

and

$$\nabla_\xi\,\nabla_\xi^T \mathrm{e}^{-\frac{1}{2}\xi^T\,\mathbb{H}\,\xi} = \Big(\mathbb{H}\,\xi\,\xi^T\,\mathbb{H} - \mathbb{H}\,\xi\Big)\,\mathrm{e}^{-\frac{1}{2}\xi^T\,\mathbb{H}\,\xi}$$

with $\xi = \mathbf{c} - \hat{\mathbf{c}}_0$, we conclude and that the first moment and the variance are given by

$$< \mathbf{c} >= \int\limits_{-\infty}^{\infty} d^3c\,\mathbf{c}\,P(\mathbf{c},t) = \hat{\mathbf{c}}_0 = \mathrm{e}^{-\mathbb{A}(t-t_0)}\,\mathbf{c}_0 \tag{D-15}$$

and

$$< (\mathbf{c} - \hat{\mathbf{c}}_0)(\mathbf{c} - \hat{\mathbf{c}}_0)^T >=< (\mathbf{c}\,\mathbf{c}^T > - \hat{\mathbf{c}}_0\,\hat{\mathbf{c}}_0^T = \mathbb{H}^{-1} \tag{D-16}$$

respectively, where we assumed that the integrals of $\mathrm{e}^{-\frac{1}{2}\xi^T\,\mathbb{H}\,\xi}$ and $\nabla^T\,\mathrm{e}^{-\frac{1}{2}\xi^T\,\mathbb{H}\,\xi}$ over a surface vanish at infinity.

Appendix E. Some Properties of the Rosenbluth Potentials

The main interesting properties of the Rosenbluth potentials can be traced back to the following identities for $\mathbf{g} = \mathbf{v} - \mathbf{w}$ and $g = |\mathbf{v} - \mathbf{w}|$:

$$\nabla_v g = \frac{\mathbf{g}}{g} \tag{E-1}$$

$$\nabla_v \left(\frac{1}{g}\right) = -\frac{\mathbf{g}}{g^3} \tag{E-2}$$

$$\nabla_v \cdot \mathbf{g} = 3 \tag{E-3}$$

$$\nabla_v \cdot \Big[\nabla_v g\Big] = \nabla_v^2\, g = \frac{2}{g} \tag{E-4}$$

$$\nabla_v \cdot \left[\nabla_v \Big(\frac{1}{g}\Big)\right] = \nabla_v^2 \left(\frac{1}{g}\right) = \begin{cases} 0\,, & \mathbf{v} \neq \mathbf{w} \\ -4\pi\delta\Big(\mathbf{v} - \mathbf{w}\Big)\,, & \mathbf{v} = \mathbf{w} \end{cases}, \tag{E-5}$$

where $\delta\Big(\mathbf{v} - \mathbf{w}\Big)$ is the Dirac distribution. Applying the latter relations to the potentials $\mathcal{H}^{(\beta)}$ and $\mathcal{G}^{(\beta)}$, we immediately obtain

$$\nabla_v^2\, \mathcal{H}^{(\beta)}(\mathbf{x}, \mathbf{v}, t) = -4\pi\, \frac{m_\alpha}{\mu_{\alpha\beta}}\, f_\beta(\mathbf{x}, \mathbf{v}, t) \tag{E-6}$$

and

$$\nabla_v^2\, \mathcal{G}^{(\beta)}(\mathbf{x}, \mathbf{v}, t) = 2\frac{\mu_{\alpha\beta}}{m_\alpha}\, \mathcal{H}^{(\beta)}(\mathbf{x}, \mathbf{v}, t)\,, \tag{E-7}$$

which means, that the potentials $\mathcal{H}^{(\beta)}$ and $\mathcal{G}^{(\beta)}$ are determined by the solution of Poisson equations with sources proportional to f_β and $\mathcal{H}^{(\beta)}$, respectively.

Appendix F. Fourier Transformation of the Coulomb Potential

In order to obtain the Fourier transformation of the Coulomb potential $1/g$ $\Big(g = |\mathbf{v}-\mathbf{w}|\Big)$, it is convenient to start from the Yukawa (or Debye) potential

$$\varphi_\eta(\mathbf{g}) = \frac{\mathrm{e}^{-\eta\, g}}{g}\,, \tag{F-1}$$

where η is a positive real number. Clearly, in the limit $\eta \to 0$ one recovers the usual Coulomb potential. The Fourier transformation of the latter equation

$$\hat{\varphi}_\eta(\mathbf{k}) = \mathcal{F}\left\{\frac{\mathrm{e}^{-\eta\, g}}{g}\right\} = \frac{1}{(2\pi)^{3/2}} \int\limits_{-\infty}^{\infty} d^3g\, \mathrm{e}^{-i\mathbf{k}\cdot\mathbf{g}}\, \frac{\mathrm{e}^{-\eta\, g}}{g} \tag{F-2}$$

can be determined analytically. For that, one introduces spherical coordinates in $\mathbf{g}$-space, perform the integration over the azimuthal and polar angle and get

$$\hat{\varphi}_\eta(\mathbf{k}) = \frac{1}{i\sqrt{2\pi}k} \int\limits_{0}^{\infty} dg\, \mathrm{e}^{-\eta\, g} \left(\mathrm{e}^{ikg} - \mathrm{e}^{-ikg}\right). \tag{F-3}$$

The final integration yields the Fourier transformation of the Yukawa potential given by

$$\hat{\varphi}_\eta(\mathbf{k}) = \frac{2}{\sqrt{2\pi}}\, \frac{1}{k^2+\eta^2}\,, \tag{F-4}$$

from which one obtains immediately the Fourier transformation of the Coulomb potential in the limit $\eta \to 0$:

$$\hat{\varphi}(\mathbf{k}) = \frac{2}{\sqrt{2\pi}\, k^2}\,. \tag{F-5}$$

Appendix G. Hierarchical Sets

A row vector of the form

$$\alpha = (j_1, j_2, \dots, j_\lambda) \tag{G-1}$$

is called a multi-index, where $j_\nu \in \{0, 1, \dots, \mu\}$ for $\nu \in \{1, 2, \dots, \lambda\}$ and $\lambda = 1, 2, \dots$. The length of a multi-index is abbreviated by $l(\alpha) \in \{1, 2, \dots\}$. The special multi-index of length zero is denoted by v: $l(v) = 0$. Furthermore, $n(\alpha)$ imforms about the number of components of α which are equal to zero. For instance, $\alpha = (0, 0)$: $l(\alpha) = n(\alpha) = 2$ and $\alpha = (1, 0, 0, 1, 1)$: $l(\alpha) = 5$, $n(\alpha) = 2$. The set of all multi-indices is denoted by $\mathcal{M}$ and defined according to

$$\begin{aligned} \mathcal{M} = \quad & \Big\{ \quad (j_1, j_2, \dots, j_\lambda) \,|\, j_\nu \in \{0, 1, \dots, \mu\}, \\ & \nu \quad \in \{1, 2, \dots, \lambda\} \text{ for } \lambda = 1, 2, \dots \Big\} \cup \Big\{ v \Big\} , \end{aligned} \tag{G-2}$$

where μ is related to the number of components of the considered Wiener process.

Definition:

A subset $\mathcal{A} \subset \mathcal{M}$ is called a hierarchical set if

- $\mathcal{A}$ is not empty: $\mathcal{A} \neq \emptyset$,
- all $\alpha \in \mathcal{A}$ are uniformly bounded in lenght: $\inf\limits_{\alpha \in \mathcal{A}} < \infty$, and
- $-\alpha \in \mathcal{A}$ for each $\alpha \in \mathcal{A} \setminus \{v\}$.

Furthermore, the remainder set $\mathcal{B}(\mathcal{A})$ of $\mathcal{A}$ is specified by

- $\mathcal{B}(\mathcal{A}) = \Big\{ \alpha \in \mathcal{M} | - \alpha \in \mathcal{A} \Big\}$.

Here, "$-\alpha$" is obtained from "α" by deleting the first component of the row vector: $-\alpha = -(j_1, j_2, \dots, j_\lambda) = (j_2, \dots, j_\lambda)$.

According to this definition one can see that

$$\mathcal{A}_\gamma = \left\{ \alpha \in \mathcal{M} \,|\, l(\alpha) + n(\alpha) \leq 2\,\gamma \;\text{ or }\; l(\alpha) = n(\alpha) = \gamma + \frac{1}{2} \right\} \tag{G-3}$$

is a hierarchical set for $\gamma = 0.5, 1.0, 1.5, \dots$.

- $\mathcal{A}_0 = \Big\{ v \Big\}$, $\mathcal{A}_{0.5} = \mathcal{A}_0 \cup \Big\{ (0);\, (1) \Big\}$, $\mathcal{A}_{1.0} = \mathcal{A}_{0.5} \cup \Big\{ (1,1) \Big\}$.

Another example of a hierarchical set is established by

$$\Gamma_\beta = \Big\{ \alpha \in \mathcal{M} \,|\, l(\alpha) \leq \beta \Big\} \tag{G-4}$$

with the remainder set

$$\mathcal{B}\Big(\Gamma_\beta\Big) = \Big\{ \alpha \in \mathcal{M} \,|\, l(\alpha) = \beta + 1 \Big\} \tag{G-5}$$

for $\beta = 1.0, 2.0, 3.0, \dots$.

- $\Gamma_{1.0} = \Big\{ v;\, (0);\, (1) \Big\}$, $\Gamma_{2.0} = \Gamma_1 \cup \Big\{ (1,1);\, (1,0);\, (0,1);\, (0,0) \Big\}$.

In the following we state explicitly the ITE in the case $d = m = 1$ (one-dimensional in space and one Wiener process) for the hierarchical set $\Gamma_{2.0}$. For this we start from the one-dimensional Itô SDE (69) in integral form

$$C(t) = C(t_0) + \int_{t_0}^{t} ds\, F\{s\} + \int_{t_0}^{t} dW(s)\, B\{s\} \;, \tag{G-6}$$

and apply the Itô formula (80) with $\mathcal{L}^{(0)} = F\frac{d}{dC} + \frac{1}{2}B^2\frac{d^2}{dC^2}$ and $\mathcal{L}^{(1)} = B\frac{d}{dC}$. Then, we obtain immediately the ITE for $\Gamma_{2.0}$ which reads as

$$\begin{aligned} C(t) &= C(t_0) + \sum_{\alpha\in\Gamma_{2.0}} k_\alpha\{t_0\}\, I_\alpha \\ &= C(t_0) + k_{(0)}\, I_{(0)} + k_{(1)}\, I_{(1)} \\ &+ k_{(1,1)}\, I_{(1,1)} + k_{(1,0)}\, I_{(1,0)} + k_{(0,1)}\, I_{(0,1)} + k_{(0,0)}\, I_{(0,0)} \;, \end{aligned} \tag{G-7}$$

where the Itô coefficient functions are given by

$$\begin{aligned} k_{(0)} = F\{t_0\} \quad &, \quad k_{(1)} = B\{t_0\} \\ k_{(1,1)} = \left[B\,\frac{dB}{dC}\right]\{t_0\} \quad &, \quad k_{(1,0)} = \left[B\,\frac{dF}{dC}\right]\{t_0\} \\ k_{(0,1)} = \left[F\,\frac{dB}{dC} + \frac{1}{2}B^2\frac{d^2B}{dC^2}\right]\{t_0\} \quad &, \quad k_{(0,0)} = \left[F\,\frac{dF}{dC} + \frac{1}{2}B^2\frac{d^2F}{dC^2}\right]\{t_0\} \;. \end{aligned}$$

The remainder for this ITE is found to be

$$R = \sum_{\alpha\in\mathcal{B}(\Gamma_{2.0})} k_\alpha\{t_0\}\, I_\alpha \;, \tag{G-8}$$

with multi-indices α taken from the set

$$\mathcal{B}\big(\Gamma_{2.0}\big) = \Big\{(0,0,0);\,(1,0,0);\,(0,1,0);\,(0,0,1);\,(1,1,0);\,(1,0,1);\,(1,1,1)\Big\} \;.$$

Appendix H. Low-Order strong Itô-Taylor scheme

One-Dimensional Schemes ($d = m = 1$): The simplest strong Taylor approximation of the SDE (69), is the Euler scheme of the form

$$C_{n+1} = C_n + F\Big(C_n, t_n\Big)\,\Delta t_n + B\Big(C_n, t_n\Big)\,\sqrt{\Delta t_n}\,\eta_n\,, \tag{H-1}$$

for the approximation of the stochastic variable $C(t)$, where $C_n = C(t_n)$ and $C_0 = V(t_0)$. It is obvious from the ITE that this scheme contains only Wiener integrals of multiplicity one, which are given by $\mathrm{I}_{(0)} = \Delta t_n$ and $\mathrm{I}_{(1)} = \Delta W_n = \sqrt{\Delta t_n}\,\eta_{n+1}$ (see relation (73)), respectively, where $\eta_{n+1} \sim \mathcal{N}(0,1)$ is a Gaussian distributed random number with mean $\mu = 0$ and variance $\sigma^2 = 1$. Note, that the Euler scheme converges with strong order $\gamma = 1/2$. The order of the Euler scheme can easily be improved by considering the next term of the ITE (94), which is given by $B\,\frac{dB}{dC}\,\mathrm{I}_{(1,1)}$ with $\mathrm{I}_{(1,1)} = \int\limits_{t_0}^{t} dW_{s_2} \int\limits_{t_0}^{s_2} dW_{s_1}$. The Itô integral $\mathrm{I}_{(1,1)}$ of multiplicity two can be computed analytically (see footnote 1) and approximated with (73) according to

$$\mathrm{I}_{(1,1)} = \frac{1}{2}\Big[(W_{t+\Delta t} - W_t)^2 - \Delta t\Big] \approx \frac{1}{2}\Big[(\Delta W_n)^2 - \Delta t_n\Big]\,. \tag{H-2}$$

Finally, the Taylor scheme of strong order $\gamma = 1$ reads as

$$\begin{aligned} C_{n+1} &= C_n + F\Big(C_n, t_n\Big)\,\Delta t_n + B\Big(C_n, t_n\Big)\,\Delta W_n \\ &+ \frac{1}{2} B\,B'\,\Big[(\Delta W_n)^2 - \Delta t_n\Big]\,, \end{aligned} \tag{H-3}$$

which was first proposed by Milstein, where $\Delta W_n = \sqrt{\Delta t_n}\,\eta_{n+1}$ and $B' = dB/dC$. Clearly, the latter equation reveals a certain disadvantage of the strong Taylor approximation, namely, the derivative of the diffusion coefficient $B = \sqrt{D}$ must be evaluated. Note, that in the general case, the derivatives of various orders of the diffusion and drift coefficients have to be considered. Strong schemes which avoid the computation of derivatives at each time step are known as explicit strong approximations. To obtain the explicit Milstein scheme we consider

$$B\Big(C_n + \Delta C_n\Big) - B\Big(C_n\Big) = \Big[F\Big(C_n\Big)\,\Delta t_n + B\Big(C_n\Big)\,\sqrt{\Delta t_n}\Big]B' \approx \sqrt{\Delta t_n}\,B\,B'\,,$$

and get in the lowest order of this approximation the explicit strong order $\gamma = 1$ scheme due to Platen

$$\begin{aligned} C_{n+1} &= C_n + F\Big(C_n, t_n\Big)\,\Delta t_n + B\Big(C_n, t_n\Big)\,\Delta W_n \\ &+ \frac{1}{2\sqrt{\Delta t_n}}\Big[B\Big(\tilde{C}^{\,n}, t_n\Big) - B\Big(C_n, t_n\Big)\Big]\,\Big[(\Delta W_n)^2 - \Delta t_n\Big]\,, \end{aligned} \tag{H-4}$$

with the supporting value

$$\tilde{C}^{\,n} = C_n + F\Big(C_n, t_n\Big)\,\Delta t_n + B\Big(C_n, t_n\Big)\,\sqrt{\Delta t_n}\,, \tag{H-5}$$

where $\Delta W_n = \sqrt{\Delta t_n}\,\eta_{n+1}$ with $\eta_{n+1} \sim \mathcal{N}(0,1)$.

Multi-Dimensional Schemes: In the following we present strong Taylor approximations for the multi-dimensional SDE (82). In order to find the lowest strong order schemes in vector form, we first introduce the auxiliary vector $\mathbf{b}_p^{\,n} = \mathbb{B}\Big(\mathbf{C}^{\,n}, t_n\Big)\,\mathbf{e}_p \in \mathbb{R}^d$ at the time level t_n, which

represents the p$^{\text{th}}$ column of the matrix $\mathbb{B}$, and $\mathbf{e}_p \in \mathbb{R}^m$ is a unit vector with the entry "1" in the p$^{\text{th}}$ row. Then, for the approximation $\mathbf{C}(t)$ of the stochastic variable $\mathbf{V}(t)$, we obtain from the ITE (94)

$$\begin{aligned}\mathbf{C}^{n+1} &= \mathbf{C}^n + \mathbf{F}\Big(\mathbf{C}^n, t_n\Big)\,\mathrm{I}_{(0)} + \sum_{q=1}^{m} \mathbf{b}_q^n\,\mathrm{I}_{(q)} \\ &+ \sum_{p,q=1}^{m} \mathbf{b}_p^n \cdot \nabla_c\, \mathbf{b}_q^n\,\mathrm{I}_{(p,q)} + \mathcal{O}(\Delta t^{3/2})\,, \end{aligned} \tag{H-6}$$

where we used the result that $\mathcal{L}^{(p)}$ can be expressed by $\mathcal{L}^{(p)} = \mathbf{b}_p^n \cdot \nabla_c$ with the nabla operator $\nabla_c = \left(\frac{\partial}{\partial C_1}, \frac{\partial}{\partial C_2}, \frac{\partial}{\partial C_3}\right)^T$. Considering only the first three terms of the rhs (H-6), we obtain the forward Euler scheme of strong order $\gamma = 1/2$. Including the remaining term, expression (H-6) establish the stong $\gamma = 1$ order Milstein scheme, where the analytical form of the diffusion coefficients are needed to perform the derivatives. The explict – which means derivation free – strong Milstein scheme in the multi-dimensional case is obtained by replacing the derivation according to

$$\mathbf{b}_p^n \cdot \nabla_c\, b_{q,i}^n = \frac{1}{\sqrt{\Delta t_n}}\Big[b_{q,i}^n\big(\mathbf{S}_p^n\big) - b_{q,i}^n\big(\mathbf{C}^n\big)\Big] \tag{H-7}$$

with the supporting vector

$$\mathbf{S}_p^n = \mathbf{C}^n + \Delta\mathbf{C}^n\,; \quad \Delta\mathbf{C}^n = \mathbf{F}\Big(\mathbf{C}^n, t_n\Big)\,\Delta t_n + \mathbf{b}_p^n\,\sqrt{\Delta t_n}\,, \tag{H-8}$$

where $b_{q,i}^n$ is the i$^{\text{th}}$ component of $\mathbf{b}_q^n$. Similar to the one-dimensional case, the Itô integrals of multiplicity one are approximated according to $\mathrm{I}_{(q)} = \Delta W_n^q = \sqrt{\Delta t_n}\,\eta_{n+1}^q$ with $\eta_{n+1}^q \sim \mathcal{N}(0,1)$. However, an additional difficulty arise in computing the Itô integrals of multiplicity two. In order to evaluate these integral, we adopt from the literature the result [49]

$$\mathrm{I}_{(p,q)} = \begin{cases} \frac{1}{2}\left[\Big(\Delta W_n^p\Big)^2 - \Delta t_n\right] & \text{for } p = q \\ \mathrm{J}_{(p,q)} & \text{for } p \neq q \end{cases}, \tag{H-9}$$

which allows to compute the Itô integral $\mathrm{I}_{(p,q)}$ from its Stratonovich counterpart $\mathrm{J}_{(p,q)}$. It is possible to represent multiple stochastic Stratonovich integrals in effectiv approximate way. The method for multiple Stratonovich integrals based on the Fourier (Kahunen-Loéwe) series expansion; for details we refer the reader to the books [50] or [49]. In essence, the series expansion is truncated at P_S and the multiple Stratonovich integrals $\mathrm{J}_{(j_1,j_2,\ldots,j_l);\,\Delta t}$ are approximated by Riemann-Stieltjes integrals $\mathrm{J}^{(P_S)}_{(j_1,j_2,\ldots,j_l);\,\Delta t}$, which converge to the Stratonovich integral. After a simple, but lengthy computation we obtain the result

$$\begin{aligned}\mathrm{J}^{(P_S)}_{(p,q)} &= \frac{\Delta t}{2}\,\xi_p\,\xi_q + \Delta t\,\sqrt{\rho_{P_S}}\left(\mu_p^{(P_S)}\,\xi_q - \mu_q^{(P_S)}\,\xi_p\right) \\ &+ \frac{\Delta t}{2\pi}\sum_{r=1}^{P_S}\frac{1}{r}\left[\zeta_{p,r}\Big(\sqrt{2}\,\xi_q + \eta_{q,r}\Big) - \zeta_{q,r}\Big(\sqrt{2}\,\xi_p + \eta_{p,r}\Big)\right] \end{aligned} \tag{H-10}$$

with

$$\rho_{P_S} = \frac{1}{12} - \frac{1}{2\pi^2}\sum_{r=1}^{P_S}\frac{1}{r^2}\,, \tag{H-11}$$

where ξ_j, $\zeta_{j,k}$, $\eta_{j,k}$ and $\mu_j^{(P_S)}$ are independent standard Gaussian random variables (which means, zero mean and variance one: $\mathcal{N}(0,1)$). It is obvious from the latter expression that the strong Milstein scheme is numerical much more expensive than the strong forward Euler, because a lot of additional random variables have to be generated. Furthermore, if we interpret Itô integrals as random numbers, it is clear from equation (H-10) that, especially high multiplicity integrals possess a very complex "inner structure" which may be resolved by standard Gaussian random numbers.

Numerical Experiment: In order to investigate the approximation behaviour of the strong forward Euler and Milstein scheme (H-6) experimentally, we consider the one-dimensional Itô process $V = \Big\{ V(t)\,; 0 = t_0 \le t \le T = 1 \Big\}$ satisfying

$$dV(t) = -\frac{1}{2}\, V(t)\, dt + V(t)\, dW^1(t) + V(t)\, dW^2(t) \tag{H-12}$$

on the time interval $0 \le t \le 1$ for the initial value $V_0 = V(0) = 1$, where $W^1(t)$ and $W^2(t)$ are two independent Wiener processes. Using the multi-dimensional Itô formula (83) for $\Phi = \ln V(t)$, we can immediately check that the SDE (H-12) has the analytical solution

$$V(t) = V_0 \exp\Big\{ -\frac{3}{2}\, t + W^1(t) + W^2(t) \Big\}\,, \tag{H-13}$$

where $\Delta W^j(t)$ is determined from relation (72). For the comparison of the strong approxima-

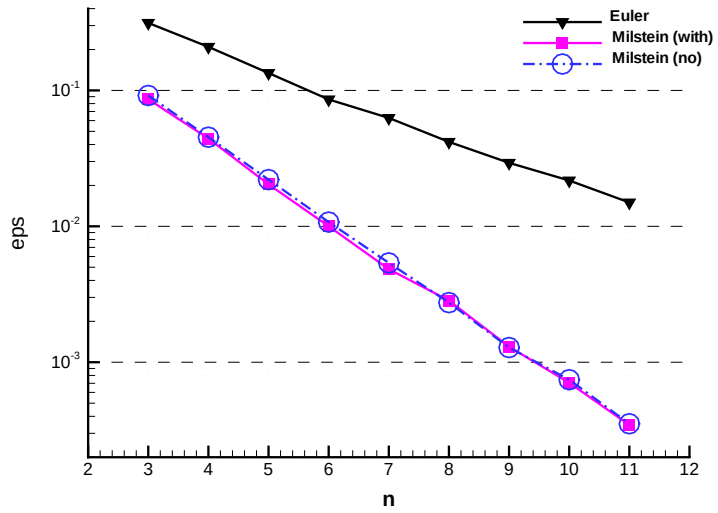

FIGURE 8.1. Comparison of the mean batch average $\hat{\epsilon}$ (= eps) as a function of the exponent n (corresponding to the discretization $\Delta t = 2^{-n}$) for the Euler scheme (full line with gradients), the Milstein scheme with derivations (full line with squares; $P_S = \min(2^n, 512)$) and the derivation-free Milstein scheme (dashed-dotted line with open circles; $P_S = 16$).

tion of the SDE (H-12) according to (H-6) with the analytical solution (H-13), we organized

the simulation into $M = 40$ batches of $N = 100$ trajectories each and compute the mean $\hat{\epsilon}$ of the batch average $\hat{\epsilon}_k$ from

$$\hat{\epsilon} = \frac{1}{M}\sum_{k=1}^{M}\hat{\epsilon}_k = \frac{1}{M}\sum_{k=1}^{M}\left(\frac{1}{N}\sum_{j=1}^{N}|V_{j,k}(T) - C_{j,k}(T)|\right) \tag{H-14}$$

for different discretizations $\Delta t = 2^{-n}$ of the considered time interval, where $C_{j,k}(T)$ represents the solution of the strong Euler or Milstein approximation. The results depicted in Figure 8.1, where the mean of the batch averages $\hat{\epsilon}$ is plotted as a function of the discretization exponent n for the Euler (full line with gradients), the Milstein (full line with squares; $P_S = \min(2^n, 512)$) and the derivation-free Milstein (dashed-dotted line with open circles; $P_S = 16$) scheme. Clearly, this plot demonstrate that the agreement between the Milstein scheme with and without derivations is very good and suggests to use the less expensive derivation-free scheme. Furthermore, we derive from the slope of the curves that the experimental order of convergence is ~ 0.54 and ~ 1.01 for the Euler and the Milstein scheme, respectively, which agree very well with the nominal strong order of $\gamma = 1/2$ and $\gamma = 1$. Finally note, that $\hat{\epsilon}$ may be considered as a measure of the pathwise closeness at the end of the time interval $[0, 1]$, which represent the absolute error criterion. Moreover, the quality of the estimate (H-14) can be assessed with the variance

$$\hat{\sigma}_\epsilon^2 = \frac{1}{M-1}\sum_{k=1}^{M}\left(\hat{\epsilon}_k - \hat{\epsilon}\right)^2$$

of the batch averages, which is necessary to evaluate a confidence interval for $\hat{\epsilon}$ based on the Student t-distribution [50].

Appendix I. Weakly Consistent Schemes

If there exists a nonnegative function $\varphi = \varphi(\delta)$ with $\lim\limits_{\delta \downarrow 0} \varphi(\delta) = 0$ such that

$$\mathcal{E}\left\{ \left| \mathcal{E}\left\{ \frac{1}{\Delta t_n} \Big(\mathbf{V}^{\delta}_{n+1} - \mathbf{V}^{\delta}_{n} \Big) \right\} - \mathbf{F}\big(\mathbf{V}^{\delta}_{n}, t_n\big) \right|^2 \right\} \leq \varphi(\delta) \tag{I-1}$$

and

$$\mathcal{E}\left\{ \left| \mathcal{E}\left\{ \frac{1}{\Delta t_n} \Big(\mathbf{V}^{\delta}_{n+1} - \mathbf{V}^{\delta}_{n} \Big) \Big(\mathbf{V}^{\delta}_{n+1} - \mathbf{V}^{\delta}_{n} \Big)^T \right\} - \mathbb{B}\big(\mathbf{V}^{\delta}_{n}, t_n\big)\, \mathbb{B}^T\big(\mathbf{V}^{\delta}_{n}, t_n\big) \right|^2 \right\} \leq \varphi(\delta) \tag{I-2}$$

for $n = 1, 2, \dots$, then a discrete approximation $\mathbf{V}^{\delta}_{n}$ with maximum time step size $\delta = \max\limits_{\forall n}\{\Delta t_n\} = \Delta t$ is weakly consistent, where $\mathbb{D} = \mathbb{B}\,\mathbb{B}^T$.

Weak Euler Scheme (116)

For the Euler scheme in the form

$$\mathbf{V}_{n+1} = \mathbf{V}_n + \mathbf{F}\big\{t_n\big\}\,\Delta t + \sum_p \mathbf{b}_q\big\{t_n\big\}\,\mathcal{I}_{(p)} \tag{I-3}$$

we obtain

$$\mathcal{E}\Big\{ \mathbf{V}_{n+1} - \mathbf{V}_n \Big\} = \mathbf{F}\big\{t_n\big\}\,\Delta t\,, \tag{I-4}$$

from which we conclude that (I-1) vanishes. Since $\mathcal{E}\Big\{ \mathcal{I}_{(p)}\,\mathcal{I}_{(q)} \Big\} = \Delta t\,\delta_{pq}$ we get from

$$\begin{aligned} \mathcal{E}\Big\{ \Big(\mathbf{V}_{n+1} - \mathbf{V}_n \Big) \Big(\mathbf{V}_{n+1} - \mathbf{V}_n \Big)^T \Big\} &= \mathbf{F}\big\{t_n\big\}\,\mathbf{F}^T\big\{t_n\big\}\,(\Delta t)^2 \\ &+ \sum_{p,q} \mathbf{b}_p\big\{t_n\big\}\,\mathbf{b}^T_q\big\{t_n\big\}\,\mathcal{E}\Big\{ \mathcal{I}_{(p)}\,\mathcal{I}_{(q)} \Big\} \\ &= \mathbf{F}\big\{t_n\big\}\,\mathbf{F}^T\big\{t_n\big\}\,(\Delta t)^2 \\ &+ \mathbb{D}\big\{t_n\big\}\,\Delta t\,. \end{aligned} \tag{I-5}$$

that condition (I-2) is of the order $\mathcal{O}\Big((\Delta t)^2\Big)$. Consequently, the Euler scheme (I-3) is weakly consistent.

Weak $\beta = 2.0$ Itô-Taylor Scheme (125)

In the following we consider this scheme in the form

$$\begin{aligned} \mathbf{V}_{n+1} &= \mathbf{V}_n + \mathbf{F}\big\{t_n\big\}\,\Delta t + \frac{1}{2}\Big[\mathcal{L}^{(0)}\,\mathbf{F}\Big]\big\{t_n\big\}\,(\Delta t)^2 \\ &+ \sum_p \mathbf{b}_p\big\{t_n\big\}\,\mathcal{I}_{(p)} + \sum_{p,q} \Big[\mathbf{b}_p \cdot \nabla_c\,\mathbf{b}_q\Big]\big\{t_n\big\}\,\mathcal{I}_{(p,q)} \\ &+ \sum_p \Big[\mathbf{b}_p \cdot \nabla_c\,\mathbf{F}\Big]\big\{t_n\big\}\,\mathcal{I}_{(p,0)} + \sum_p \Big[\mathcal{L}^{(0)}\,\mathbf{b}_p\Big]\big\{t_n\big\}\,\mathcal{I}_{(0,p)}\,. \end{aligned} \tag{I-6}$$

It is obvious that the expectation of (I-6) immediately yields

$$\mathcal{E}\Big\{\mathbf{V}_{n+1}-\mathbf{V}_n\Big\}=\mathbf{F}\big\{t_n\big\}\,\Delta t+\frac{1}{2}\Big[\mathcal{L}^{(0)}\,\mathbf{F}\Big]\big\{t_n\big\}\,(\Delta t)^2 \tag{I-7}$$

and, hence, the left-hand side of relation (I-1) is proportional to $(\Delta t)^2$. Keeping only the two lowest orders in Δt, we find for scheme (I-6) that

$$\mathcal{E}\Big\{\Big(\mathbf{V}_{n+1}-\mathbf{V}_n\Big)\Big(\mathbf{V}_{n+1}-\mathbf{V}_n\Big)^T\Big\}\approx\mathbb{D}\big\{t_n\big\}\,\Delta t+\mathbb{H}\big\{t_n\big\}\,(\Delta t)^2\,, \tag{I-8}$$

where $\mathbb{H}$ is given by

$$\begin{aligned}\mathbb{H}\big\{t_n\big\}=\Bigg(\mathbf{F}\,\mathbf{F}^T\quad&+\quad\frac{1}{2}\Bigg(\mathbf{b}_p\Big[\mathbf{b}_p\cdot\nabla_c\,\mathbf{F}\Big]^T+\mathbf{b}_p\Big[\mathcal{L}^{(0)}\,\mathbf{b}_p\Big]^T\\&+\quad\Big[\mathbf{b}_p\cdot\nabla_c\,\mathbf{F}\Big]\mathbf{b}_p^T+\Big[\mathcal{L}^{(0)}\,\mathbf{b}_p\Big]\mathbf{b}_p^T\Bigg)\Bigg)\big\{t_n\big\}\,.\end{aligned} \tag{I-9}$$

From this observation we obtain that the expectation value (I-2) is also propotional to $(\Delta t)^2$ and the Itô-Taylor Scheme (I-6) is weakly consistent.